

12-2011

First-principles Studies on Physical and Chemical Properties of Nanostructures

Menghao Wu

University of Nebraska-Lincoln, wmh198789@163.com

Follow this and additional works at: <http://digitalcommons.unl.edu/physicsdiss>

 Part of the [Condensed Matter Physics Commons](#), and the [Physical Chemistry Commons](#)

Wu, Menghao, "First-principles Studies on Physical and Chemical Properties of Nanostructures" (2011). *Theses, Dissertations, and Student Research: Department of Physics and Astronomy*. 16.
<http://digitalcommons.unl.edu/physicsdiss/16>

This Article is brought to you for free and open access by the Physics and Astronomy, Department of at DigitalCommons@University of Nebraska - Lincoln. It has been accepted for inclusion in Theses, Dissertations, and Student Research: Department of Physics and Astronomy by an authorized administrator of DigitalCommons@University of Nebraska - Lincoln.

First-principles Studies on Physical and Chemical Properties of Nanostructures

by

Menghao Wu

A Dissertation

Presented to the Faculty of

The Graduate College at the University of Nebraska

In Partial Fulfillment of Requirements

For the Degree of Doctor of Philosophy

Major: Physics & Astronomy

Under the Supervision of Professor Xiao Cheng Zeng

Lincoln, Nebraska

December, 2011

First-principles Studies on Physical and Chemical Properties of Nanostructures

Menghao Wu, Ph.D.

University of Nebraska, 2011

Adviser: Xiao Cheng Zeng

The physical and chemical properties of decorated graphene and graphene ribbons, single-layer III-V systems, three-dimensional carbon and BN foam, and transition-metal-molecular sandwich nanowires have been investigated by first-principle calculations and their potential applications have been predicted. First, it is shown that zigzag graphene nanoribbons (ZGNRs) can be converted into half metal when their edges are decorated by some chemical functional groups, and the half-metallicity is induced by chemical potential difference between two edges when one edge is decorated by electron-donating group like $-OH$ and the other edge is decorated by electron-accepting group like $-F$, $-NH_2$, $-N(CH_3)_2$, $-SO_2$, $-NO_2$ and $-CN$, or by spin-polarized impurity state induced by isolated SO_2 group. In addition, no matter how trivial the potential difference between two edges is, the decorated ZGNR can be half metal as long as the width of ZGNR is sufficiently large. As ZGNRs are decorated by copper atoms, they are shown to be a unique host system for the realization of an extended planar tetracoordinate carbon (ptC) strips due to its highly delocalized in-plane π -electrons and intrinsic rigid structure. When they are decorated by scandium atoms, they are shown to be good candidates for hydrogen storage and the adsorption energy can be controlled by electric field. Second, graphene is also revealed to become half metal through selective chemical decorations, and by selective hydrogenation, it can become magnetic

quantum dot arrays and its magnetic coupling or band gap can be tuned, which can be applied for magnetic data storage and light-emitting devices. Third, single-layer BN and some other hexagonal systems like AlN, GaN, BP, SiC, ZnO are studied. It is demonstrated that upon charge-injection some of them like BN and AlN can become magnetic or even half-metallic, which is clarified by using Stoner Criterion. As they are cut into zigzag nanoribbons with one or two edges unpassivated, some of them may become half metals, and the edge-reconstructions of the unpassivated edges are studied. Fourth, two kinds of 3D carbon and BN foam, one with hexagonal holes and the other with triangular holes and only pure sp^2 carbon bonds, are designed, and they are shown to be stable and porous low-density carbon and BN allotrope with large internal surface area and strong bulk modulus. Finally, some transition-metal-molecular sandwich nanowires can become magnetic or even half-metallic from nonmagnetic through charge-injection, which is also clarified by using Stoner Criterion. For Ti-benzene nanowires its magnetic coupling can be tuned either by charge-injection or tension.

ACKNOWLEDGEMENTS

My sincerely thanks to all the people who have contributed to this work.

I would first like to thank my advisor, Professor Xiao Cheng Zeng, for his effective instructions and excellent guidance. I sincerely appreciated his support and suggestions on my research. It has been a great honor for me to study with Prof.Zeng and it is very beneficial to my science career.

I would also like to thank current and former Zeng's group members, a group of people who adventure the unknown world of science with talent and enthusiasm and are willing to help each other. My special thanks got to Dr. Xiaojun Wu, Yong Pei, Yi Gao, Jaeil Bai, Hui Li, Jun Wang, Nan Shao, Chad Killblane, Zhuhua Zhang, Guiling Zhang, Rulong Zhou and other graduate students Rhitankar, Yu, Peng and Lei.

I would also like to thank my Supervisory Committee: Professor Hui Li, Sy-Hwang Liou, and Sitaram Jaswal, and Professor Tsymbal, Belashchenko, Dr. Burton and Wang in Department of Physics, for their advice, discussions, support and encouragement through my graduate years.

Finally, I would like to thank my parents, for their everlasting unconditional support during my study abroad.

CONTENTS

1	Introduction to theoretical methods	
1.1	Wavefunctions & Schroedinger's equation	1
1.2	Hohenberg-Kohn theorem and Kohn-Sham equation	2
1.3	Approximations for the exchange-correlation functional	4
1.4	Basis set function	6
1.5	Nanostructures of different dimensions	8
1.6	References	8
2	Edge-decorated graphene nanoribbons	
2.1	Introduction	10
2.2	Computational details	11
2.3	Half-metallicity in edge-decorated ZGNRs	12
2.4	Metal-decorated ZGNRs as mediums for planar tetracoordinate carbon strips	28
2.5	Hydrogen storage in metal-decorated GNRs	37
2.6	References	51
3	Decorated graphene of various physical applications	
3.1	Introduction	58
3.2	Computational details	59
3.3	Half-metallicity in periodically functionalized graphene	60
3.4	Magnetic quantum dot arrays	63
3.5	References	70

4	Single-layer BN and other hexagonal systems	
4.1	Introduction	72
4.2	Computational details	72
4.3	Charge-Injection Induced magnetism and half metallicity in single-Layer hexagonal group III/V (BN, BP, AlN, AlP) systems	73
4.4	Inorganic nanoribbons with unpassivated zigzag edge: half metallicity and edge reconstructions	79
4.5	References	87
5	Three-dimensional carbon and BN foam	
5.1	Introduction	90
5.2	Computational details	90
5.3	Results and discussions	91
5.4	Conclusions	100
5.5	References	101
6	Transition-Metal-Molecular Sandwich Nanowires as Magnetic On/Off Switch	
6.1	Introduction	102
6.2	Computational details	103
6.3	Results and discussions	103
6.4	Conclusions	114
6.5	References	115

1 Introduction to theoretical methods

1.1 Wavefunctions & Schroedinger's Equation

For a microscopic system, its properties are determined by the interactions between the constituting electrons and nuclei, and from the point of view of quantum mechanics, they are given by many-body Schrodinger equation written as:

$$H \Psi(\mathbf{x}_1, \mathbf{x}_2, \dots, \mathbf{x}_N; \mathbf{R}_1, \dots, \mathbf{R}_{N_n}) = E \Psi(\mathbf{x}_1, \mathbf{x}_2, \dots, \mathbf{x}_N; \mathbf{R}_1, \dots, \mathbf{R}_{N_n}) \quad (1.1)$$

here $\mathbf{x}_1, \mathbf{x}_2, \dots, \mathbf{x}_N$ denote the spin and cartesian coordinates of the N electrons in the system, and $\mathbf{R}_1, \dots, \mathbf{R}_{N_n}$ are the nuclear coordinates of the N_n nuclei in the system. The Hamiltonian operator is given by:

$$H = T_e + T_n + V_{en} + V_{ee} + V_{nn} \quad (1.2)$$

where the kinetic and potential energies of N electrons (e) and N_n nuclei (n) are given by:

$$T_e = -\frac{\hbar^2}{2m_e} \sum_{\mu=1}^{N_e} \nabla_{\mu}^2 \quad (1.3)$$

$$T_n = -\frac{\hbar^2}{2} \sum_{k=1}^{N_n} \frac{\nabla_k^2}{m_k}$$

$$V_{en} = -\sum_{\mu=1}^{N_e} \sum_{k=1}^{N_n} \frac{Z_k e^2}{4\pi\epsilon_0 |\vec{r}_{\mu} - \vec{R}_k|}$$

$$V_{ee} = \sum_{\mu=1}^{N_e} \sum_{\nu>\mu}^{N_e} \frac{e^2}{4\pi\epsilon_0 |\vec{r}_{\mu} - \vec{r}_{\nu}|}$$

$$V_{nn} = \sum_{j=1}^{N_n} \sum_{k>j}^{N_n} \frac{Z_k Z_j e^2}{4\pi\epsilon_0 |\vec{R}_j - \vec{R}_k|}$$

Because the masses of nuclei are very large and the nuclei move much more slowly than electrons, according to the Born-Oppenheimer approximation, the system can be well described by the motion of electrons alone and the kinetic energy of nuclei can be ignored in the Hamiltonian. Since we are interested in the electronic structures, the V_{nn} term is then irrelevant and can be dropped. Therefore the Hamiltonian can now be simplified as:

$$H = -\frac{\hbar^2}{2m_e} \sum_{\mu=1}^{N_e} \nabla_{\mu}^2 - \sum_{\mu=1}^{N_e} \sum_{k=1}^{N_n} \frac{Z_k e^2}{4\pi\epsilon_0 |\vec{r}_{\mu} - \vec{R}_k|} + \sum_{\mu=1}^{N_e} \sum_{\nu>\mu}^{N_e} \frac{e^2}{4\pi\epsilon_0 |\vec{r}_{\mu} - \vec{r}_{\nu}|} \quad (1.4)$$

However, the correlation interaction of electrons cannot simply be given by isolated electron wavefunctions due to the third term giving the interactions among electrons. To study a system of interacting electrons and nuclei, a many-body wavefunctions must be built and can be solved only after certain conditions of approximation are assumed, and a popular method of approximation is density-functional theory (DFT) method, which only deals with the density of electron while includes both the exchange and correlation interaction, which is described in following sections.

1.2 Hohenberg-Kohn theorem and Kohn-Sham equation

In 1964, Hohenberg & Kohn demonstrated that [1]: 1. the ground state properties of a many-body interacting electron system, including the many-body wave function, are uniquely determined by the ground state electron density; 2. The energy of a system $E[\rho]$ reaches the

minimal value at the ground state density. In DFT method, the electronic energy is partitioned into several terms:

$$E[\rho] = T_s[\rho] + V_{en}[\rho] + V_{nn} + J[\rho] + Exc[\rho] \quad (1.5)$$

where the first to fifth term are respectively the kinetic energy term arising from the motion of the electrons, potential energy of the nuclear-electron attraction and the nuclear-nuclear repulsion due to the classical Coulomb interaction, the Coulomb electron-electron repulsion, and the exchange-correlation term. The reference system of fictitious non-interacting particles has a rigorous solution in terms of single electron wavefunctions, or molecular orbitals called the Kohn-Sham (KS) orbitals. Assuming the single particle orbital is χ , and as proposed by Kohn

and Sham [2], the density of the auxiliary system is then $\rho = \sum_{j=1}^N \sum_{\sigma} |\chi_j(\vec{r}, \sigma)|^2$ and the kinetic

energy $T_s[\rho_s] = -\frac{1}{2} \sum_{j=1}^N \langle \chi_j | \nabla_j^2 | \chi_j \rangle$. In practice, a basis set expansion is used to represent

the KS orbitals and the entire energy functional in terms of the KS orbitals is given by:

$$E[\rho] = -\frac{1}{2} \sum_{j=1}^N \langle \chi_j | \nabla_1^2 | \chi_j \rangle + \frac{1}{2} \sum_{j=1}^N \sum_{i=1}^N \iint \langle \chi_j \chi_i | \frac{1}{r_{12}} | \chi_j \chi_i \rangle + Exc[\rho] - \sum_{a=1}^{N_n} \sum_{j=1}^N Z_a \langle \chi_j | \frac{1}{r_{a1}} | \chi_j \rangle + \sum_{a=1}^{N_n} \sum_{b=1}^{N_n} \frac{Z_a Z_b}{r_{ab}} \quad (1.6)$$

As the functional derivative of this expression is set to zero, the KS orbitals must satisfy:

$$\left\{ -\frac{1}{2} \nabla_1^2 - \sum_{a=1}^{N_n} \frac{Z_a}{r_{a1}} + V_{KS}(\vec{r}_1) \right\} \chi_j = \epsilon_j \chi_j \quad (1.7)$$

here the effective KS potential where the non-interacting particles move includes both classical electrostatic interaction and exchange-correlation potential.

$$V_{KS}(\vec{r}_1) = \int \frac{\rho(\vec{r}_2)}{r_{12}} d\vec{r}_2 + V_{xc}(\vec{r}_1) \quad (1.8)$$

Here the V_{xc} term includes unknown functional forms for the coulomb and exchange correlation energy. The major issue in the Kohn-Sham approach is how to obtain the expression of the exchange-correlation potential. Since the unknown density is required to write out the KS potential, the equations are also non-linear pseudo-eigenvalue equations and must be solved by an SCF method.

1.3 Approximations for the Exchange-Correlation Functional

A widely used approximation is called the Local Density Approximation (LDA) assuming that at every point in space we can use the value of the density that the uniform electron gas would have at that point, and allow it to vary from point to point. As a result we can write exchange-correlation energy as:

$$E_{xc}^{LDA}[\rho] = \int \rho(\vec{r}) \varepsilon_{xc}(\rho(\vec{r})) d\vec{r}, \quad \varepsilon_{xc}(\rho(\vec{r})) = \varepsilon_x(\rho(\vec{r})) + \varepsilon_c(\rho(\vec{r})) \quad (1.9)$$

here the $\varepsilon_x(\rho(\vec{r})) = -\frac{3}{4} \left(\frac{3\rho(\vec{r})}{\pi} \right)^{1/3}$ is the Dirac/Slater Exchange energy of electron gas[3]. The Coulomb correlation term is obtained based on analytical interpolations of Quantum Monte Carlo calculations (Ceperly and Alder (1980))[4]. Another typical LDA approximation is the

SWVN implementation that implies Slater Exchange plus Coulomb correlation obtained by Vosko, Wilk & Nussair (1980)[5]. In 1992 a more accurate implementation is made by Perdew and Wang. For spin-polarized systems, the local spin density approximation (LSDA) considers electrons with different spin respectively, therefore can give better results.

The LDA by its self does not contain sufficient accuracy for chemical applications and always underestimate bond lengths. In addition, it is weak in describing strong correlated systems. It is necessary to include terms considering the spatial variation of the density. The formulation of functionals within the Generalized Gradient Approximation (GGA) depending both on electron density and gradient of electron density has improved the exchange and correlation functionals of LDA and LSDA greatly and made good accuracy density functional theory possible [6]. Like LDA, approximations are made separately for the exchange and correlation portions. For exchange functional:

$$E_x^{CGA} = E_x^{LDA} - \sum_{\sigma} F(s_{\sigma}) \rho_{\sigma}^{4/3}(\vec{r}) d\vec{r}, s_{\sigma} = \frac{|\nabla \rho|}{\rho_{\sigma}^{4/3}} \quad (1.10)$$

Two commonly used choices for the Exchange functional are Perdew-Wang's 1991 exchange functional[7] and Becke's 1988 functional[8]. The second functional is normally Perdew-Wang (PW91) correlation functional[7], Becke correlation functional[8] and the Lee-Yang-Parr correlation functional (LYP)[9]. Perdew-Burke-Ernzerhof exchange and correlation functional (PBE)[10] has no empirical parameters, which is applied most often in this thesis. In addition, any exchange functional can be combined with any correlation functional. For example, BLYP is the combination of Becke 1988 exchange functional and LYP correlation functional [11]. Mixing

different exchange and correlation functional with different weight generates the hybrid exchange and correlation functional, such as B3LYP[12].

1.4 Basis set function

Linear combination of atomic orbits approximation (LCAO) leads that any one electron molecular orbital can be written as a linear combination of atomic orbitals (basis functions):

$$\Phi_i = \sum_{\mu=1}^K c_{\mu i} \varphi_{\mu} \quad (1.11)$$

A basis set is such a combination of mathematical functions designed to give the maximum flexibility to the molecular orbitals and their coefficients are obtained variationally . There are two types of popular atom-centered basis functions, Slater type orbital (STO) [13] and Gaussian type orbital (GTO) [14]. STO has the following general form:

$$\varphi_i(\xi, n, l, m; r, \theta, \varphi) = N r^{n-1} e^{-\xi r} Y_{lm}(\theta, \varphi) \quad (1.12)$$

And their normalized forms :

$$\begin{aligned} \varphi_{1s} &= \left(\frac{\xi_1^3}{\pi} \right)^{1/2} \exp(-\xi_1 r) \\ \varphi_{2s} &= \left(\frac{\xi_2^5}{96\pi} \right)^{1/2} r \exp\left(-\frac{\xi_2 r}{2}\right) \\ \varphi_{2p_x} &= \left(\frac{\xi_2^5}{32\pi} \right)^{1/2} x \exp\left(-\frac{\xi_2 r}{2}\right) \end{aligned} \quad (1.13)$$

They are similar to atomic orbitals of the hydrogen atom, but they are not suitable for fast calculations of necessary two-electron integrals. That is why GTOs were introduced. You can approximate the shape of the STO function by summing up a number of GTOs with different exponents and coefficients. Even if you use 4 or 5 GTO's to represent STO, you will still calculate your integrals much faster than if original STOs are used. The GTO (called also cartesian gaussian) is expressed as:

$$g(\alpha, l, m, n; x, y, z) = Ne^{-\alpha r^2} x^l y^m z^n \quad (1.14)$$

or

$$g(\alpha, l, m, n, f; x, y, z) = Ne^{-\alpha f^2 r^2} x^l y^m z^n \quad (1.15)$$

Here N is normalization constant and f is scaling factor, which scale all exponents in the related gaussians in molecular calculations. In spherical coordinates:

$$\varphi_{\text{GTO}}(\xi, n, l, m; r, \theta, \varphi) = Nr^{2n-2l-1} e^{-\alpha r^2} Y_{lm}(\theta, \varphi) \quad (1.16)$$

GTOs are inferior to STOs as the GTO has zero slope at the nucleus while the STO has a cusp. Behavior near the nucleus is poorly represented. GTOs also diminish too rapidly with distance so the 'tail' behavior is poorly represented. In addition, Extra d -, f -, g -, etc. functions (from Cart. rep.) may lead to linear dependence of the basis set. They are usually dropped when large basis sets are used. However, GTOs have analytical solutions and we can use a linear combination of GTOs to overcome these deficiencies.

Another basis set popular in calculations on periodic systems is plane wave non-localized basis set. Infinite number of electrons in a periodic crystal can be simplified to the number of electrons in the unit cell of the crystal using Bloch's theorem, while each electronic wavefunction is written as a sum of infinite plane waves. Applying a plane wave energy cutoff reduces the basis set to a finite size, and the error caused by this kinetic energy cut-off can be reduced by using larger energy cut-off.

1.5 Nanostructures of different dimensions

In this thesis my work includes nanostructures of different dimensions. Graphene is a flat monolayer of carbon atoms tightly packed into a two-dimensional (2D) honeycomb lattice, and is a basic building block for graphitic materials of other dimensionalities. It can be wrapped up into 0D fullerenes, cut into 1D nanoribbons, rolled into 1D nanotubes or stacked into 3D graphite. In this thesis chapter 2 and 3 are about 2D graphene and 1D graphene nanoribbons. In Chapter 4 2D single-layer BN and other III-IV compound have similar hexagonal lattice to graphene, and they can also be cut into 1D nanoribbons. In Chapter 5 I used 1D graphene and BN nanoribbons to build two types of 3D carbon and BN foams. In chapter 6 1D transition-metal-molecular sandwich nanowires are studied. Most of those systems contain only light elements and only metal-decorated graphene nanoribbons and transition-metal-molecular sandwich nanowires contain first-row transition metal atoms. In previous work PBE functional is widely applied in ab initio calculations on similar systems and it is used in most of the study in this thesis.

1.6 References

1. P. Hohenberg, and W. Kohn, *Physical Review* **136**, B864 (1964).113
2. W. Kohn, and L. J. Sham, *Physical Review* **140**, A1133 (1965).
3. E. Kaxiras, *Atomic and electronic structure of solids* (Cambridge University Press, Cambridge, UK; New York, 2003).
4. J. P. Perdew, and A. Zunger, *Physical Review B* **23**, 5048 (1981)
5. Vosko, S. H., Wilk, L., Nusair, M. *Can. J. Phys.*, **1980**, 58, 1200.
6. R. M. Martin, *Electronic structure: basic theory and practical methods* (Cambridge University Press, Cambridge, UK; New York, 2004).
7. J. P. Perdew, and Y. Wang, *Physical Review B* **45**, 13244 (1992).
8. A. D. Becke, *Physical Review A* **38**, 3098 (1988).
9. Lee, C., Yang, W., Parr, R. G. *Phys. Rev. B* **1988**, 37, 785.
10. J. P. Perdew, K. Burke, and M. Ernzerhof, *Physical Review Letters* **77**, 3865 (1996).
11. (a) Becke, A. D. *Phys. Rev. A* **1988**, 38, 3098; (b) Lee, C., Yang, W., Parr, R. G. *Phys. Rev. B* **1988**, 37, 785.
12. Becke, A.D. *J. Chem. Phys.* **1997**, 107, 8554.
13. Slater, J. C. *Phys. Rev.* **1930**, 36, 57.
14. Frisch, J. *et al. GAUSSIAN 03* (Gaussian, Pittsburgh), Revision D. 01, 2003.

2 Edge-decorated Graphene Nanoribbons

2.1 Introduction

Graphene, a single layer of graphite, has attracted considerable research interests owing to its novel physical properties, such as massless Dirac fermions behavior [1-5], room-temperature quantum hall effect [6, 7] and high mobility and coherence [8]. The two-dimensional (2D) graphene sheet itself is a semi-metal. However, when the 2D sheet is cut into rectangle slices, namely, graphene nanoribbons (GNRs), they can become semiconductors with their energy band gap depending on the width of the nanoribbons as well as the crystallographic orientation of cutting edge. Hence, the GNRs possess more tunable electronic properties, rendering GNR-based nano-electronic devices conceivable [9-20].

Several recent theoretical studies have also revealed that zigzag edged GNRs (ZGNRs) can be converted into a half metal by either applying an external electric field or through chemical modification of the edges. Half metals hold the promise for spintronic applications [18, 21-27] as the electric current can be fully spin polarized when going through half metals. This is because for a half metal, one electron spin channel is insulating while the other channel is metallic. Son *et al.* were the first to show that half-metallicity can be achieved in a ZGNR by applying a strong in-plane transverse electric field [24]. The external electric field induces an electrostatic-potential difference between the two edges of the ZGNR, resulting in a spin-polarized band crossing the Fermi level. An important physical insight attained from this study is that it is the electrostatic potential difference between the two edges of a ZGNR is a prerequisite in achieving half metallicity. Inspired by this study, Kan *et al.* found an alternative

way to design GNR-based half metals. They showed that if the two edges of a ZGNR can be decorated with NO_2 and CH_3 chemical function groups, respectively, the ZGNR can become half metallic [26]. Indeed, the chemical modification can elevate certain spin-polarized bands crossing the Fermi level. However, the large steric interactions between neighbor groups make the system distorted. Hence, our design is mainly focused on single-atom and two-atom functional groups for the chemical functionalization. Here we will present a systematic study of electronic structures of ZGNR whose edges are decorated with various chemical functional groups and try to obtain half-metallicity in those systems. In addition, we will also show that ZGNRs decorated by some transition metal atoms can be a medium for planar tetracoordinate carbon strips, or functional materials that can be applied for hydrogen storage.

2.2 Computational Details

The density function theory (DFT) calculations are carried out using Dmol3 package [27-29]. The generalized gradient approximation (GGA) in the Perdew-Burke-Ernzerhof (PBE) form and an all-electron double numerical basis set with polarized function (DNP basis set) were chosen for the spin-unrestricted DFT computation [30]. The real-space global cutoff radius is set to be 3.7 Å. To simulate ZGNRs, a cuboid supercell with dimension $36 \times 16 \times c$ Å³ with one periodic length, or $36 \times 16 \times 2c$ Å³ with two periodic lengths, or $36 \times 16 \times 3c$ Å³ with three periodic lengths was opted, where c is the length of a unit cell along the ribbon direction. The nearest distance between two neighboring GNR is greater than 16 Å. For geometric optimization, the Brillouin zone was sampled by $1 \times 20 \times 1$ k points using the Monkhorst-pack scheme [31], and the forces on all atoms were optimized to be less than 0.005 eV/Å.

2.3 Half-metallicity in Edge-decorated ZGNRs

We examined a number of functional groups and found that the OH group is an effective electron-donating group for functionalizing one edge, and F atom is a weak electron-accepting group for the other. We can judge whether a chemical group is electron-donating or accepting by attaching it on benzene and calculate the total charge on the group and adjacent carbon atom. For example, by Hirshfeld analysis, in benzene decorated by $-OH$, the total charge on $-OH$ and adjacent carbon is $-0.18e+0.17e+0.07e=0.06e$ so it is electron-donating; for benzene decorated by $-F$, this value is $-0.09e+0.08e=-0.01e$ so it is weakly electron-accepting. Hereafter, we label a GNR with n zig-zag chains as n -ZGNR. Figure 1(a-c) shows the chemically modified 8-ZGNRs with one edge fully modified by OH groups and another by F, Cl or Br atoms, and their calculated spin-resolved electronic band structures. It is revealed that only edge modification by F atoms leads to a semiconducting spin channel while others all lead to metallic channels.

As the width of F-modified ZGNR is prolonged to 16, as shown in Fig. 1(d), its electronic band structure indicates that the chemically modified ZGNR becomes a half metal. Dependence of the spin-resolved band gap on the width of ZGNRs is shown in Fig. 1(d). Here, the gap-opening channel is designated as α spin channel and the gap-narrowing channel is designated as the β spin channel. As the width of ZGNRs increases, band gaps of both spin channels are reduced, and the band gap of the β spin channel is closed at $n = 16$. In the latter case, the potential difference due to the edge modification is sufficiently large to push the edge state to the Fermi level, resulting in half metallicity. Figure 1(d) shows that narrow-width edge-modified ZGNRs ($n < 16$) are typically spin-polarized semiconductors whereas wide-width ZGNRs ($n > 16$) are half metals.

An important implication derived from Fig. 1(d) is that if the width of a ZGNR is sufficiently large, half metallicity might be achievable even with weaker electron-donating group for edge modification. To confirm this postulation, we replaced the OH groups by H atoms for edge modification. As shown in Fig. 2 (a), (b), the chemically modified 8-ZGNR is still a semiconductor with trivial spin-polarization, but the 72-ZGNR becomes half metallic. Figures 2(c) confirm that the band gap of β spin channel decreases with increasing n , and is closed when $n = 72$, a critical value beyond which the ZGNR becomes half metallic.

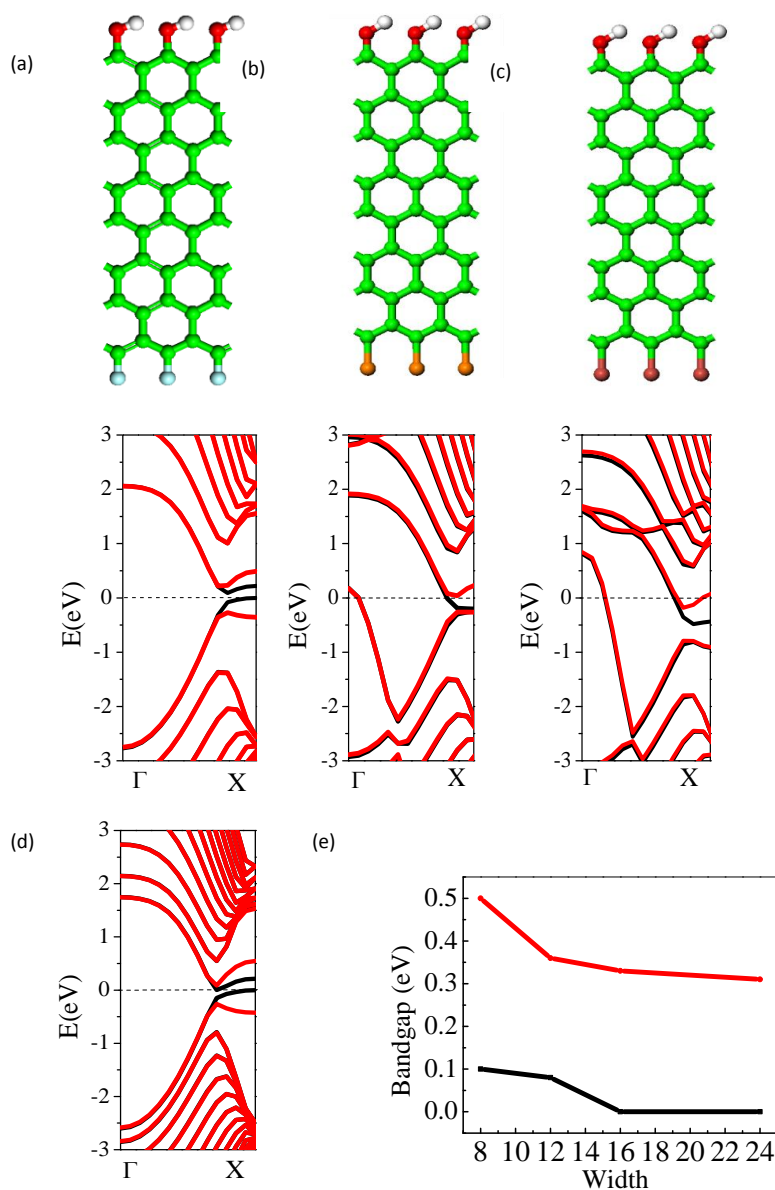


Figure 1 Geometric structure and electronic band structure of an 8-ZGNR with edges chemically modified by OH and (a) F, (b) Cl, and (c) Br, respectively. The green, red, blue, orange, red-brown and white spheres denote C, O, F, Cl, Br and H atoms, respectively. (d) Electronic band structure of 16-ZGNR modified by OH and F. (e) Spin-resolved band gap versus the width of ZGNR. Red and black lines denote α and β spin channel, respectively.

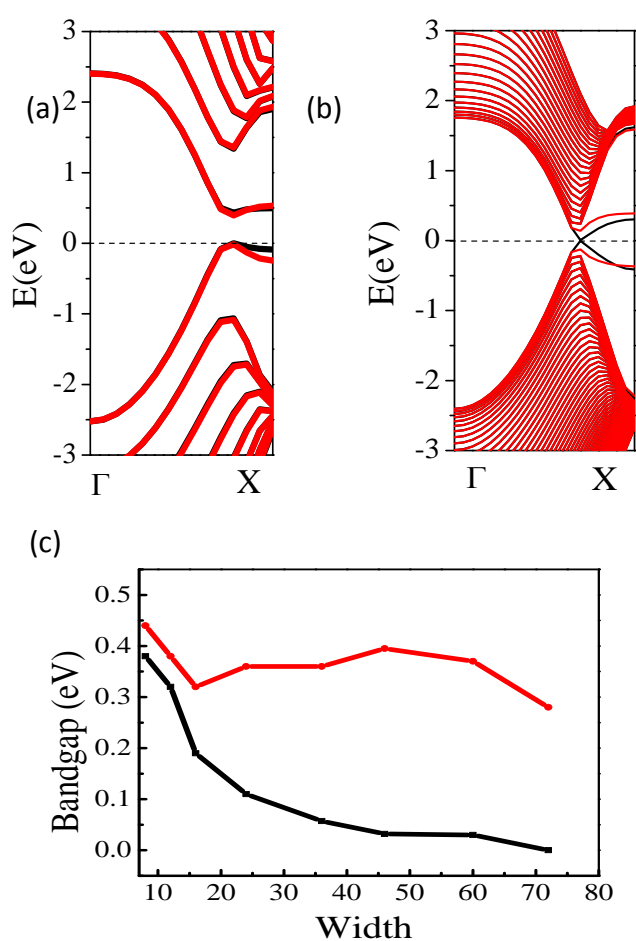


Figure 2 Electronic band structures of (a) 8-ZGNR and (b) 72-ZGNR, with edge modified by H and F, respectively. (c) Spin-resolved band gap versus the width of ZGNR. Red and black lines denote α and β spin channel, respectively.

Because $-F$ group is not effective on narrow ZGNRs we need to study more functional groups. First, we show electronic properties of an 8-ZGNR modified with the same type of functional groups at both edges (homogeneous edge decoration). Figure 3 displays the optimized geometric structures, the computed electronic band structures, as well as the partial density of states (PDOS) of the chemical groups and carbon atoms at the edges of several chemically modified 8-ZGNRs. Note that a pristine 8-ZGNR is a semiconductor with a narrow direct band gap of ~ 0.45 eV. Figure 3(a) shows that the OH-decorated 8-ZGNR has a similar profile of electronic band structures as a pristine 8-ZGNR, but the electronic band gap is 0.17 eV less than that of the pristine 8-ZGNR. As shown in Figure 3(c) and (d), the three-atom NO_2 or SO_2 functional groups induce out-of-plane structural distortions near each edge site due to strong repulsive (steric) interactions among nearest-neighbor functional groups. In addition, the optimized supercell length along the ribbon direction increases from 4.93 Å (in the pristine ribbon) to 4.97 Å. The edge modified 8-ZGNR by either NO_2 or SO_2 groups is still a semiconductor but with an indirect band gap of 0.26 eV. The PDOS plots in Figure 3 (a) – (d) show that the states near the Fermi level are mainly contributed by edge C rather than the functional groups are. In contrast, the CN decorated 8-ZGNR is a semimetal because of the appearance of certain impurity states that cross the Fermi level. These impurity states are mainly induced by CN groups.

The average substitution energy per functional group X for the replacement of hydrogen atoms H by functional groups X is defined as

$$E_s = (E(X - \text{ZGNR}) + mE(\text{H}) - E(\text{H} - \text{ZGNR}) - mE(X))/m,$$

where $E(\text{system})$ is the total energy of the system per supercell, X denotes the functional group (OH, SO_2 , NO_2 , or CN), H the hydrogen atom, and m the number of functional groups per supercell. The calculated average substitution energies per functional group are -0.17, 3.62, 2.83 and -1.30 eV for OH, NO_2 , SO_2 and CN group, respectively. The positive E_s in the case of NO_2 or SO_2 reflects the energy cost due to the local out-of-plane structural distortion at each edge site.

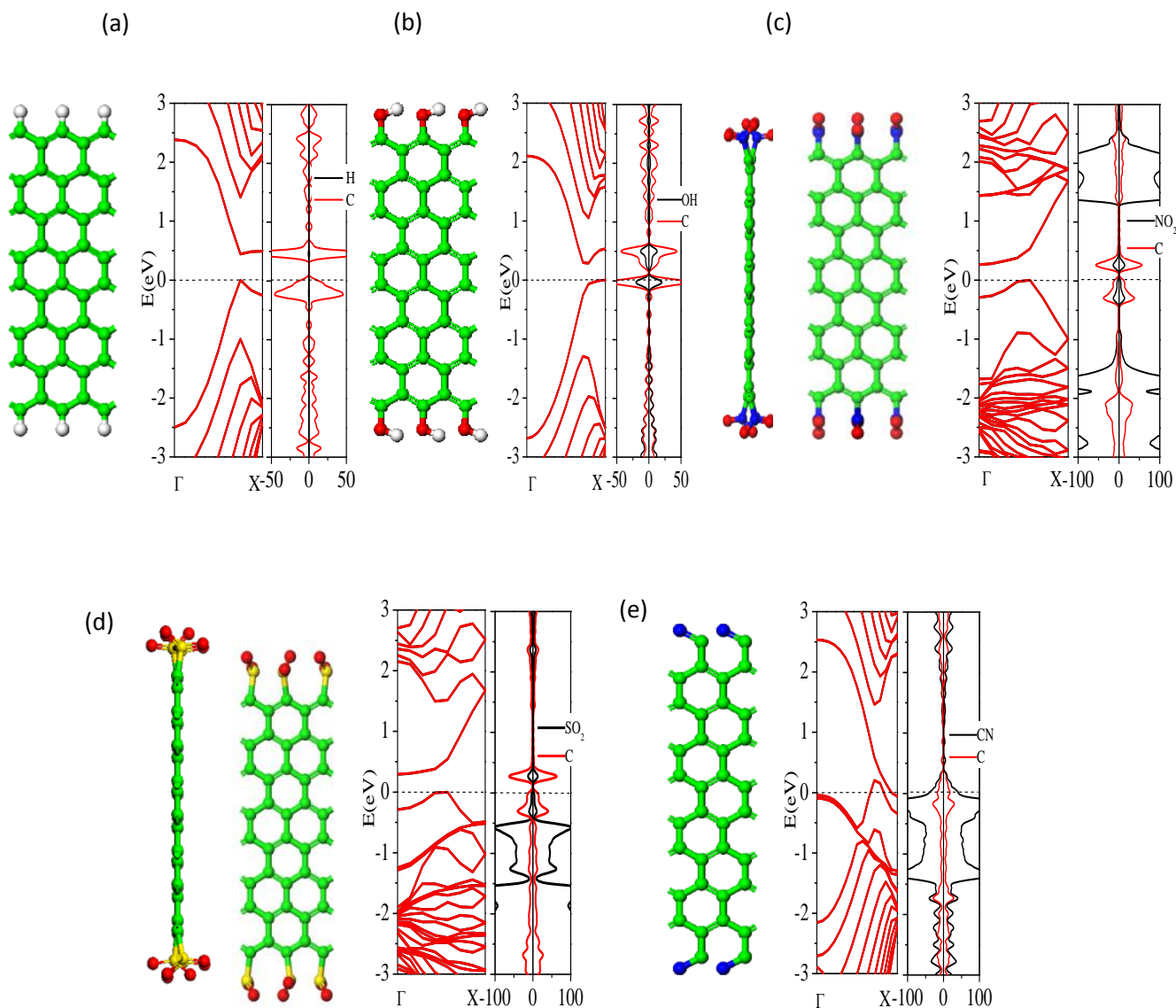


Figure 3 Geometric structures, electronic band structures, and PDOS of functional groups and carbon atoms at the edges of 8-ZGNRs. The two edges are uniformly decorated by (a) H, (b) OH, (c) NO₂, (d) SO₂, and (e) CN groups. In the PDOS plots, positive region represents the spin-up channel and negative region represents the spin-down channel. The optimized value of unit cell length c in the ribbon direction is (a) 2.465 Å, (b) 2.465 Å, (c) 2.485 Å, (d) 2.485 Å, and (e) 2.465 Å, respectively. Color code: C (green), H (white), O (red), N (blue), and yellow). Out-of-plane structural distortions at the two edges can be seen in side view of the structure in (c) and (d).

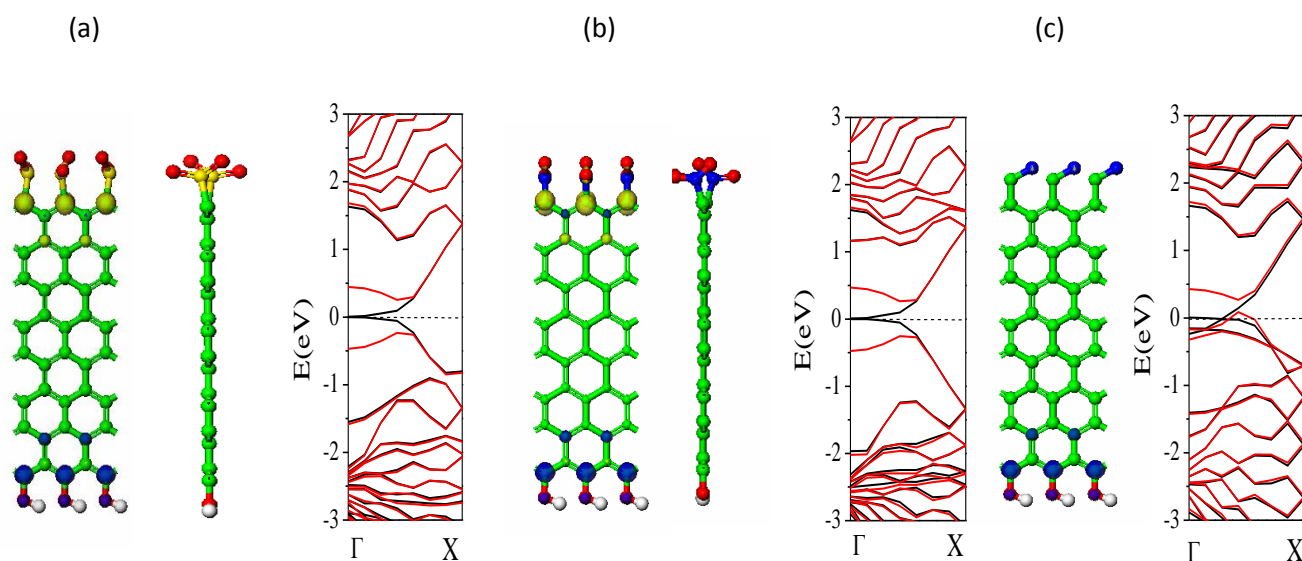


Figure 4 Geometric structures, spin densities, and electronic band structures of 8-ZGNRs. The two edges are decorated by (a) SO₂/OH groups, (b) NO₂/OH groups, or (c) CN/OH groups. The S-S distance is 2.085 Å in (a). The larger dark blue and yellow spheres represent spin-up and spin-down local state, respectively. The isovalues of spin density is [-0.03, 0.03]. In the corresponding band structure plots, black lines represent the spin-up channel and red lines represent the spin-down channel.

Now we show electronic properties of the 8-ZGNR decorated by OH functional groups at one edge and by the SO₂, NO₂, or CN groups at the other edge. These edge decorated ribbons are labeled as OH/X-8-ZGNR ($X = \text{SO}_2, \text{NO}_2, \text{CN}$). The optimized structures and computed electronic band structures of OH-X-8-ZGNR are shown in Figure 4. The DFT calculations suggest that the

OH/SO₂-8-ZGNR and OH/NO₂-8-ZGNR are half metallic, as the conduction and valence band edge of one spin channel cross the Fermi level, whereas in the other spin channel an indirect band gap of ~ 0.5 eV shows up. Again, the relatively larger three-atom NO₂ or SO₂ functional groups induce out-of-plane structural distortions near each edge sites. In contrast, the OH/CN-8ZGNR is predicted to be metallic, similar to the homogeneous edge decoration of the 8-ZGNR with the CN groups.

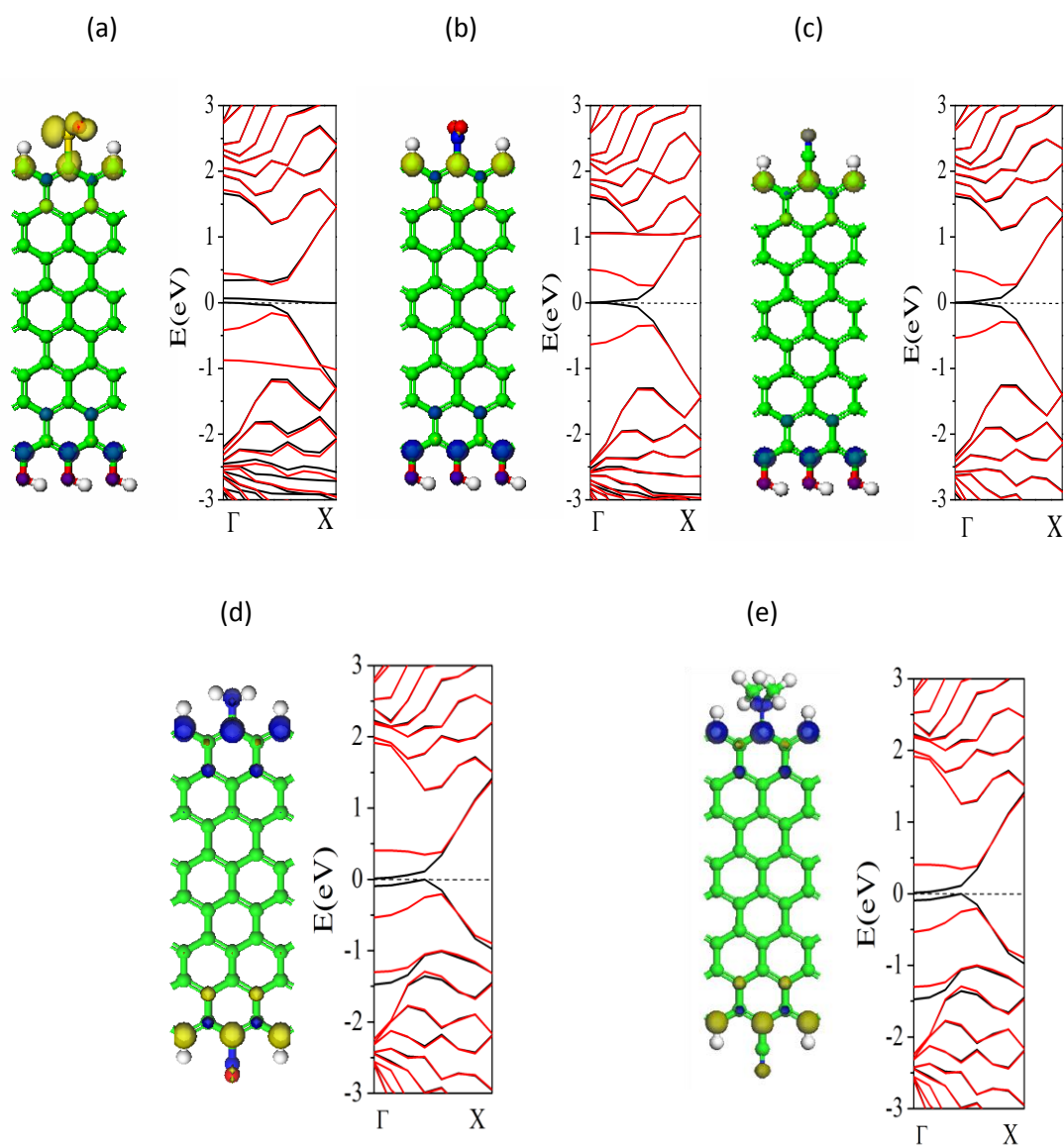


Figure 5 The structures, spin density and band structures of ZGNR modified by (a) $\text{SO}_2+\text{H}/\text{OH}$, (b) $\text{NO}_2+\text{H}/\text{OH}$, (c) $\text{CN}+\text{H}/\text{OH}$, (d) $\text{NO}_2+\text{H}/\text{NH}_2+\text{H}$, and (e) $\text{CN}+\text{H}/\text{N}(\text{CH}_3)_2+\text{H}$. Green, white, blue, yellow and red balls denote carbon, hydrogen, nitrogen, sulfur and oxygen atoms, and for spin density blue and yellow represent spin-up and spin-down respectively and the range of the isovalues of spin density is $[-0.03, 0.03]$. In band structure graphs black represents the spin-up channel and red represents the spin-down channel.

One way to alleviate the strong steric repulsion between nearest-neighbor functional groups at the edges is to reduce the composition of the three-atom functional group (such as SO_2 , NO_2) at an edge, e.g., by replacing every other SO_2 or NO_2 group with a smaller hydrogen atom for the edge decoration (see Figure 5). Clearly, the replacement of a larger functional group by the much smaller H atom completely removes the local out-of-plane structural distortion occurred in fully decorated ZGRNs. The calculated average binding energies are 3.46 and 2.35 eV for SO_2 and NO_2 , respectively, in the case of hybrid edge decoration with H. Both binding-energy values are greater than those in fully decorated ZGRNs, suggesting that the removal of local structural distortions via introducing H atoms actually increases the stability of the system.

In addition, the hybrid decoration with H and X (= SO_2 , NO_2 , or CN) at one edge may yield some new features in the electronic structure. For example, the ribbon $\text{NO}_2+\text{H}/\text{OH}$ -8-ZGNR has similar band structures near the Fermi level as the NO_2/OH -8ZGNR [see Figures 4(b) and 5(b)]. However, the DFT calculation suggests that $\text{CN}+\text{H}/\text{OH}$ -8-ZGNR is half metallic [see Figure 5(c)] even though the CN/OH -8-ZGNR is metallic [Figure 4(c)]. More interestingly, for the $\text{H}+\text{SO}_2/\text{OH}$ -8-ZGNR, the computed electronic structure [Figure 5(a)] suggested it is a different type half metal from SO_2/OH -8-ZGNR [figure 4(a)]. For the latter, the spin-up channel shows a *direct* zero band-gap, whereas for the $\text{H}+\text{SO}_2/\text{OH}$ -8-ZGNR, the spin-up channel shows an *indirect* zero

band-gap. In other words, for H+SO₂/OH-8-ZGNR, an impurity state is induced at the Fermi level, resulting in a new type of half-metallicity. Note that the SO₂/OH-8ZGNR has a similar electronic structure as NO₂+H/OH-8-ZGNR.

Besides the electron accepting groups, the electron donating groups e.g. OH can be also replaced by hybrid NH₂ groups plus H atoms or N(CH₃)₂ groups plus H atoms [See Figure 5(d) and (e)]. For example, when the OH groups in H+NO₂/OH-8-ZGNR and H+CN/OH-8-ZGNR are fully replaced by NH₂+H or N(CH₃)₂+H groups, the DFT calculations suggest that the ribbons are still half metallic. However, instead of direct zero band-gap in the spin-up channel, both new edge-decorated ribbons exhibit indirect zero band-gap in the spin-up channel [see Figure 5(d) and (e)].

The three distinct zero band-gap features in the electronic structures can be attributed to two underlying mechanisms for achieving half metallicity. The first mechanism is already known, that is, the band gap closing in one spin channel is due to the merging of conduction and covalent band edges at Fermi level, stemming from the chemical potential difference between two edges. The zero band-gap can be either direct, as shown in Figures 4(a), 4(b), 5(b) and 5(c), or indirect, as shown in Figure 5(d) and 5(e). The second mechanism appears to be a new one. As shown in Figure 3(a), a new state is induced at the Fermi level in one spin channel, resulting in zero band gap. The difference in the two mechanisms can be also reflected in the spin charge density distribution. In the first, the spin charge density is mainly contributed by carbon atoms at the edges, whereas in the second, the spin charge density is contributed by both the SO₂ groups and carbon atoms at the edges [see Figure 5(a)].

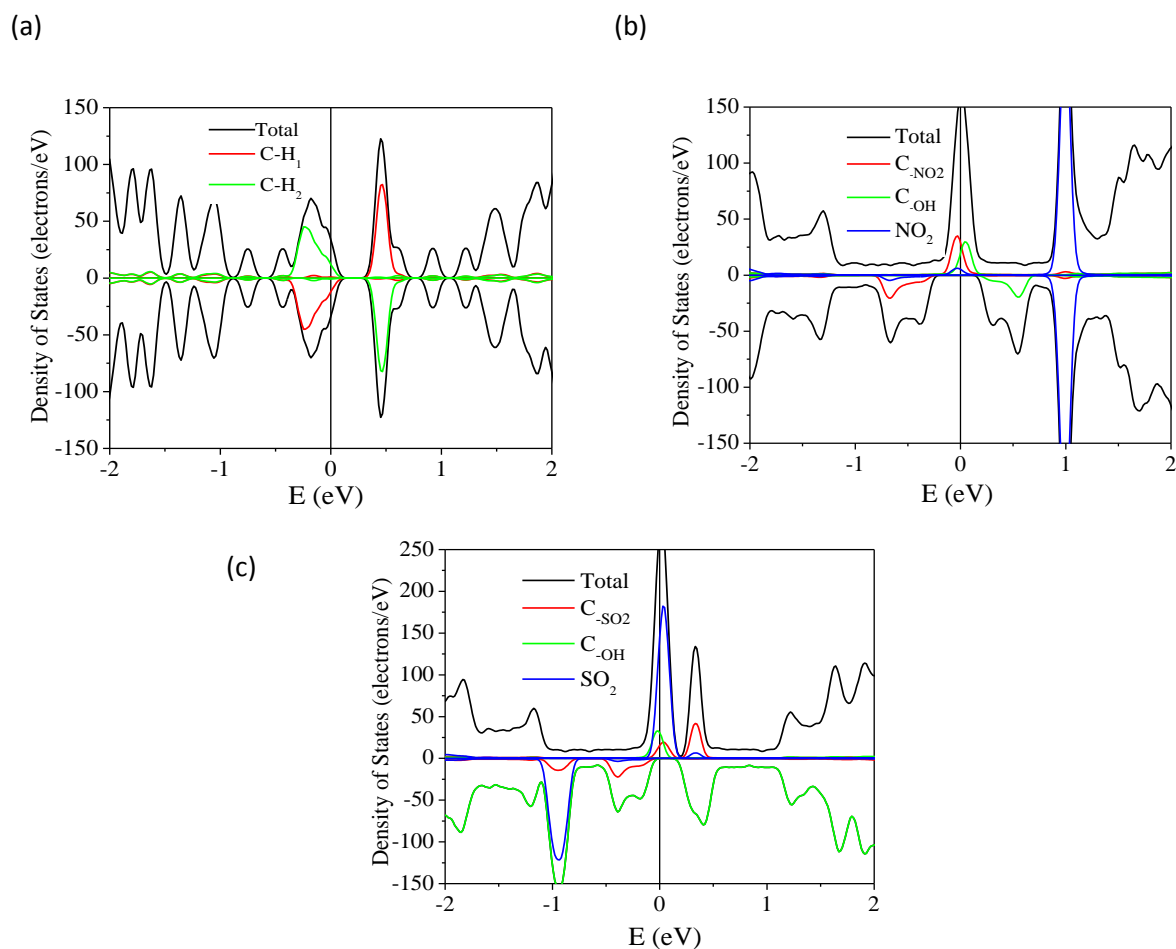


Figure 6 Partial density of states of (a) two C-H atoms and 2 total units in hydrogenated ZGNR; (b) C-NO₂, C-OH, NO₂ group and 2 total units of ZGNRs modified by NO₂/H-OH pair; (c) C-SO₂, C-OH, SO₂ group and 2 total units of ZGNRs modified by SO₂/H-OH pair. Positive represents the spin-up channel and negative represents the spin-down channel.

To further illustrate the difference between the two mechanisms, the projected density of states (PDOS) on the functional groups and carbon atoms at the edges of a pure 8-ZGNR,

H+NO₂/OH-8-ZGNR, and H+SO₂/OH-8-ZGNR are plotted in Figure 6, respectively. For the pure 8-ZGNR [Figure 6(a)], the carbon atoms at the edges contribute two separated conduction and valence PDOS peaks near the Fermi level. These peaks show mirror symmetry with respect to the horizontal axis and thus, the pure ZGNR is a spin-nonpolarized semiconductor. For H+NO₂/OH-8-ZGNR [Figure 6(b)], the PDOS peaks near the Fermi level contributed by the carbon atoms bonded to NO₂ (C-NO₂) are shifted downward, with respect to the Fermi level, while those peaks contributed by the carbon atoms bonded to OH (C-OH) are shifted upward. Both shifts are due to the chemical potential difference between the two edges. In this case, no PDOS peak near the Fermi level is contributed by NO₂ and OH groups. On the other hand, for H+SO₂/OH-8-ZGNR [Figure 6(c)], the PDOS peaks near the Fermi level contributed by C-OH are shifted upward, similar to that in H-NO₂/OH-8-ZGNR, but the PDOS peaks contributed by C-SO₂ retain their positions in energy. Instead, a new impurity state in one spin channel appears with the band gap. Hence, the PDOS analysis suggests that the impurity state mainly originate from a coupling between carbon atoms at the edge with SO₂ functional groups. The notable spin charge density distribution over SO₂ functional groups is consistent with this conclusion.

Ratio of H vs. SO ₂	0 (SO ₂ only)	1:2	1:1	2:1
C-S Bond length (Å)	1.786	1.778	1.836	1.839
Substitution energy E_s (eV)	3.62	2.80	3.46	3.11

Table 1 The C-S bond lengths and average substitution energies of SO₂ at different ratios of H/SO₂ in H+SO₂/OH-8-ZGNR.

It is expected that the exact 1:1 ratio of SO_2 vs. H is difficult to realize in experiments. Hence we also investigated electronic structures of $\text{H}+\text{SO}_2/\text{OH}$ -8-ZGNR with different ratios of H/SO_2 . The optimized geometric structures, computed band structures and DOS of $\text{H}+\text{SO}_2/\text{OH}$ -8-ZGNR with H/SO_2 ratio of 1:2 and 2:1, respectively, are shown in Figure 7. The average substitution energy of the SO_2 functional groups in place of H atoms, and the C-S bond lengths at different H/SO_2 ratios are summarized in Table I. It is found that when H/SO_2 ratio = 2:1, where two H atoms are located between two SO_2 functional groups, as shown in Figure 7(a), the average substitution energy per SO_2 in $\text{H}+\text{SO}_2/\text{OH}$ -8-ZGNR is the second lowest while the C-S bond length is the longest. More interestingly, as shown in Figure 7(b), when two side-by-side SO_2 functional groups form a pair and one H atom is located between the two SO_2 pairs, no out-of-plane structural distortion of S atoms was observed in this case. This is because the two S atoms adjust their in-plane position [the S-S distance is 2.262 Å, compared to 2.085 Å in Figure 2(a)] to mitigate the strong steric interaction. Indeed, as shown in Table 1, the substitution energy per SO_2 in this case is the lowest, indicating that this configuration is the most stable.

Again, the calculated band structures suggest that all $\text{H}+\text{SO}_2/\text{OH}$ -8-ZGNR with the H/SO_2 ratio between 1:2 and 2:1 are half metallic. The calculated band gaps in the semiconducting spin channel are 0.3 and 0.5 eV for H/SO_2 ratio = 2:1 and 1:2, respectively. When H/SO_2 ratio is 2:1, an impurity state is introduced at the Fermi level and a large spin charge density is distributed over SO_2 functional groups, as in the case of H/SO_2 ratio = 1:1. On the other hand, when H/SO_2 ratio is 1:2, at which the SO_2 pair is formed, the band structures exhibits similar profiles as those of OH/SO_2 -8-ZGNR and the spin charge density mainly distribute over carbon atoms at

the edges. Remarkably, the transition between the two mechanisms for half-metallicity can be controlled by changing the H/SO₂ ratio for edge decoration.

In general, when SO₂ functional groups are separated by H atoms, the SO₂ functional groups tend to introduce some impurity states at the Fermi level (impurity-state mechanism). When SO₂ functional groups form pairs, they tend to create sufficiently large chemical potential (together with OH functional groups at the opposing edge) between the two edges (chemical-potential mechanism). To verify this physical picture, we performed a test calculation for an 8-ZGNR with one edge decorated by SO₂ functional groups and the other edge by H atoms (non-electron-donating groups). As shown in Figure 8(a) and (b), the impurity states are introduced in the H+SO₂/H-8-ZGNRs with H/SO₂ ratio at one edge being 1:1 or 2:1, i.e. the impurity-state mechanism prevails. However, when the H/SO₂ ratio is 1:2, the chemical-potential mechanism prevails, as shown in Figure 8(c).

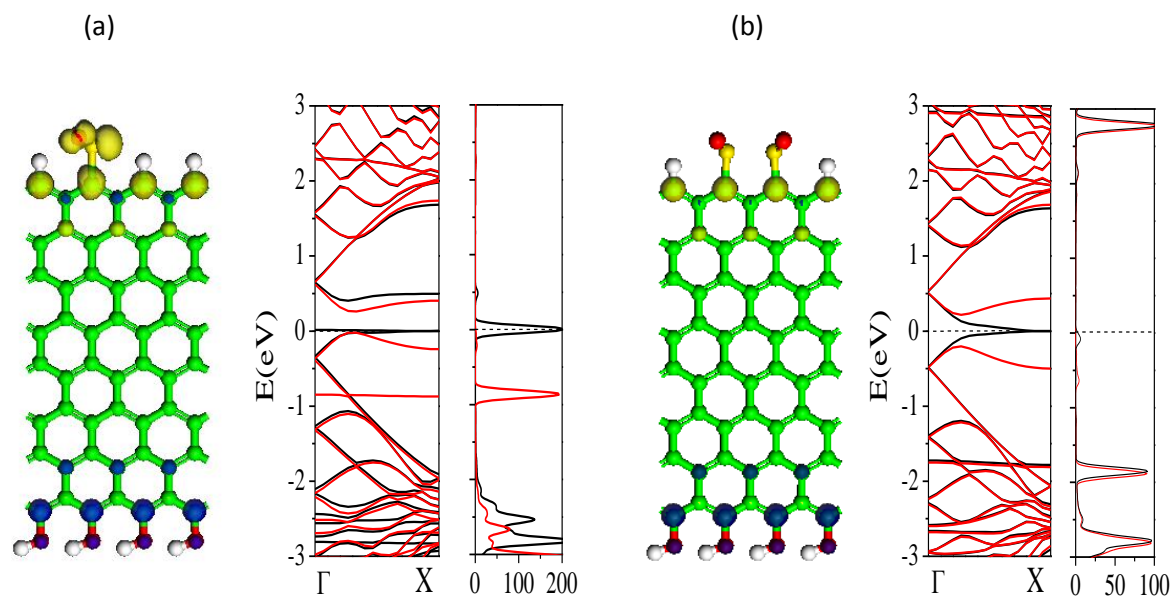


Figure 7 The spin density, band structures and the partial density of states distributed by SO_2 of 8-ZGNRs modified by OH-H/ SO_2 pair when the ratio of H/ SO_2 equals (a) 1:2 and (b) 2:1. The S-S distance is 2.262 Å in (b). Green, white, yellow and red balls denote carbon, hydrogen, sulfur and oxygen atoms, and for spin density blue and yellow represent spin-up and spin-down and the range of the isovalues of spin density is [-0.03, 0.03]. In both band structure and density of state graphs black represents the spin-up channel and red represents the spin-down channel.

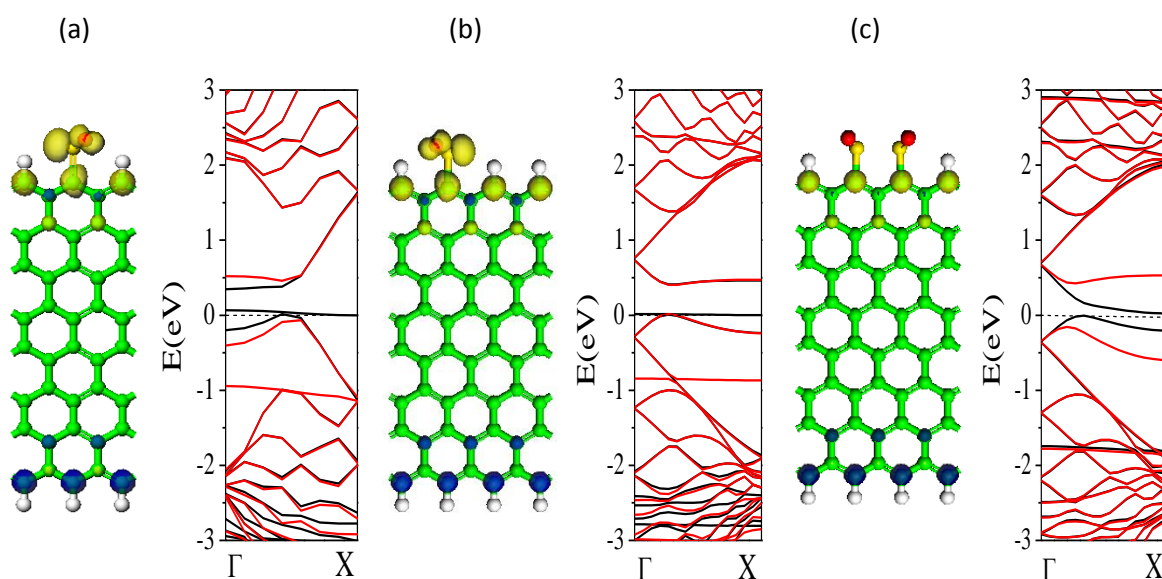


Figure 8 The spin density and band structures of ZGNR modified by H-H/ SO_2 pair when the ratio of H/ SO_2 equals (a)1, (b)2 and (c)1/2. Green, white, yellow and red balls denote carbon, hydrogen, sulfur and oxygen atoms, and for spin density blue and yellow represent spin-up and spin-down and the range of the isovalues of spin density is [-0.03, 0.03]. In band structure graphs black represents the spin-up channel and red represents the spin-down channel.

The impurity-state mechanism is likely due to the lone pair electrons of S atom in the SO₂ functional group which gives rise to the impurity state at the Fermi level. However, when two side-by-side SO₂ functional groups form a pair, the two neighboring S atoms form a weak S-S bond (with a bond length ~ 2.262 Å) and largely consume the lone pair electrons. Note that the S-S bond length 2.262 Å is shorter than the distance 2.46 Å between two neighboring carbon atoms at the edge.

The impurity-state mechanism is likely due to a lone pair of electrons of S atom in the SO₂ functional group which give rise to the impurity state at the Fermi level. However, when two side-by-side SO₂ functional groups form a pair, the two neighboring S atoms form a weak S-S bond (with a bond length ~ 2.262 Å) and consume the lone pair electrons, noting that the S-S bond length 2.262 Å is shorter than the distance 2.46 Å between two neighboring carbon atoms at the edge. A major advantage of the impurity-state mechanism is that the half-metallicity is insensitive to the potential difference between the two edges of a ZGNR. As such, with isolated SO₂ functional groups at one edge, the other edge of ZGNR can be decorated by a variety of functional groups such as F, H, or OH, to meet the specific needs for nanoelectronic applications. For example, as shown in Figure 9(a), the use of either H atoms as in H+SO₂/H-8-ZGNR or F atoms as in H+SO₂/F-8-ZGNR for decorating the opposing edge does not affect the underlying half-metallic property of the ribbon.

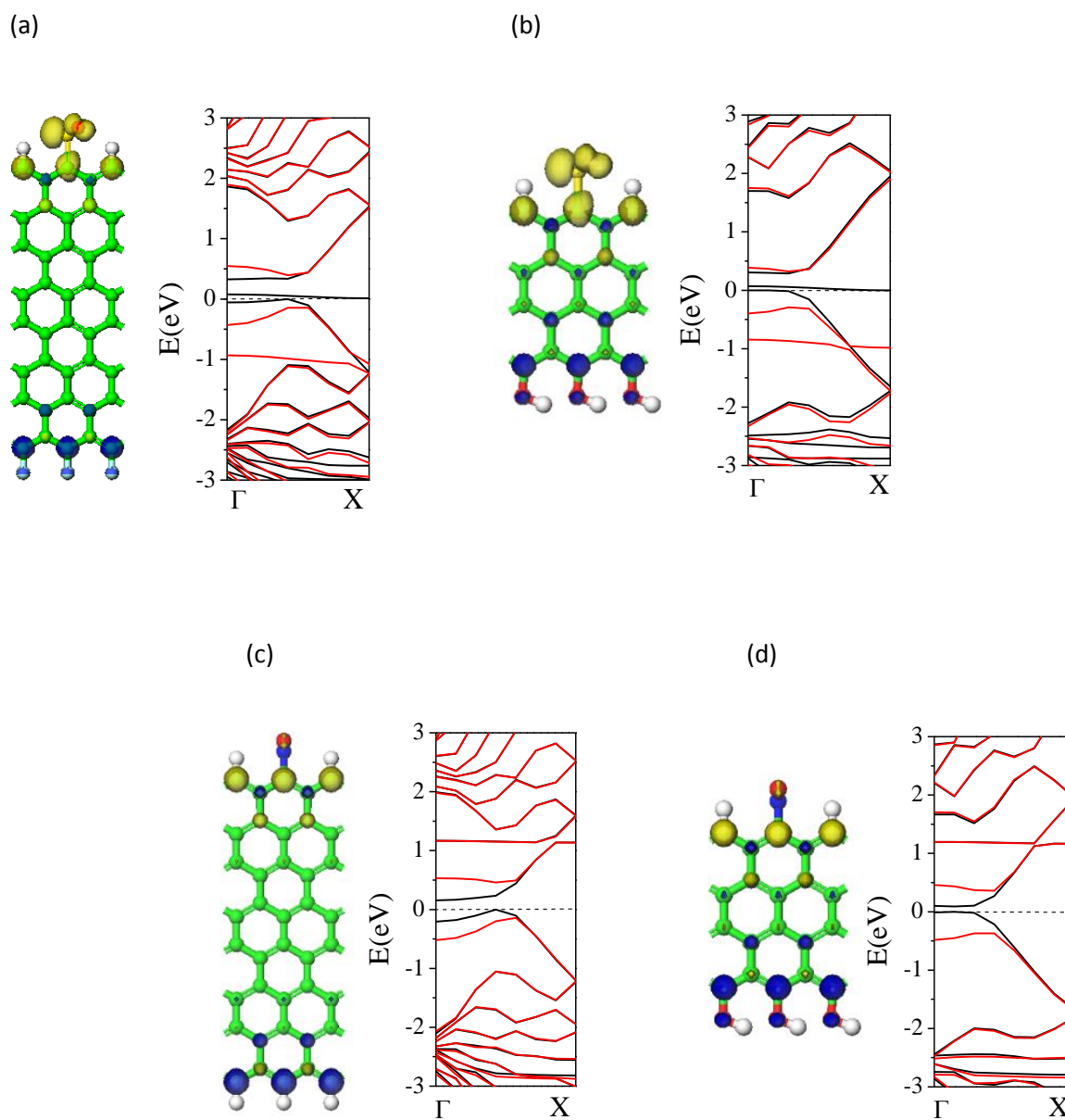


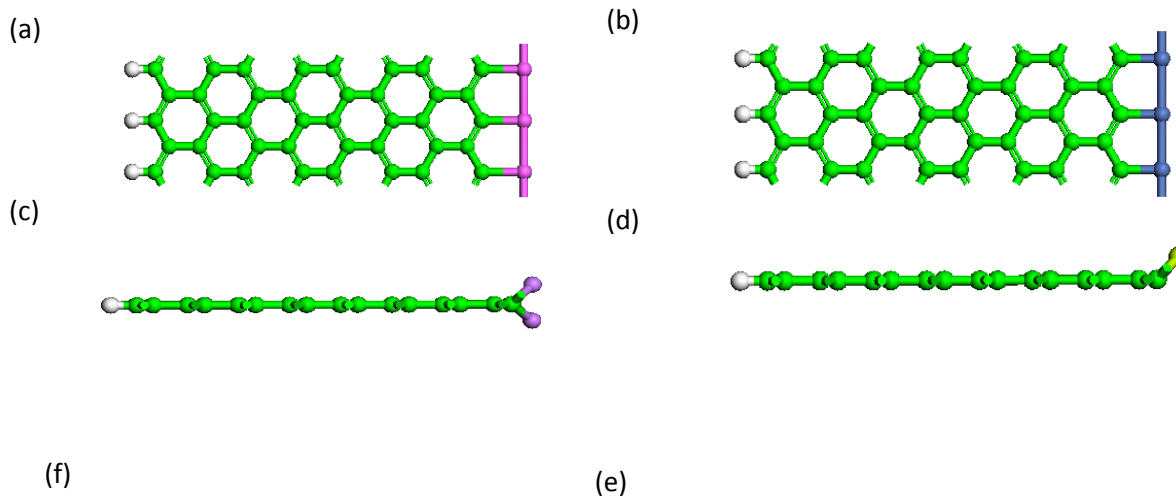
Figure 9 The spin density and band structures of ZGNR modified by (a)F-H/SO₂(n=8) ,(b)OH-H/SO₂(n=4) ,(c)H-H/NO₂(n=8) and (d)OH-H/NO₂(n=4). For spin density blue and yellow represent spin-up and spin-down respectively and the range of the isovalues of spin density is [-0.03, 0.03]. In band structure graphs black represents the spin-up channel and red represents the spin-down channel.

Another merit of the impurity-state mechanism is that the half-metallicity is insensitive to the width of nanoribbons. As shown in Figure 9(b), H+SO₂/OH-4-ZGNR has a width of $n = 4$, and yet it is still half metallic. In stark contrast, the half metallicity achieved via the chemical-potential mechanism can be quite sensitive to the selected functional groups and the width of nanoribbons. As a proof of principle, we considered the model system H+NO₂/OH-8-ZGNR shown in Figure 5(b). By replacing OH groups with H atoms as in H+NO₂/H-8-ZGNR or by reducing its width to $n = 4$ as in H+NO₂/OH-4-ZGNR, both systems lose the half metallicity and become spin-polarized semiconductors, as shown in Figure 9 (c) and (d), respectively.

2.4 Metal-decorated ZGNRs as Mediums for Planar Tetracoordinate Carbon Strips

The *spatial tetrahedral* coordination of saturated carbon has been a textbook concept since it was revealed independently by van't Hoff and Le Bel more than a century ago[32]. In 1970, Hoffmann and coworkers raised an intriguing question about stability of *planar tetracoordinate* carbon (ptC)[33]. A few years later, the first theoretical prediction and experimental isolation of ptC systems were reported[34]. Since then, exploration of unusual ptC systems has attracted considerable attention[35,36]. Numerous ptC-containing molecules have been predicted via molecular orbital (MO) calculations[35]. Some of these predicted ptC-containing molecules have been detected and even characterized in the laboratory[35,36]. Despite many ptC-containing molecules have been detected, existence of ptC-containing units in condensed matter has not been observed. Only a few ptC-containing extended systems have been theoretically predicted[37]. These extended systems are typically based on arrangement of molecular ptC

motifs such as CAI_4^{2-} , C_5^{2-} , or CB_4 [37]. Here we present *ab initio* calculation evidence of a *hitherto* unreported one-dimensional (1-D) ptC system – an infinite ptC strip embedded in an edge-decorated ZGNR. We first show that a 1-D ZGNR can be a unique host system for realization of extended ptC structure due to its highly delocalized in-plane π -electrons and intrinsic rigid structure. In principle, the stabilization of a ptC unit requires satisfaction of both geometrical and electronic conditions, besides being the most energetically stable structure against any spatial conformation or atomic exchange between the central carbon and any peripheral non-carbon atom. Because the structure of ZGNRs is mechanically robust, atomic exchange between an edge carbon atom and a peripheral metal atom would likely result in higher-energy structures. Hence, only the geometrical and electronic requirements should be met in order to realize the ptC-containing ZGNR. In most cases, edge decoration of a ZGNR by functional groups (FGs) such as $-H$, $-OH$ results in binding of each edge carbon atom with only one FG, as represented by $FG-ZGNR-FG$. The edge carbon atoms have sp^2 hybridization. To achieve a ptC strip at an edge of a ZGNR, each anchoring ligand (L) must bind with two edge carbon atoms, as denoted by $L\langle ZGNR \rangle L$.



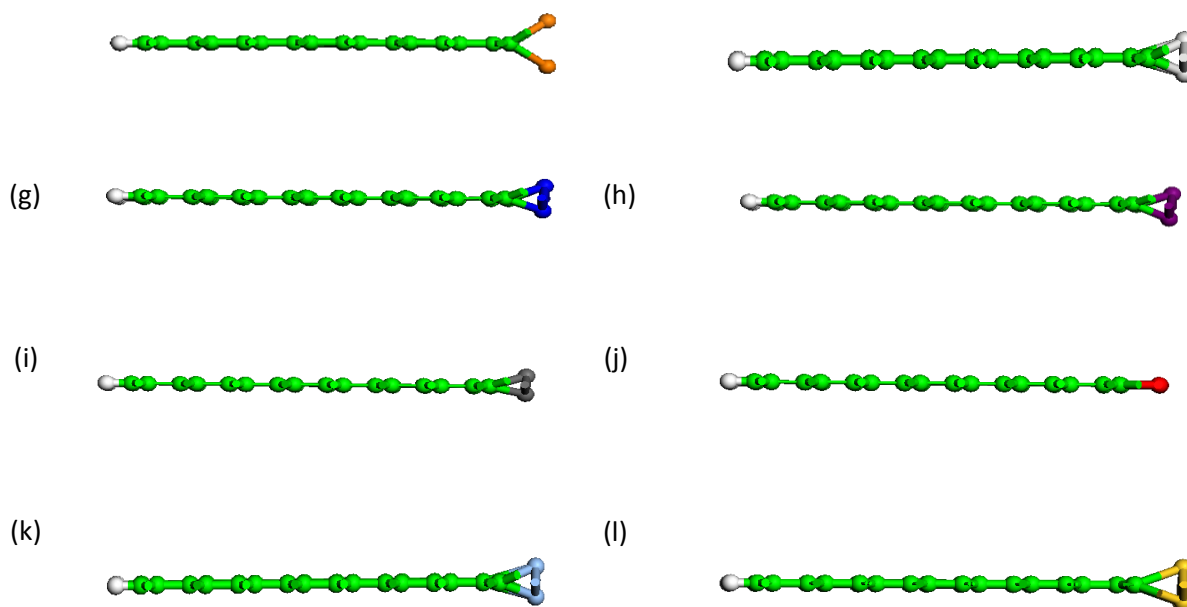


Figure 10. Optimized geometric structures of H-8-ZGNR>M for M= (a) Al, (b) Ni (top view of the plane of the systems), and for M= (c) Li, (d) Be, (e) Na, (f) Sc, (g) Ti, (h) Cr, (i) Fe, (j) Cu, (k) Ag and (l) Au (side view of the systems). In (a) and (b), all the edge carbons are sp^2 type, and in (c-l) all edge carbon atoms are tetracoordinated. But only in (j) these carbon atoms are co-planar with other atoms in the system.

We have examined a variety of main-group metal atoms such as Li, Be, Na, Al, transition metal atoms such as Sc, Ti, Cr, Fe, Ni, and noble metals Cu, Ag, Au for edge decoration. The metal atoms form a stable 1-D metal wire at each edge of ZGNRs. However, the geometric optimization and frequency calculations suggest that none forms perfectly planar L<ZGNR>L like systems except the Cu-decorated ZGNR. The most stable structure of Al- and Ni-decorated ZGNRs favors L-ZGNR-L like structure with each metal atom binding to a single carbon atom. For other metal decorations (cf. Figure 10), all metal atoms form irregular out-of-plane structures.

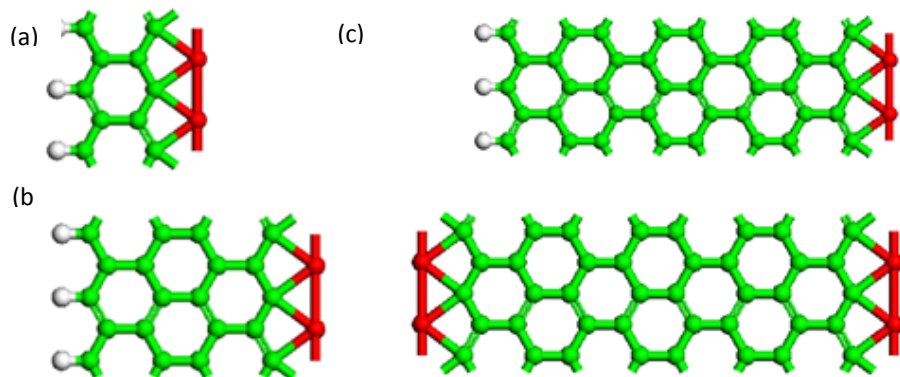


Figure 11. Optimized geometric structures of n -ZGNRs (a unit cell) with one (or two) edge(s) decorated by Cu. The width n is (a) 2, (b) 4, and (c) and (d) 8, respectively. Green, red and white balls denote carbon, copper and hydrogen atoms, respectively. The ZGNR with one edge decorated by Cu and another by H is denoted as H-ZGNR>Cu (a-c), and with both edges decorated by Cu is denoted as Cu<ZGNR>Cu in (d).

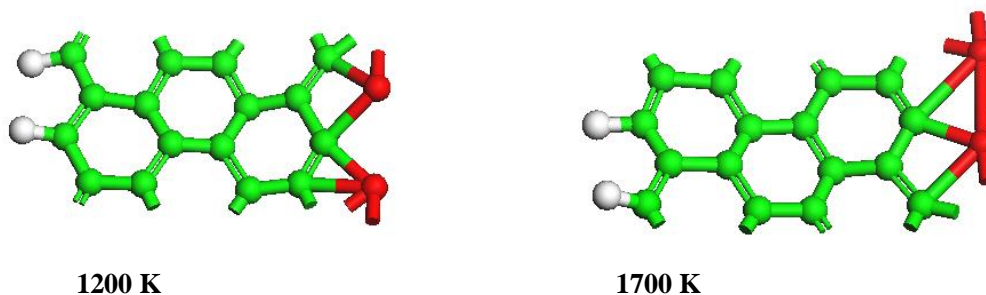


Figure 12. A snapshot of the equilibrium structure of H-4-ZGNR>Cu at 1200 K and 1700 K, respectively, at the end of 5ps quantum MD simulations. The NVT MD is carried out using the Dmol3 package. The Nosé-Hoover chain method is used for temperature control. The Nosé Q ratio is set 2.0 and the Nosé chain length is 2.

Hereafter, we focus on edge decorated ZGNRs by Cu, which give rise to one or two stable ptC strips denoted as either H- n -ZGNR>Cu or Cu< n -ZGNR>Cu (see Figure 11). These ptC-containing planar structures are highly stable, regardless of the width of ZGNRs. An independent geometric optimization and frequency calculation on the Cu<8-ZGNR>Cu system and no imaginary frequencies were found. The stability of Cu<ZGNR>Cu systems is also reflected from

relatively large binding energy (E_b) of a Cu atom to the edge of ZGNRs. The computed E_b is 3.66 eV per Cu atom, notably greater than the cohesive energy (3.36 eV/atom) of bulk Cu solid. Although such a binding energy is still much smaller than that of non-metal functional groups such as $-H$ (5.09 eV) and $-OH$ (5.26 eV), the E_b can increase up to 4.22 eV/atom when two H-ZGNR>Cu fuse together at the edges. Moreover, our calculations of binding energies per Cu atom with Cu atoms located on various positions indicate the binding of Cu atoms at the edge leads to the most stable structure. We also examined thermodynamic stability of the ptC strip at the edge of ZGNR using the Born-Oppenheimer quantum molecular dynamics (MD) simulation[38]. The snapshot of the equilibrium structure at the end of each MD simulation on the H-4-ZGNR>Cu system at 1200 and 1700 K, respectively (each for 2 ps), is shown in Figure 12, which suggested that the ptC structure can be still intact for 2 ps even at 1700 K.

Table 2. Van der Waals (vdW) radii, covalent radii, and M-M bond length in the bulk structure of various metal elements.

<i>Elements</i>	Au	Ag	Al	Be	Cr	Cu
vdW radii (Å)	1.66	1.72	2.00	2.00	2.00	1.40
Covalent radii (Å)	1.36	1.45	0.96	0.96	1.39	1.32
M-M length in bulk (Å)	2.88	2.89	2.86	2.22	2.50 and 2.88	2.55
<i>Elements</i>	Li	Fe	Na	Ni	Sc	Ti
vdW radii (Å)	1.82	2.00	2.27	1.63	2.00	2.00
Covalent radii (Å)	1.28	1.52	1.66	1.24	1.70	1.60
M-M length in bulk (Å)	3.04	2.48	3.71	2.50	3.25	2.89

Table 3 Hirshfeld charge analysis of edge atoms in Cu<ZGNR>Cu and H-ZGNR>Cu systems. C_{-Cu} and C_{-H} represent the edge carbon atom connecting to Cu and H, respectively.

	Cu<ZGNR>Cu		H-ZGNR>Cu			
	Cu	C _{-Cu}	Cu	C _{-Cu}	H	C _{-H}
Charge (<i>e</i>)	0.148	-0.116	0.149	-0.115	0.046	-0.039
Spin (absolute value)	0.022	0.200	0.021	0.193	0.012	0.202

Table 4. Lowest vibrational frequencies (cm⁻¹) of molecular anions **1-3** calculated based on three DFT functionals.

	Lowest vibrational frequency		
	B3LYP	TPSS	PBE
1	62.17	64.32	62.63
2	54.55	58.26	56.29
3	35.33	38.32	36.54

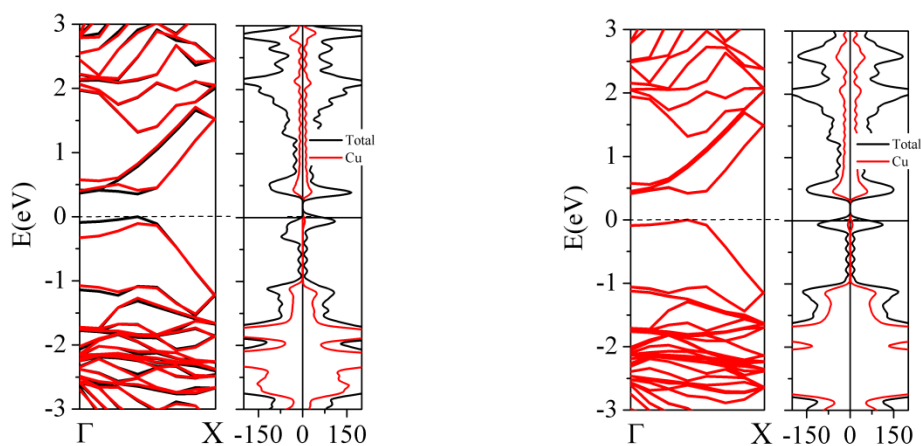


Figure 13. Calculated electronic band structure and density of states (DOS) of the (a) H<8-ZGNR>Cu and (b) Cu<8-ZGNR>Cu systems. In the band-structure graphs, black and red denote spin-up and spin-down channel, and in DOS graphs positive and negative denote spin-up and spin-down channel, respectively.

The perfectly planar structure of ptC strips at the edge of Cu<ZGNR>Cu system stems from both steric and electronic stabilization. As shown in Table 2, the sum of van der Waals radii (2.80 Å) and covalent radii (2.64 Å) of two Cu atoms, as well as the Cu-Cu bond length (2.55 Å) in the bulk all match the neighboring C-C distance (2.48 Å) very well along the edge direction. Hence little mechanical strain is incurred upon the edge decoration of ZGNR by Cu atoms. In addition, the electronic stabilization may be imparted by both aromatic delocalization and the σ -donation from the electropositive groups[35a]. The $2p_z$ orbital of the edge ptC is significantly delocalized in the ZGNR due to in-planar π -electrons. Furthermore, significant charge transfer from Cu to ptC is found. Based on the Hirshfeld charge analysis, the ptC atom carries -0.11 |e| negative charge and the Cu atom has a positive charge (0.15 |e|) (cf. Table 3). In contrast, the interior C atoms of ZGNR are nearly charge neutral. Figure 13a shows the deformation electronic density[39] of the Cu<8-ZGNR>Cu system. One can see that the edge ptC atoms form multicenter electron-deficient covalent bonds (blue regions in Figure 13a) with Cu atoms. The highest occupied electronic state (HOES) and the lowest unoccupied electronic state (LUES) at the gamma (Γ) point are displayed in Figure 13b and 13c, respectively. The HOES is mainly contributed by the $2p_z$ atomic orbitals of ptC atoms. The LUES clearly shows multi-center bonding between ptC and Cu atoms, as well as a highly delocalized σ -orbital among peripheral Cu-Cu atoms. The electronic band structure and density of states of Cu<8-ZGNR>Cu system are

shown in Figure S5, which suggest that Cu<8-ZGNR>Cu is a spin-non-polarized semiconductor with a band gap ~ 0.42 eV. The Hirshfeld spin analysis reveals significant spin distribution to the edge ptC atoms (cf. Table 3). The two ptC strips are antiferromagnetically coupled with each other, even though the edge Cu atoms do not exhibit significant magnetism.

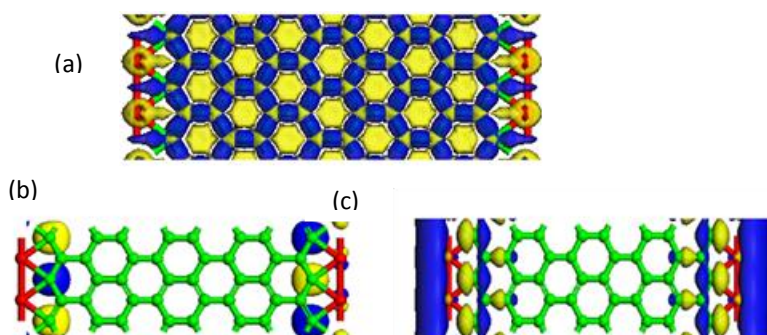


Figure 13. Iso-surface ($0.05 e/a.u.$) of the deformation electronic density of Cu<8-ZGNR>Cu. Blue and yellow color represent electron rich and deficient region, respectively. (b) The highest occupied electronic state and (c) lowest unoccupied electronic state of the Cu<ZGNR>Cu at Γ point.

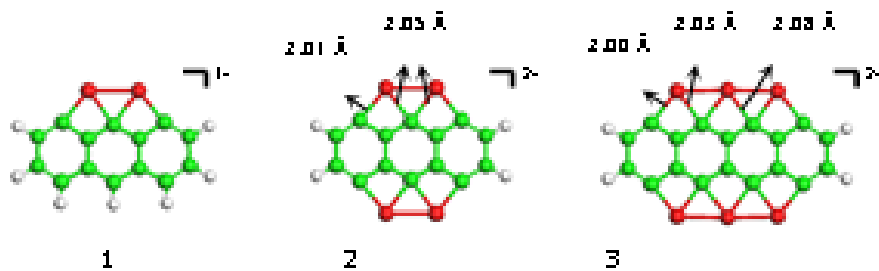


Figure 14. Structures and WBI (in parentheses) of molecular anions **1** – **3**, where green, red and white balls denote C, Cu, and H atoms, respectively.

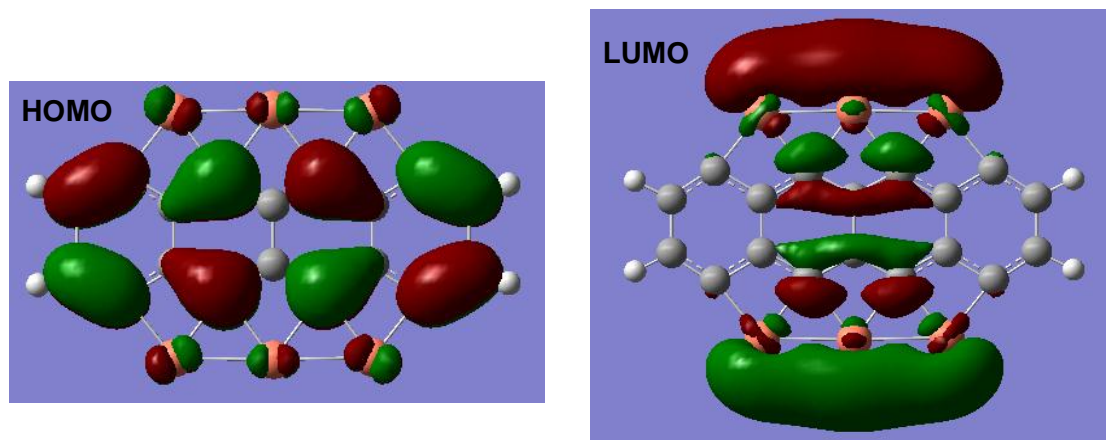


Figure 15. HOMO and LUMO of molecular dianion **3**.

To gain more insights into the bonding nature of ptC in Cu<ZGNR>Cu, we investigated three model molecular systems **1** – **3** (see Fig. 15), for which we used DFT functionals including hybrid (B3LYP), meta-GGA (TPSS), and PBE, along with the 6-311++(2df,2dp) basis set implemented in the Gaussian 03 package [40]. The anions **1** - **3** are all stable local minima (lowest frequencies are listed in Table 4) and exhibit perfect planarity. In the dianion **3**, both sides of the molecule exhibit ptC centers. The Wiberg bond index (WBI) analysis and natural population analysis (NPA) were taken for **1** – **3** based on natural bonding orbital (NBO) calculation. As shown in Fig. 14, the Cu-C bonds are weakened with the increase of the number of ptC centers from **2** to **3**, reflecting by smaller WBIs of Cu-C bonds in **3**. However, the total WBI for the ptC maintains at ~ 4.0 in **1** – **3**. The NPA analysis suggests that Cu atoms are positively charged while ptC is negatively charged, consistent with the Hishfeld analysis for the periodic Cu<ZGNR>Cu system. In addition, main features of HOMO and LUMO of **3** are consistent with HOES and LUES of periodic system (cf Fig. 15 for HOMO and LUMO of **3**). The natural

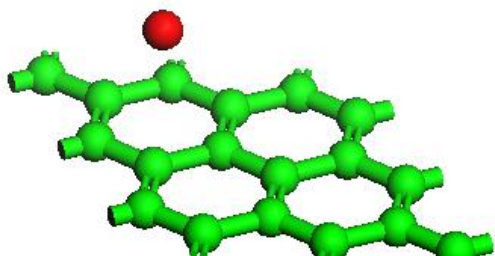
electron configuration for the ptC centers in **3** is $2s^{0.98}2p_x^{1.0}2p_y^{1.0}2p_z^{1.2}$, suggesting the stability of ptC stems mainly from the delocalization of $2p_z$ electrons of ptC atoms, rather than from the σ -donation[36b] from Cu atoms. However, we note that the highly delocalized Cu-Cu bonding in LUMO s enhances the stability of planar structure.

In summary, we predicted highly stable Cu-decorated 1-D ZGNRs which contain ptC strip(s). The stability of multicenter ptC strip stems from both highly delocalized π orbital of ZGNR and nearly-perfect fit of Cu-Cu bonding geometries at the edge.

2.5 Hydrogen Storage in Metal-decorated GNRs.

Safe and cost-effective hydrogen storage media are required for wide application of hydrogen fuel-cell powered systems[41,42]. A gravimetric target of 9 wt% of H_2 for the hydrogen storage media has been set by the U.S. Department of Energy (DOE). To meet this target, it has been suggested theoretically that the optimal adsorption enthalpy of H_2 should be about 15.1 kJ/mol at 298 K and pressure 1.5~30 bar, and about 13.6 kJ at a relatively high pressure (e.g. 130 bar)[43]. Other theoretical estimates suggest that desirable adsorption energy of H_2 can range from 0.2 - 0.6 eV per H_2 molecule [45a]. To date, the DOE gravimetric target has not been achieved experimentally. On theoretical side, a number of material designs have been proposed to reach the DOE target. For example, it has been suggested that alkali or alkali earth metal (Li, Na, K, Ca)-decorated nanostructured materials may lead to an adsorption energy of 0.1 - 0.2 eV per H_2 [44-51]. Moreover, transition metal (Sc, Ti and V)-decorated nanostructured materials can yield higher adsorption energy [52-59] due to the Kubas interaction[60] which results from the hybridization of H_2 σ or σ^* orbitals with transition metal d orbitals[61,63]. In the alkali metal

decorated systems, high concentrations of B dopants or defects are required, while in the transition metal decorated systems, transition metal atoms tend to form clusters rather than spread over the adsorbent, thereby reducing hydrogen storage capacity. Carbon nanostructures, such as fullerenes, carbon nanotubes, graphene, GNRs and related nanostructures have been explored as adsorbent for metal adsorption owing to their large surface area per unit weight [50-52,56,57,63,64]. Nevertheless, as shown in Table 5, the binding energy of most metal with the carbon substrates is typically $\sim 1\text{eV}/\text{atom}$, much less than the cohesive energy per atom in bulk metals. Hence, most metals tend to form clusters when coated on the carbon substrates. We show that edge-modified GNR by Sc can be a viable hydrogen storage media as each Sc site at the edge can adsorb 4-5 hydrogen molecules in a quasi-molecular fashion, thereby can theoretically meet the DOE gravimetric target with the narrowest GNR. In addition, the adsorption energy of H_2 can be modestly tuned (either increased and decreased) via an external electric field whose magnitude is typically an order of magnitude less than that required for other carbon-metal systems to achieve comparable weight percentage of hydrogen adsorption.



	Li	Na	Mg	Al	Sc	Ti	V	Cr	Mn	Fe	Co	Ni	Cu
$E_b(\text{eV})$	0.97	0.82	0.17	1.00	2.45	1.32	1.40	0.27	0.29	0.52	0.57	0.88	0.22

Table 5. Calculated binding energy of a metal atom (red sphere) located on the center of a hexagon of the graphene. Optimization of the structure is at the GGA/PBE level of theory.

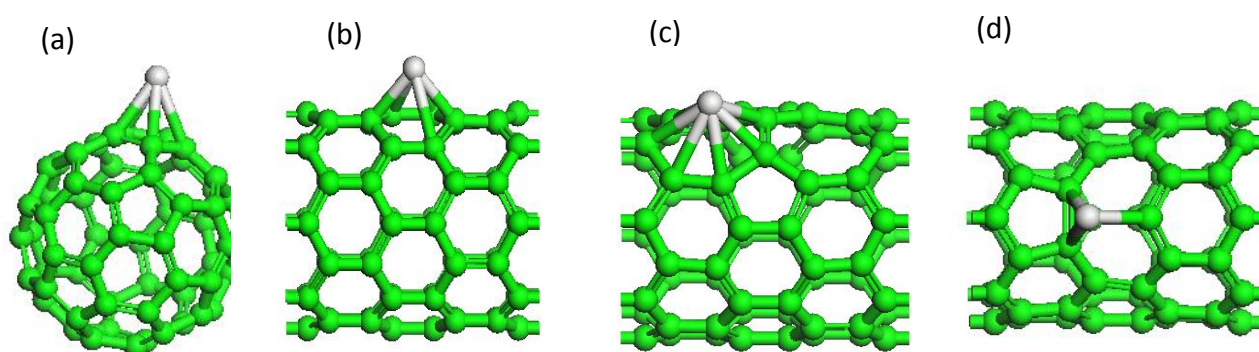


Figure 16. Optimized structure of a Sc atom (grey sphere) binding with (a) a fullerene C_{60} , (b) a perfect (8,0) single-walled carbon nanotube (SWCNT), a (8,0) SWCNT containing (c) a Stone-Wales defect (per supercell), or (d) a vacancy. Calculated binding energies between Sc and the carbon substrate are: (a) 1.9 eV (1.85 eV reported in Ref. 14), (b) 2.2 eV, (c) 2.6 eV, and (d) 4.7 eV, respectively.

First, we modified only one edge of an 8-ZGNR by the lightest transition metal Sc. If a modest level of edge decoration is realized on one edge such that every two carbon atoms on the edge are bonded with one Sc atom [such a model system is named as $ZGNR>Sc/2$], the calculated binding energy of each Sc atom is 6.4 eV. Here, the binding energy of Sc at the 8-

ZGNR edge is calculated according to the formula $E_b = [E(8\text{-ZGNR with one bare edge}) + E(\text{Sc}) - E(\text{ZGNR} > \text{Sc}/2)]/n(\text{Sc})$. Notably, this Sc binding energy is greater than that (5.1 eV) of a fully Sc-decorated ZGNR (where every carbon atom on the edge is bonded with an Sc atom). More importantly, both Sc binding energies are greater than the cohesive energy (4.4 eV) of bulk Sc, suggesting that Sc will not form clusters once bonded with carbon atoms at the 8-ZGNR edge. In other words, edge-decorated GNR by Sc is energetically robust. Do Sc atoms also prefer to bind with carbon atoms on the surface of GNR? Our calculation indicates that if Sc atoms are uniformly dispersed on the surface of graphene, with each Sc atom located at the center of a carbon hexagon, the Sc binding energy is merely 2.1 eV per Sc atom. Because this binding energy is much less than the cohesive energy of bulk Sc, it is more likely that Sc atoms will form clusters on the surface of GNR rather than disperse uniformly.

In addition, we have examined binding energies of Sc atom with other low-dimensional carbon nanostructure, *e.g.* fullerene C_{60} and (8,0) single-walled carbon nanotube (SWCNT). Consistent with previous results [54,55], our calculations show that the binding energies between Sc and C_{60} and between Sc and (8,0) SWCNT are less than 2.5 eV (Fig. 16), considerably less than the cohesive energy of bulk Sc. We have also examined binding energies of Sc atom with a Stone-Wales and a vacancy defect on the (8,0) SWCNT (Fig. 16). A Stone-Wales defect gives rise to a binding energy of 2.6 eV, while a vacancy gives a binding energy of 4.7 eV, greater than the cohesive energy of bulk Sc. However, since a SWCNT cannot entail very high concentration of vacancies, it is unlikely to achieve a high coverage of Sc on the outer surface of SWCNT.

Table 6. Binding energy E_b of a metal atom with two carbon atoms at the edge of GNR, bulk cohesive energy of metal E_c , and adsorption energy E_H of H_2 at the M-decorated edge of 8-ZGNR>M/2 (M=Sc, Ti, V, Cr, Mn, Fe, Co, Ni, Co, Cu)

	Sc	Ti	V	Cr	Mn	Fe	Co	Ni	Cu
E_b (eV)	6.4	6.2	6.0	4.9	4.9	4.9	4.9	5.2	3.9
E_c (eV)	4.4	5.1	5.4	4.0	3.8	4.4	4.3	4.4	3.4
E_H (eV)	0.24	0.43	0.42	0.22	0.20	0.27	0.57	0.39	0.41

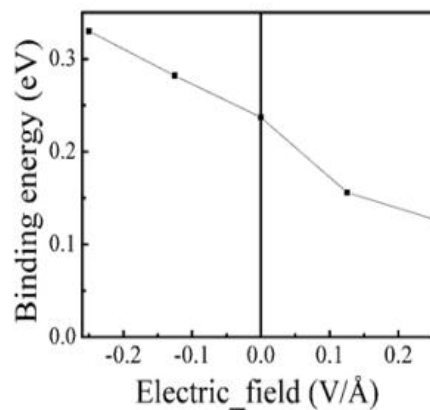
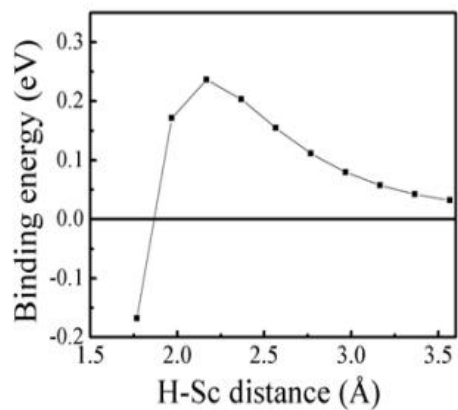
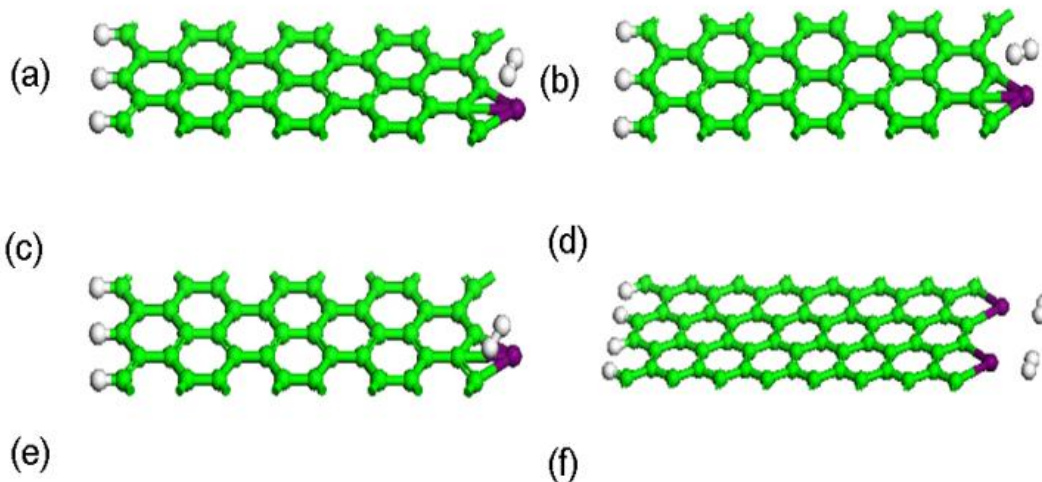


Figure 17. (a)-(c) Optimized structures of 8-ZGNR>Sc/2 with one H₂ per supercell. An in-plane electric field is applied perpendicular to the axial direction, with magnitude being (a) zero, (b) -0.25 V/Å and (c) 0.25 V/Å to the right. (d) Optimized structure of AGNR>Sc with one H₂ per supercell. (e) Calculated adsorption energies per H₂ for 8-ZGNR>Sc/2 model as a function of the Sc-H distance. (f) Calculated adsorption energy per H₂ for 8-ZGNR>Sc/2 as a function of external electric field. Green, purple and white balls represent C, Sc, and H atoms, respectively.

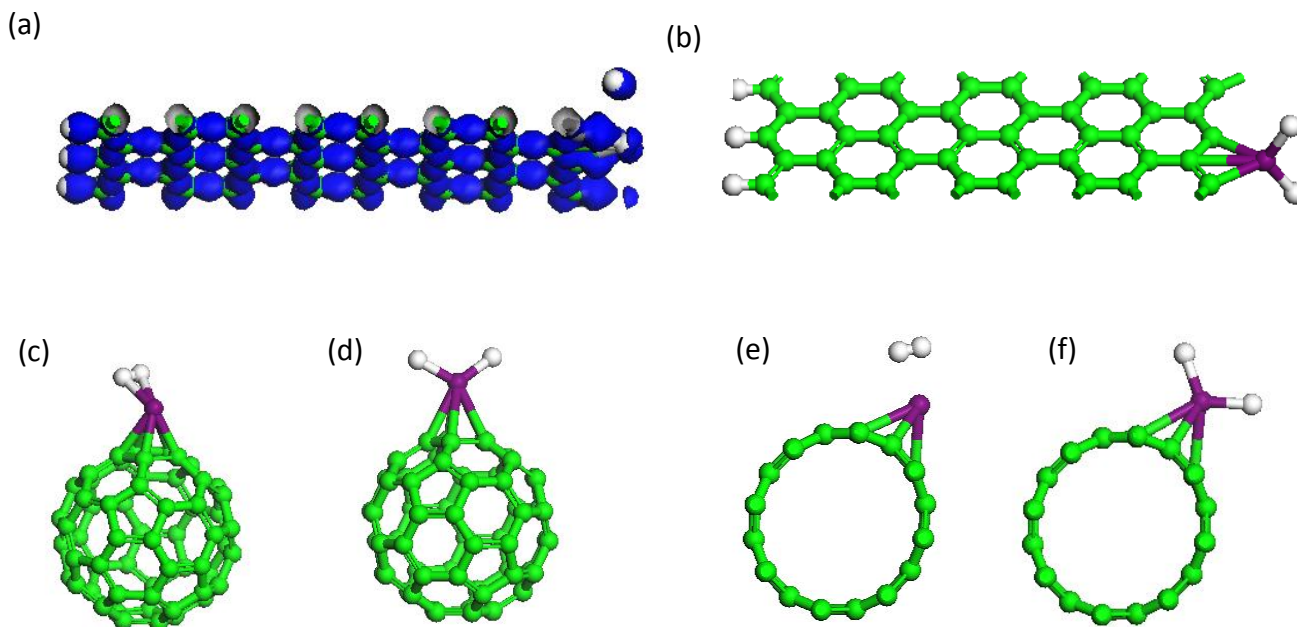


Figure 18. (a) Calculated deformation density distribution for the 8-ZGNR>Sc/2 model system with one H₂ (per supercell) adsorbed at the Sc-decorated edge. Optimized structure of (b) the 8-ZGNR>Sc/2 model where the Sc atom binds with two H atoms (dihydride configuration); (c) a H₂ molecule, and (d) two H atoms adsorbed on a Sc atom, respectively, where the Sc atom is adsorbed on a fullerene C₆₀; (e) a H₂ molecule, and (f) two H atoms adsorbed on a Sc atom, respectively, where the Sc atom is adsorbed on a perfect (8,0) SWNCT. Here the configuration (d) is **0.65 eV** lower than the configuration (c) in energy, and the configuration (f) is **0.50 eV** lower than the configuration (e).

The (Hirshfeld) charge on Sc and on H atom, distance between H-H, and the binding energy of Sc-2H complex to the carbon substrate E_b for configurations (a)-(f) are given in the table below.

	a	b	c	d	e	f
Charge on Sc (<i>e</i>)	0.51	0.51	0.59	0.59	0.50	0.51
Charge on H (<i>e</i>)	0.01	-0.21	0.00	-0.22	0.00	-0.22
H-H distance (Å)	0.79	3.19	0.82	3.06	0.80	3.10
E_b (eV)	6.20	4.75 [#]	1.96	1.70 [#]	2.27	1.88 [#]

[#]When the H₂ molecule dissociates into two H atoms, the E_b value becomes smaller, in part due to a net charge transfer (highlighted in bold) from the carbon substrate to the H atoms through Sc.

Besides Sc, we also calculate E_b of 8-ZGNR>M/2 for other first-row transition metals in the periodic table (M=Ti, V, Cr, Mn, Fe, Co, Ni, Cu) and bulk energy E_b of the metals, as shown in Table 6. One can see that all E_b values are greater than bulk cohesive energies of corresponding metals. Hence, all first-row transition metals prefer to bind with carbon atoms at the edge of GNR. However, Sc yields the largest energy difference ($E_b - E_c$) while other metals give much smaller energy differences ($E_b - E_c < 1\text{eV}$).

Next, we compute adsorption energies of hydrogen molecules, using 8-ZGNR>M/2 as a prototype model system. The first hydrogen molecule H₂ adsorbed on a Sc atom at the GNR edge is illustrated in Fig. 17(a). Upon geometric optimization, the distance between the Sc atom and an H atom is about 2.15 Å; the calculated adsorption energy of H₂ is 0.24 eV. Unlike the fullerene-Sc system[54] where the first adsorbed H₂ dissociates into dihydride on Sc, here the H₂ molecule is in quasi-molecular form with the H-H bond length slightly elongated from 0.75 Å to 0.79 Å due to the Kubas interaction[60]. Indeed, the calculated deformation density distribution (Fig. 18) confirms that there is no density between H₂ and Sc atom. Our calculation also shows that the dihydride structure (Fig. 18) is 0.6 eV/supercell higher in energy than the structure shown in Fig. 17(a). In other words, it is energetically unfavorable for H₂ to dissociate. Based on

the Hirshfeld charge analysis, the H_2 molecule carries a small positive charge of $+0.025e$. In Table 5, calculated adsorption energies of H_2 , E_H , for all 8-ZGNR>M/2 systems considered are given. The adsorption energies are mostly in the desirable range (0.15 – 0.25 eV) for hydrogen storage, but these metals possess a heavier atomic mass than Sc. We also compute the adsorption energy of H_2 as a function of H-Sc distance. As shown in Fig. 17(e), the interaction between H_2 and Sc is quite short-ranged. Hence, only a few hydrogen molecules that are within a short distance from a Sc atom can bind with the Sc atom in a quasi-molecular fashion.

In addition, we investigate effects of an in-plane electric field on hydrogen adsorption by 8-ZGNR>Sc/2. The adsorption configuration for H_2 indeed depends on the direction of field, as shown in Fig. 17(b) and (c). When a field of 0.25 V/\AA is applied to the left (from Sc-decorated edge to H-passivated edge), the distance between Sc and an atom of H_2 increases to 2.31 \AA and the adsorption energy of H_2 increases from 0.24 eV to 0.33 eV. If a field of 0.25 V/\AA is applied to the right, the distance between Sc and H_2 decreases to 1.96 \AA and the adsorption energy decreases to 0.13 eV. The adsorption energy per H_2 as a function of electric field strength is plotted in Fig. 17(f). Note that the strong field effect on hydrogen adsorption has been demonstrated previously for boron-nitride (BN) monolayer system[68]. Zhou *et al.* reported that a very high electric field (2.25 V/\AA) is required to enhance the adsorption energy of H_2 from 0.03 to 0.14 eV. For Sc-decorated GNR, however, the required electric field is an order of magnitude smaller to achieve 0.11 eV increase in the adsorption energy of H_2 . Moreover, the adsorption energy of H_2 can be either increased or decreased, depending on the direction of the in-plane electric field. So, the physical origin for this field dependence is different from that for the BN sheet. Here, the distances between Sc and two H atoms of H_2 are nearly the same. As such, the dipole moment of H_2 should not play a major role under the electric field. Based on Hirshfeld

charge analysis, we find that the charge on Sc is 0.50, 0.80 and 0.22 e, respectively, under the electric field of zero, -0.25, and 0.25 V/Å. Hence, the field-induced charge on Sc likely plays the most important role in the field-dependence of the hydrogen adsorption energy.

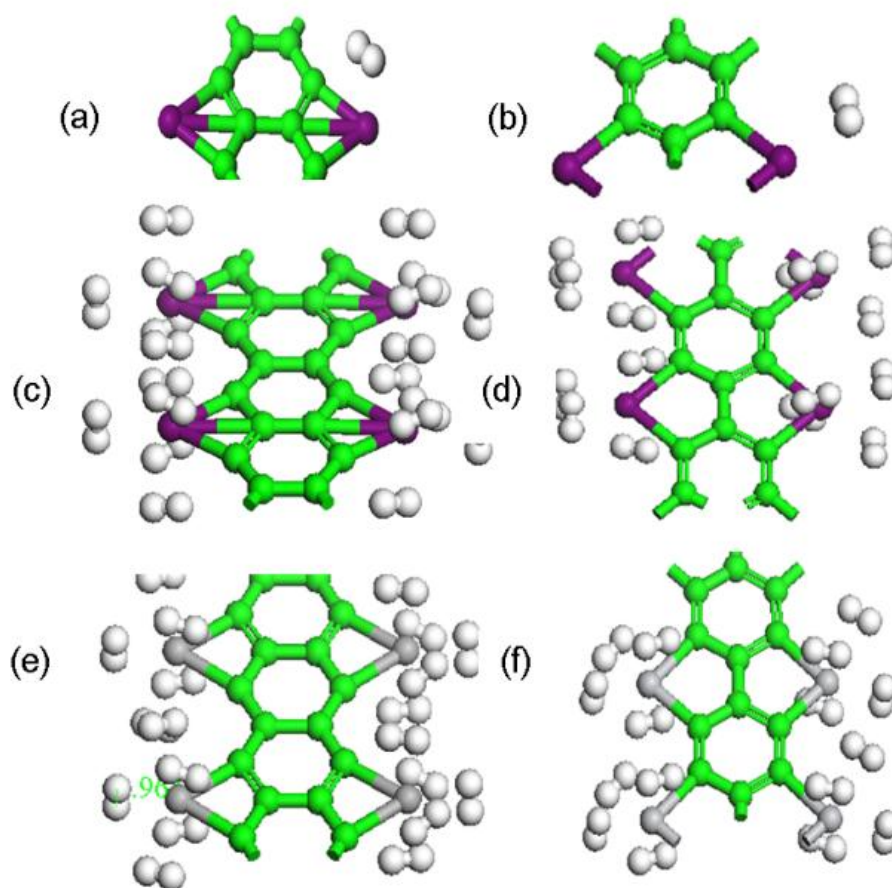


Figure 19. Optimized structures of (a) Sc/2<2-ZGNR>Sc/2 and (b) Sc<AGNR>Sc with one H₂ per supercell; optimized structures of (c) Sc/2<2-ZGNR>Sc/2, (d) Sc<AGNR>Sc, (e) Ti/2<2-ZGNR>Ti/2 and (f) Ti<AGNR>Ti with multiple H₂ per supercell. Green, purple, grey and white balls represent C, Sc, Ti and H atoms.

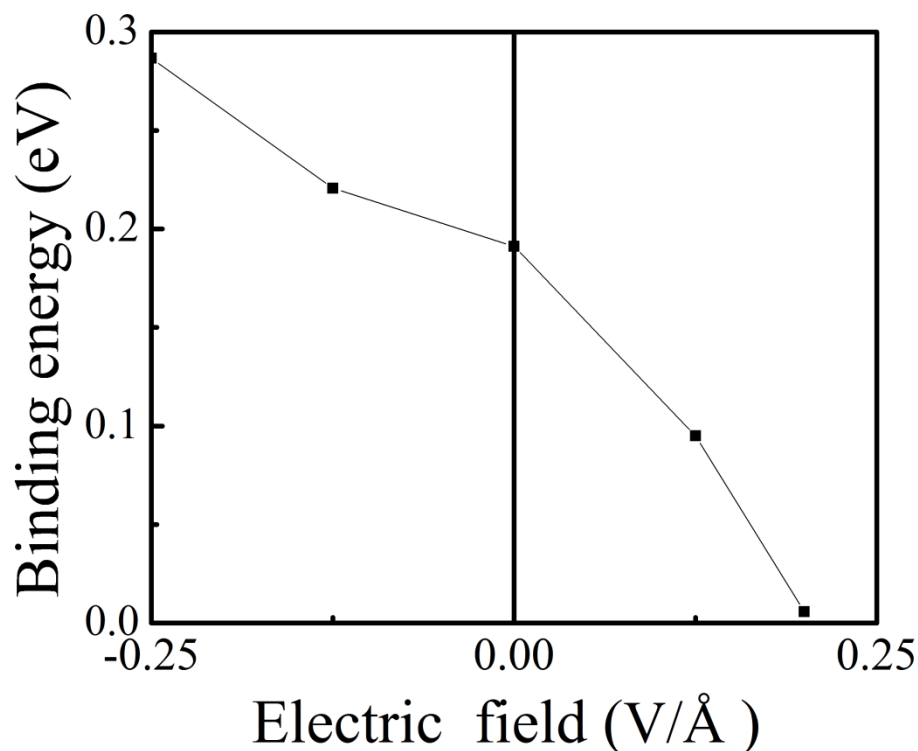


Figure 20. Calculated adsorption energy per H_2 for the $Sc/2\langle 2-ZGNR \rangle Sc/2$ model system as a function of the strength of an in-plane electric field.

We also consider Sc-decorated armchair GNR (AGNR) at one edge, where every Sc atom is bonded with two carbon atoms. This model system is denoted as $AGNR \rangle Sc$ (see Fig. 17(d)). The binding energy of Sc to the AGNR edge is 5.0 eV, larger than the cohesive energy of bulk Sc but less than that for $8-ZGNR \rangle Sc/2$. Upon adsorption of one H_2 molecule on one Sc atom, the calculated adsorption energy of H_2 is 0.14 eV. Upon applying an in-plane electric field of 0.25 $V/\text{\AA}$ to the right, the calculated Hirshfeld charge on Sc decreases from 0.39 to 0.33e, and the

adsorption energy of H_2 is reduced to 0.051 eV. On the other hand, upon applying the field of 0.25 V/\AA to the left, the charge on Sc increases to 0.51e and the adsorption energy of H_2 is enhanced to 0.16 eV. Compared to 8-ZGNR>Sc/2, the hydrogen adsorption energy is less sensitive to the charge of charge on Sc. Hence, the adsorption energy of H_2 shows weaker field dependence.

To achieve high H_2 adsorption capacity, the system should have high ratio of number of adsorption sites to the weight of adsorbate material, besides quasi-molecular H_2 binding capability for the adsorption sites. To achieve highest ratio, we consider a narrowest GNR system, namely, Sc/2<2-ZGNR>Sc/2, where both edges are decorated by Sc (Fig. 19(a)). First, we study adsorption of a single H_2 molecule on each Sc atom. As shown in Fig. 19(a), upon geometric optimization, the distances between Sc and two H atoms are about 2.1 Å. The calculated adsorption energy of H_2 is 0.19 eV. Upon applying an electric field of 0.20 V/\AA to the right, the charge on Sc is reduced from 0.49 to 0.22 e, and the adsorption energy of H_2 decreases to 0.006 eV. On the other hand, upon applying an electric field of 0.25 V/\AA to the left, the charge on Sc increases to 0.73 e, and the adsorption energy of H_2 is enhanced to 0.29 eV. The adsorption energy per H_2 as a function of electric field is plotted in Fig. 20. For this system, the adsorption energy of H_2 is also sensitive to the direction and magnitude of the applied electric field. Upon adsorption of a hydrogen molecule (per supercell) to the narrowest Sc<AGNR>Sc system, as shown in Fig. 19(b), the distances between Sc and two H atom are about 2.15 Å, and the calculated adsorption energy of H_2 is 0.11 eV. If an in-plane electric field of 0.25 V/\AA is applied to the right, the charge on Sc is reduced from 0.36 to 0.21 e, and the adsorption energy of H_2 decreases to 0.06 eV. If the field of 0.20 V/\AA is applied to the left, the charge on Sc increases to 0.50 e, and the adsorption energy is enhanced to 0.15 eV.

Table 7. Average adsorption energy of H₂ E_a (based on GGA/PBE level of theory), and E_a calculated based on the local density approximation (LDA) method, charge on Sc atom (GGA/PBE), bond length of H-H, and the H-Sc distance as increasing number of H₂ adsorbed on the Sc atom, for model system (a) Sc/2<2-ZGNR>Sc/2, and (b) Sc<Narrowest AGNR>Sc.

(a)

numbers of H ₂	E _a (eV) GGA	E _a (eV) LDA	Charge on Sc (e)	Bond length of H-H (Å)	H-Sc distance (Å)
1	0.19	0.53	0.43	0.80	2.15
2	0.16	0.51	0.41	0.79,0.79	2.12,2.19
3	0.23	0.54	0.38	0.81,0.81,0.82	2.13,2.13,2.05
4	0.21	0.53	0.33	0.78,0.80,0.80,0.81	2.38,2.13,2.13,2.05
5	0.17	0.49	0.32	0.79,0.79,0.80, 0.80,0.81	2.14,2.14,2.14,2.10,2.10

(b)

numbers of H ₂	E _a (eV) GGA	E _a (eV) LDA	Charge on Sc (e)	Bond length of H-H (Å)	H-Sc distance (Å)
1	0.11	0.30	0.45	0.83	2.15
2	0.24	0.48	0.49	0.81,0.81	2.11,2.16
3	0.23	0.53	0.41	0.81,0.81,0.81	2.15,2.23,2.23
4	0.23	0.54	0.35	0.78,0.81,0.81,0.81	2.11,2.17,2.17,2.17

For the Sc/2<2-ZGNR>Sc/2 system, we find that the maximum number of hydrogen molecules that can be adsorbed on each Sc atom is five (Fig. 19(c)), for which the average adsorption energy of H₂ is 0.17 eV. Under this condition, the highest hydrogen storage gravimetric capacity for this system is 9.7wt%. For the narrowest AGNR, however, the maximum number of hydrogen molecules that can be adsorbed on each Sc atom is 4 (Fig. 19(d)), and the average adsorption energy of H₂ is 0.23 eV. Here, the distance between two nearest Sc

atoms is 4.26 Å, smaller than 4.92 Å for the Sc/2<2-ZGNR>Sc/2 system. Hence, for the narrowest Sc<AGNR>Sc system, the highest hydrogen storage gravimetric capacity is 9.1 wt%. Besides gravimetric density, the DOE target of volumetric density (>0.081kg/L) should also be met. Ideally, if those Sc-decorated GNRs are stacked layer by layer and side by side, so the distance between nearest graphene plane is 4.0Å and the distance between two Sc atoms of two nearest GNRs in same plane is 6.0Å, the volumetric density of hydrogen in Sc/2<2-ZGNR>Sc/2 and Sc<AGNR> are respectively 0.102kg/L and 0.100kg/L, greater than target (0.081kg/L). In Table.7 we list the average adsorption energy versus the numbers of H₂ adsorbed on one Sc atom in Sc/2<2-ZGNR>Sc/2 or Sc<AGNR>Sc system. For Sc<ZGNR>Sc and Sc<AGNR>Sc of different width, their hydrogen storage gravimetric capacity are listed in Table 8. If the Sc atoms are replaced by Ti in both Sc/2<2-ZGNR>Sc/2 (Fig. 19(e)) and Sc<AGNR>Sc systems (Fig. 19(f)), we find that the maximum number of H₂ molecules adsorbed on each Ti atom is still 5 and 4, respectively. However, since Ti atom is heavier than Sc, their hydrogen storage gravimetric capacity is less.

Table 8. An estimate of weight percentage of hydrogen for Sc-decorated AGNRs and *n*-ZGNRs with different widths, assuming each Sc can adsorb four H₂ molecules for AGNR systems, and five H₂ molecules for *n*-ZGNR systems.

	Narrowest AGNR	2 nd Narrowest AGNR	3 rd Narrowest AGNR	2-ZGNR	3-ZGNR	4-ZGNR
Weight percentage	9.1	8.0	7.1	9.7	7.9	6.6

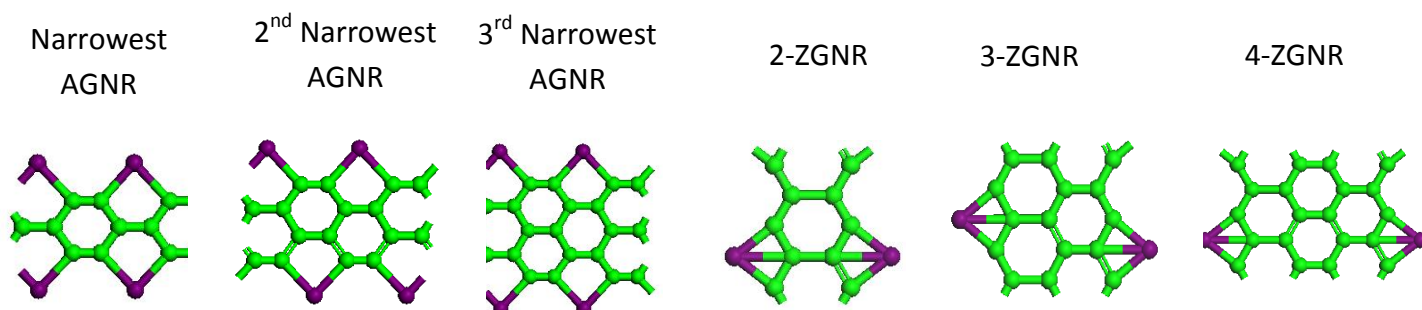


Table 9. Calculated adsorption energy of a single H₂ molecule on a metal atom per supercell for the 8-ZGNR>Sc/2 (Fig. 1(a)), AGNR>Sc (Fig. 1(e)), Sc/2<2-ZGNR>Sc/2 (Fig. 2(a)) and Sc<AGNR>Sc (Fig. 2(c)) systems, based on three DFT methods.

DFT	8-ZGNR>Sc/2	AGNR>Sc	Sc/2<ZGNR>Sc/2	Sc<AGNR>Sc
PBE	0.24	0.14	0.19	0.09
PBE-D2	0.27	0.14	0.20	0.09
LDA-D2	0.60	0.34	0.53	0.30

We also compute adsorption energy of H₂ using three different DFT methods: (1) PBE-GGA, (2) PBE-D2 method of Grimme[69], and (3) local density approximation (LDA)-D2 method[69], implemented in Vienn Ab initio Simulation package (VASP 5.2)[70]. As shown in Table 9, the calculated adsorption energies using the PBE-D2 method are nearly the same as those using PBE-GGA, but about half of those calculated based on the LDA-D2 method. The actual adsorption energies are likely in between the values from PBE-D2 and LDA-D2 methods[71]. If this is the case, as shown in Table 7, the average H₂ binding energies would be between 0.17 eV

(PBE) and 0.49 eV (LDA) for the Sc/2<2-ZGNR>Sc/2 system, and between 0.23 eV (PBE) and 0.54 eV (LDA) for the Sc/2<AGNR>Sc/2 system. All these binding energies are within the optimal adsorption energy range for hydrogen storage.

In summary, on basis of density-functional theory calculations, we show that edge-modified GNRs by Sc can adsorb multiple hydrogen molecules in a quasi-molecular fashion, thereby can be a potential candidate for hydrogen storage. Moreover, the adsorption energy of H₂ can be adjusted (either increased and decreased) via an in-plane electric field. For the narrowest GNR with either Sc-decorated armchair or zigzag edges, the average binding energy of H₂ is 0.23 or 0.17 eV, suitable for hydrogen storage. The predicted weight percentage of H₂ is > 9wt% for both systems, meeting the DOE target. In light of that controlled synthesis of narrow GNRs has been recently reported[72-73], we expect that edge-decorated GNR by Sc can be realized in the laboratory as well.

2.6 References

1. Novoselov, K. S.; Geim, A. K.; Morozov, S. V.; Jiang, D.; Katsnelson, I.V.; Grigorieva, I. V.; Dubonos, S. V.; Firsov, A. A. *Nature* **2005**, 438,197.
2. Katsnelson, M. L; Novoselov, K. S.; Geim, A. K. *Nat. Phys.* **2006**, 2, 620.
3. Castro Neto, A. H.; Guinea, F.; Peres, N. M. R. *Phys. World* **2006**, 19, 33.
4. Zhou, S. Y.; Gwonen, G. H.; Graf, J.; Ferdorov, A. V.; Spataru, C.D.; Diehl, R. D.; Kopelevich, Y.; Lee, D. H.; Louie, S. G.; Lanzara, A. *Nat Phys.* **2006**, 2, 595-599.
5. Geim, A. K.; Novoselov, K. S. *Nat. Mater.* **2007**, 6 (3), 183-191.

6. Novoselov, K. S.; Jiang, Z.; Zhang, Y.; Morozov, S. V.; Stormer, H. L.; Zeitler, U.; Maan, J. C.; Boebinger, G. S.; Kim, P.; Geim, A. K. *Science* **2007**, *315*, 1379.
7. Zheng, Y.; Ando, T. *Phys. Rev. B* **2002**, *65*, 245420.
8. Novoselov, K. S.; Geim, A. K.; Morozov, S. V.; Jiang, D.; Zhang, Y.; Dubonos, S. V.; Firsov, A. A. *Science* **2004**, *306* (5696), 666-669.
9. Fujita, M.; Wakabayashi, K.; Nakada, K.; Kusakabe, K. *J. Phys.Soc. Jpn.* **1996**, *65*, 1920–1923.
10. Miyamoto, Y.; Nakada, K.; Fujita, M. *Phys. Rev. B* **1999**, *60*, 16211.
11. Nakada, K.; Fujita, M.; Dresselhaus, G.; Dresselhaus, M. S. *Phys. Rev. B* **1996**, *54*, 17954–17961.
12. Kusakabe, K.; Maruyama, M. *Phys. Rev. B* **2003**, *67*, 092406.
13. Lee, H.; Son, Y. W.; Park, N.; Han, S.; Yu, J. *Phys. Rev. B* **2005**, *72*, 174431.
14. Rudberg, E.; Salek, P.; Luo, Y. *Nano Lett.* **2007**, *7*, 2211–2213.
15. Pisani, L.; Chan, J. A.; Montanari, B.; Harrison, N. M. *Phys. Rev. B* **2007**, *75*, 064418.
16. Hod, O.; Barone, V.; Scuseria, G. E. *Phys. Rev. B* **2008**, *77*, No. 035411.
17. Hod, O.; Peralta, J. E.; Scuseria, G. E. *Phys. Rev. B* **2007**, *76*, No. 233401.
18. Hod, O.; Barone, V.; Peralta, J. E.; Scuseria, G. E. *Nano Lett.* **2007**, *7*, 2295–2299.
19. Barone, V.; Hod, O.; Scuseria, G. E. *Nano Lett.* **2006**, *6*, 2748–2754.

20. Son, Y.-W.; Cohen, M. L.; Louie, S. G. *Phys. Rev. Lett.* **2006**, 97, No.216803.
21. Groot, R. A.; Mueller, F. M.; Engen, P. G.; Buschow, K. H. J. *Phys. Rev. Lett.* **1983**, 50, 2024.
22. Prinz, G. A. *Science* **1998**, 282, 1660.
23. Ziese, M. *Rep. Prog. Phys.* **2002**, 65, 143.
24. Son, Y.-W.; Cohen, M. L.; Louie, S. G. *Nature* **2006**, 444, 347–349.
25. Kan, E. J.; Li, Z.; Yang, J. L.; Hou, J. G. *Appl. Phys. Lett.* **2007**, 91, 243116.
26. Kan, E. J.; Li, Z.; Yang, J. L.; Hou, J. G. *J. Am. Chem. Soc.* **2008**, 130, 4224.
27. Delley, B. *J. Chem. Phys.* **1990**, 92, 508-517.
28. Delley, B. *J. Chem. Phys.* **2003**, 113, 7756-7764.
29. Dmol3 is a density functional theory quantum mechanical package available from Accelrys Software Inc.
30. Perdew, J. P.; Burke, K.; Ernzerhof, M. *Phys. Rev. Lett.* **1996**, 77, 3865–3868.
31. Monkhorst, H. J.; Pack, J. D. *Phys. Rev. B* **1976**, 13, 5188-5192.
- 32.(a) Kekulé, Aug. *Annalen der Chemie und Pharmacie* **1857**, 104, 129. (b) van't Hoff, J. H. *Arch. Neerl. Sci. Exactes Nat.* **1874**, 445; (c) Le Bel, J. A. *Bull. Soc. Chim. Fr.* **1874**, 22, 337.
33. Hoffmann, R.; Alder, R. W.; Wilcox, C. F., Jr. *J. Am. Chem. Soc.* **1970**, 92, 4992.

34.(a) Collins, J. B.; Dill, J. D.; Jemmis, E. D.; Apeloig, Y.; Schleyer, P. v. R.; Seeger, R.; Pople, J. A. *J. Am. Chem. Soc.* **1976**, *98*, 5419. (b) Cotton, F. A.; Millar, M. *J. Am. Chem. Soc.* **1977**, *99*, 7886.

35. (a) Schleyer, P. v. R.; Boldyrev, A. I. *J. Chem. Soc., Chem.* **1991**, *113*, 1536. (b) Rasmussen, D. R.; Radom, L. *Angew. Chem.Int. Ed. Engl.* **1999**, *38*, 2876. (c) Boldyrev, A. I.; Simons, J. *J. Am. Chem. Soc.* **1998**, *120*, 7967. (d) Merino, G.; Méndez-Rojas, M. A.; Vela, A. *J. Am. Chem. Soc.* **2003**, *125*, 5026. (e) Wang, Z.; Schleyer, P. v. R. *J. Am. Chem. Soc.* **2001**, *123*, 994. (f) Pei, Y.; Zeng, X. C. *J. Am. Chem. Soc.*, **2008**, *130*, 2580. (g) Wu, Y-B.; Lu, H-G.; Li, S-D.; Wang, Z-X *J. Phys. Chem. A* **2009**, *113*, 3395. (h) Erhardt, S.; Frenking, G.; Chen, Z.; Schleyer, P. v. R. *Angew. Chem. Int. Ed.* **2005**, *44*, 1078. (i) Keese, R. *Chem. Rev.* **2006**, *106*, 4787. (h) Jemmis, E.D.; Subramanian, G.; Kos, A.J.; Schleyer, P. v. R. *J. Am. Chem. Soc.* **1997**, *119*, 9504.(j) Rottger, D.; Erker, G. *Angew. Chem., Int. Ed.* **1997**, *36*, 812. (k) Merino, G.; Mendez-Rojas, M. A.; Vela, A.; Heine, T. *J. Comput. Chem.* **2007**, *28*, 362.

36. (a) Li, X.; Zhang, H-F; Wang, L.S.; Boldyrev, A. I.; Simons, J. *J. Am. Chem. Soc.* **1999**, *121*, 6033. (b) Wang, L.S.; Boldyrev, A. I.; Li, X.; Simons, J. *J. Am. Chem. Soc.* **2000**, *122*, 7681. (c) Li, X.; Zhang, H-F; Wang, L.S.; Geske, G. D.; Boldyrev, A. I. *Angew. Chem., Int. Ed. Engl.* **2000**, *39*, 3630. (d) Siebert, W.; Gunale, A. *Chem. Soc. Rev.* **1999**, *28*, 367.

37. (a) Pancharatna, P.D.; Méndez-Rojas, M. A.; Merino, G.; Vela, A.; Hoffmann, R. *J. Am. Chem. Soc.* **2004**, *126*, 15309. (b) Yang, L-M; Ding, Y-H.; Sun, C-C *J. Am. Chem. Soc.* **2007**, *129*, 658. (c) Geske, G. D.; Boldyrev, A. I. *Inorg. Chem.* **2002**, *41*, 2795. (d) Wu, X.; Pei, Y.; Zeng, X. C. *Nano Lett.* **2009**, *9*, 1577.

38. Martyna, G. J.; Klein, M. L.; Tuckerman, M. E. *J. Chem. Phys.* **1992**, *97*, 2635.

- 39.(a) Perez, N.; Heine, T.; Barthel, R.; Seifert, G.; Vela, A.; Mendez-Rojas, M. A.; Merino, G. *Org. Lett.* **2005**, *7*, 1509; (b) Wu, Y-B.; Jiang, J.-L.; Zhang, R.-W.; Wang, Z-X. *Chem. Eur. J.* **2010** *16*, 1271.
40. Frisch, M. J. et al., 2003, Gaussian 03 (Gaussian, Pittsburgh), Rev. E.02.
41. Schlapbach, L.; Züttel, A. *Nature* 2001, 414, 353.
- 42.(a) Crabtree, G. W.; Dresselhaus, M. S.; Buchanan, M. V. *Phys. Today* 2004, 57, 39 No. 12. (b) Jena, P. J. *Phys. Chem. Lett.* 2011, 2, 206.
43. Bhatia, M.S. K.; Myers, A.L. *Langmuir*. 2006, 22, 1688.
- 44.(a) Yoon, M.; Yang, S.; Wang, E.; Zhang, Z. *Nano Lett.* 2007, 7, 2578. (b) Yoon, M.; Yang, S.; Hicke, C.; Wang, E.; Geohagan, D.; Zhang, Z. *Phys. Rev. Lett.* 2008, 100, 206806.
- 45.(a) Kim, Y.; Zhao, Y.; Williamson, A.; Heben, M.J.; Zhang, S.B. *Phys. Rev. Lett.* 2006, 96, 016102. (b) Deng, W.-Q.; Xu, X.; Goddard, W.A. *Phys. Rev. Lett.* 2004, 92, 166103.
46. Sun, Q.; Jena, P.; Wang, Q.; Marguez, M. J. *Am. Chem. Soc.* 2006, 128, 9741.
47. Chandrakumar, K. R. S.; Ghosh, S. K. *Nano Lett.* 2008, 8, 13.
48. Wu, X.; Yang, J.L.; Zeng, X.C. *J. Chem. Phys.* 2006, 125, 044704
49. Wang, Q.; Sun, Q.; Jena, P.; Kawazoe, Y. *J. Chem. Theory Comput.* 2009, 5, 374–379.
50. Lee, H.; Ihm, J.; Cohen, M.L.; Louie, S.G. *Nano Lett.* 2010, 10, 793.
51. Dimitrakakis, G.K., Tylianakis, E.; Froudakis, G.E, *Nano Lett.* 2008, 8, 3166.
52. Park, N.; Hong, S.; Kim, G.; Jhi, S.-H. *J. Am. Chem. Soc.* 2007, 129, 8999.
53. Lee, H.; Choi, W. I.; Ihm, J. *Phys. Rev. Lett.* 2006, 97, 056104.

54. Zhao, Y.; Kim, Y.-H.; Dillon, A. C.; Heben, M. J.; Zhang, S. B. *Phys. Rev. Lett.* 2005, 94, 155504.
55. Yildirim, T.; Ciraci, S. *Phys. Rev. Lett.* 2005, 94, 175501.
- 56.(a) Durgun, E.; Ciraci, S. Yildirim, T. *Phys. Rev. B.* 2008, 77, 085405. (b) Durgun, E.; Ciraci, S.; Zhou, W.; Yildirim, T. *Phys. Rev. Lett.* 2006, 97, 226102.
57. Zhou, M.; Lu, Y.; Zhang, C.; Feng, Y. P., *Appl. Phys. Lett.* 2010, 97, 103109.
58. Shin, W. H.; Yang, S. H.; Goddard, W. A., III; Kang, J. K. *Appl. Phys. Lett.* 2006, 88, 053111.
59. Meng, S.; Kaxiras, E.; Zhang, Z. *Nano Lett.* 2007, 7, 663.
60. Kubas, G. J. *J. Organomet. Chem.* 2001, 635, 37.
61. Philips, A. B.; Shivaram, B. S. *Phys. Rev. Lett.* 2008, 100, 105505.
62. Hu, X.; Skadtchenko, B. O.; Trudeau, M.; Antonelli, D. M. *J. Am. Chem. Soc.* 2006, 128, 11740.
63. Patchkovskii, S.; Tse, J.S.; Yurchenko, S.N.; Zhechkov, L.; Heine, T.; Seifert, G. *Proc. Natl. Acad. Sci.* 2005, 102, 10439.
64. Du, A.; Zhu, Z.; Smith, S.C. *J. Am. Chem. Soc.* 2010, 132, 2876.
65. Delley, B. J. *Chem. Phys.* 1990, 92, 508. Delley, B. J. *Chem. Phys.* 2000, 113, 7756. Dmol3 4.4 is a density functional theory quantum mechanical package available from Accelrys Software Inc.

66. Perdew, J. P.; Burke, K.; Ernzerhof, M. *Phys. Rev. Lett.* 1996, 77, 3865.
- 67.(a) Wu, M.; Wu, X.; Gao, Y.; Zeng, X.C. *Appl. Phys. Lett.* 2009, 94, 22311; (b) Wu, M. H.; Wu, X.; Zeng, X.C. *J. Phys. Chem C* 2010, 114, 3937; (c) Wu, M. H.; Pei, Y.; Zeng, X.C. *J. Am. Chem Soc* 2010, 132, 5554.
68. Zhou, J.; Wang, Q.; Sun, Q.; Jena, P.; Chen, X. S. *Proc. Natl. Acad. Sci.* 2010, 107, 2801.
69. Grimme, S. *J. Comp. Chem. Soc.* 2006, 27, 1787.
- 70.(a) Kresse, G.; Hafner, J. *Phys. Rev. B* 1993, 47, 558. (b) Kresse, G.; Furthmuller, J. *Phys. Rev. B* 1996, 54, 11169. (c) Kresse, G.; Joubert, D. *Phys. Rev. B* 1999, 59, 1758.
71. Gao, Y.; Zeng, X.C. *J. Phys: Condens. Matter* 2007, 19, 386220.
- 72.(a) Jiao, L.; Zhang, L.; Wang, X.; Diankov, G.; Dai, H. *Nature* 2009, 458, 877. (b) Kosynkin, D. V.; Higginbotham, A. L.; Sinitskii, A.; Lomeda, J. R.; Dimiev, A.; Price, B. K.; Tour, J. M. *Nature* 2009, 458, 872.
73. Cai, J.; Ruffieux, P.; Jaafar, R.; Bieri, M.; Braun, T.; Blankenburg, S.; Muoth, M.; Seitsonen, A. P.; Saleh, M.; Feng, X.; Mullen, K.; Fasel, R. *Nature* 2010, 466, 470.

3 Decorated Graphene of Various Physical Applications.

3.1 Introduction

Although a pristine graphene is a semimetal and chemically inert, recent experiments have shown that a graphene sheet can be chemically converted into a graphane layer (an insulator) through reacting with atomic hydrogen[1-4]. Subsequent theoretical studies suggest that selective hydrogenation of graphene sheets can be employed to adjust graphene's electronic and magnetic properties, where hydrogenated carbon stripes in a graphene sheet serve as the quantum confinement[5,6].

In addition, magnetism in carbon nanostructures is highly desirable for potential applications in storage media and spintronics. Previous theoretical studies have predicted novel magnetism in graphene-based nanostructures, e.g., in zigzag edged graphene nanoribbons and nanoflakes[7-12]. It is also known that the magnetism in these carbon nanostructures stems from the localized states on the edges. Liu and co-workers have demonstrated bulk magnetism in graphene nanohole superlattice with each nanohole acting like a magnetic superatom[13-14]. Although a graphene nanohole with zigzag edges can be produced by carving out a portion of graphene via hot plasmas, still, it is challenging to achieve smooth and defect-free zigzag edges. Moreover, the zigzag edges without chemical termination are relatively unstable, as the planar reconstruction can spontaneously take place at room temperature[15]. On the other hand, if the edges are fully terminated by hydrogen, the magnetic moment at each edge site becomes much smaller than that without termination. Alternatively, magnetism or half metallicity can be achieved in graphene-based

nanostructures via selective hydrogenation. Singh and Yakobson suggested that when zigzag hydrogenated carbon stripes serve as the quantum confinement the edge carbon atoms can exhibit considerable magnetic moments[5]. In other words, a combination of hydrogenation and graphene nanoholes with zigzag edge can be a viable way to generate magnetism. As such, standard lithographic techniques may be less intrusive and applicable to the graphene structure than direct cutting by hot plasmas.

We will show that on a graphene, periodically functionalized strips of carbon chains can be viewed as boundaries that effectively divide the graphene into identical “nanoribbons” thereby leading to spin state similar to the edge state of ZGNRs. Subsequently we present a theoretical design of a new class of chemically modified graphenes via selective hydrogenation of zigzag carbon stripes. The hydrogenated stripes effectively divide a graphene sheet into an array of uncoated triangular carbon domains. First-principles calculation shows that the uncoated carbon triangles can exhibit long-range magnetic order and bulk-like magnetism.

3.2 Computational Details

DFT calculations are carried out using Dmol3 package. The GGA in the PBE form and an all-electron DNP basis set were chosen for the spin-unrestricted DFT computation. The real-space global cutoff radius is set to be 3.7 eV. For -F and -OH modified graphene, a rectangular supercell with dimension $L_1 \times 2.465 \times 16 \text{ \AA}^3$ was adopted, where L_1 is the length of one period of graphene, perpendicular to strips of chemical function groups. For the structure optimization, the Brillouin zone was sampled by $1 \times 20 \times 1$ k points using the Monkhorst-pack scheme. Specifically,

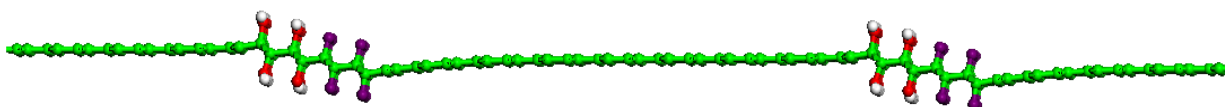
to simulate the hydrogenated graphene, we set up a rhomboid supercell in the graphene plane, with a vacuum layer of 16 Å between the graphene plane and its nearest images in the normal direction. The size of supercell was optimized. The Brillouin zone was sampled by $9 \times 9 \times 1$ k-points using the Monkhorst-pack scheme. For geometric optimization, the forces on every atom were relaxed to be less than 0.0002 au/Å.

3.3 Half-metallicity in periodically functionalized graphene

We present a special design of chemical functionalization on graphene (Fig.1 and Fig. 2(a)) and optimize the unit length, where periodically functionalized carbon strip includes four zig-zag chains - two chains are functionalized with OH groups and another two with F atoms. The non-functionalized part (in a unit cell) has $m = 16$ zig-zag carbon chains. As mentioned above, this chemically modified graphene may be viewed as merging a series of edge modified 20-ZGNRs together. DFT geometric optimization shows that the functionalized graphene exhibits a step-like structure. Nevertheless, the computed electronic band structure indicates that the functionalized graphene is also a half metal, similar to the case of chemically modified 16-ZGNR. Moreover, as shown in Fig. 2(c), the α spin density is mainly localized around the carbon atoms adjacent to the OH groups while the β spin density is mainly localized around the carbon atoms adjacent to the F atoms. This behavior in spin-density distribution resembles that at the two edges of chemically modified ZGNR. Hence, these functionalized carbon chains can be viewed as boundaries to effectively divide the graphene sheet into a series of identical ZGNRs. When the OH groups are replaced by H atoms on the graphene, as expected, the graphene is transformed back to a spin-polarized semiconductor due to the weaker electron-donating capability of H than OH groups.

However, if the width of non-functionalized carbon part (in every unit cell) is increased to $m = 72$, the graphene becomes half metallic again (Fig. 2(d)), similar to the 72-ZGNR case shown in last chapter. This result reinforces our view that as far as the half metallicity is concerned, the chemically functionalized graphene can mimics behavior of edge functionalized ZGNRs.

(a)



(b)

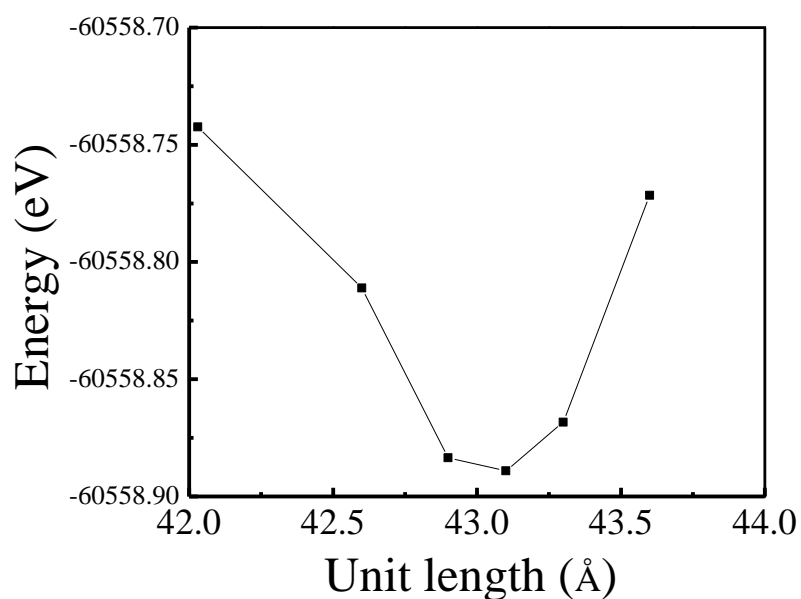


Figure 1 (a) A side view of geometric structure of chemically modified graphene (in x - z plane), where two neighboring zig-zag carbon chains are modified by OH groups and the two chains adjacent to them are modified by F atoms. The unmodified strip has $m = 16$ zig-zag carbon chains. Green, red, purple and white spheres denote C, O, F, and H atoms, respectively. (b) The

energy per supercell of modified graphene vs the unit length L_1 . The optimized unit length of graphene $L_1 \sim 43.1 \text{ \AA}$.

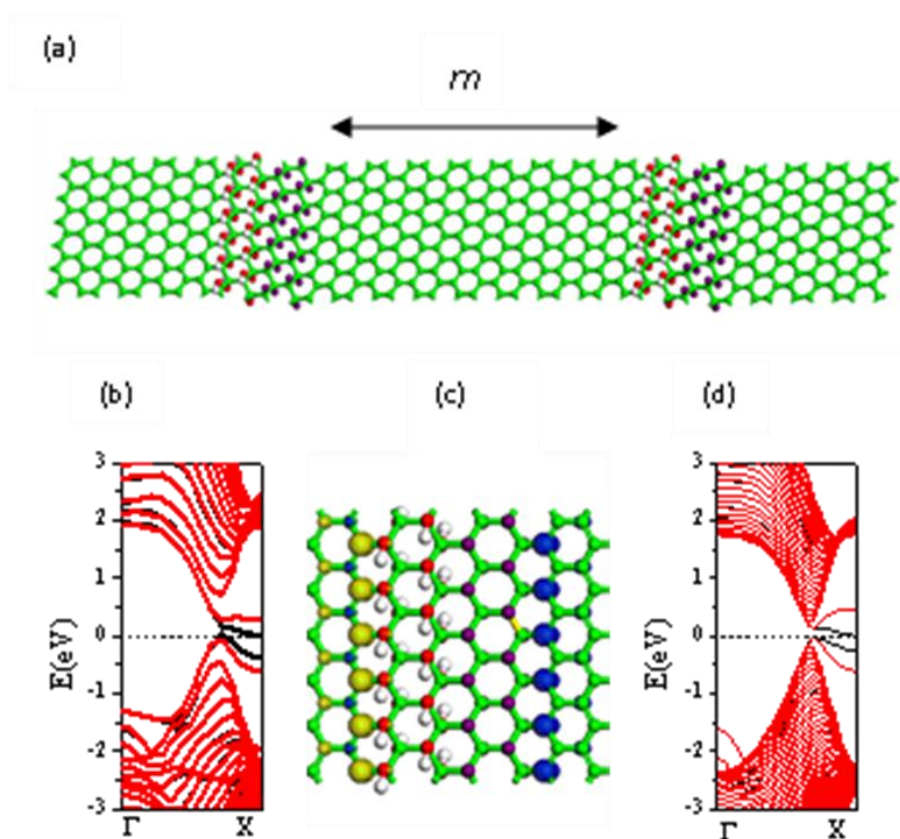


Figure 2 (a) Geometric Structure, (b) band structure and (c) spin density distribution of chemically functionalized graphene, where two neighboring zig-zag carbon chains are functionalized by OH groups and the two chains next to them are functionalized by F atoms. The unfunctionalized strip has $m = 16$ zig-zag carbon chains. Green, red, purple and white spheres denote C, O, F, and H atoms, respectively. Blue and yellow represent isosurface of α and β spin density, respectively. The range of isovalues for spin density is within $[-0.03, 0.03]$. (d) Band structure of graphene chemically functionalized with two chains of H and two chains of F. The

unfunctionalized strip has $m = 72$ zig-zag carbon chains. Red and black lines denote α and β spin channel, respectively.

In summary, we have studied electronic properties of graphene modified by OH groups and F atoms. We show that the functionalized graphene can mimic electronic behavior of edge functionalized ZGNR. ZGNRs are commonly produced by “cutting” graphene by hot plasmas, which may result in edge defects with impurities that can suppress spin polarization. Alternatively the standard lithographic techniques may be less intrusive to the graphene structure than direct “cutting” for implementing flexible chemical functionalization thereby converting graphene to a half metal.

3.4 Magnetic quantum dot arrays

Here we designed various patterned graphenes via selective hydrogenation. Specifically, we used the number of pristine carbon edges (n) in the supercell as a measure of the side length of an uncoated carbon triangle, and the number of hydrogenated zigzag chains (m) as a measure of the width of a hydrogenated carbon stripe. Hence, the size of the rhomboid supercell can be characterized based on m and n (see Fig. 3). As shown in Fig. 3(a), when an array of carbon triangles ($n = 2$) is separated by single hydrogenated zigzag carbon lines ($m = 1$), each carbon atom on the edges exhibits a local magnetic moment of $0.68\mu_B$. This moment is comparable to $\sim 0.8\mu_B$ per edge atom shown in Ref. 7 (where the zigzag edges are not chemically terminated), but much larger than $\sim 0.1\mu_B$ per edge atom shown in Ref. 13 (where

the zigzag edges are terminated by hydrogen). However, in the ground state, two nearest-neighbor carbon triangles are coupled antiferromagnetically. The calculated formation energy per H atom is 2.17 eV, which is less than the formation energy per H atom in graphane (3.95 eV), but still larger than the cases of chemisorption of hydrogen pairs on graphene (0.5-1.5eV) in Ref.4. As the length scale of uncoated carbon triangle increases from $n = 2$ to $n = 4$ and 6, as shown in Fig. 3(b) and (c), it can be seen more clearly that the magnetic moments are mainly localized at those carbon atoms on the edges, especially on the vertexes of the carbon triangles.

In contrast, when the width of hydrogenated carbon stripes increases from $m = 1$ to 2, as shown in Fig.3(d) and (e), the FM state seems to be the ground state as the FM state is 1.2 and 0.55 meV per unit cell lower in energy than the AFM state for $n = 2$ and $n = 1$, respectively. Note that in this case, the unified geometric rule is not applicable. It seems that the magnetic coupling across the hydrogenated strip between two triangles changes its sign from negative to positive when the width of strip increases to $m = 2$. The formation energy per H atom is 2.48 and 2.43 eV, respectively for $n = 2$ and $n = 1$, which is greater than that for $n = 2$ and $m = 1$ as the carbon atoms are more densely hydrogenated. Interestingly, as the width of hydrogenated carbon stripes increases further to $m = 3$, the AFM state becomes the ground state again. As shown in Fig.3 (f), for $n = 2$ and $m = 3$, the AFM state is 0.42 meV per unit cell lower in energy than the FM state. These results suggest that the magnetic coupling (either FM or AFM) between nearest-neighbor carbon triangles can be controlled by changing the width of hydrogenated carbon stripes m . Note that the magnitude of magnetic coupling decreases drastically as m increases.

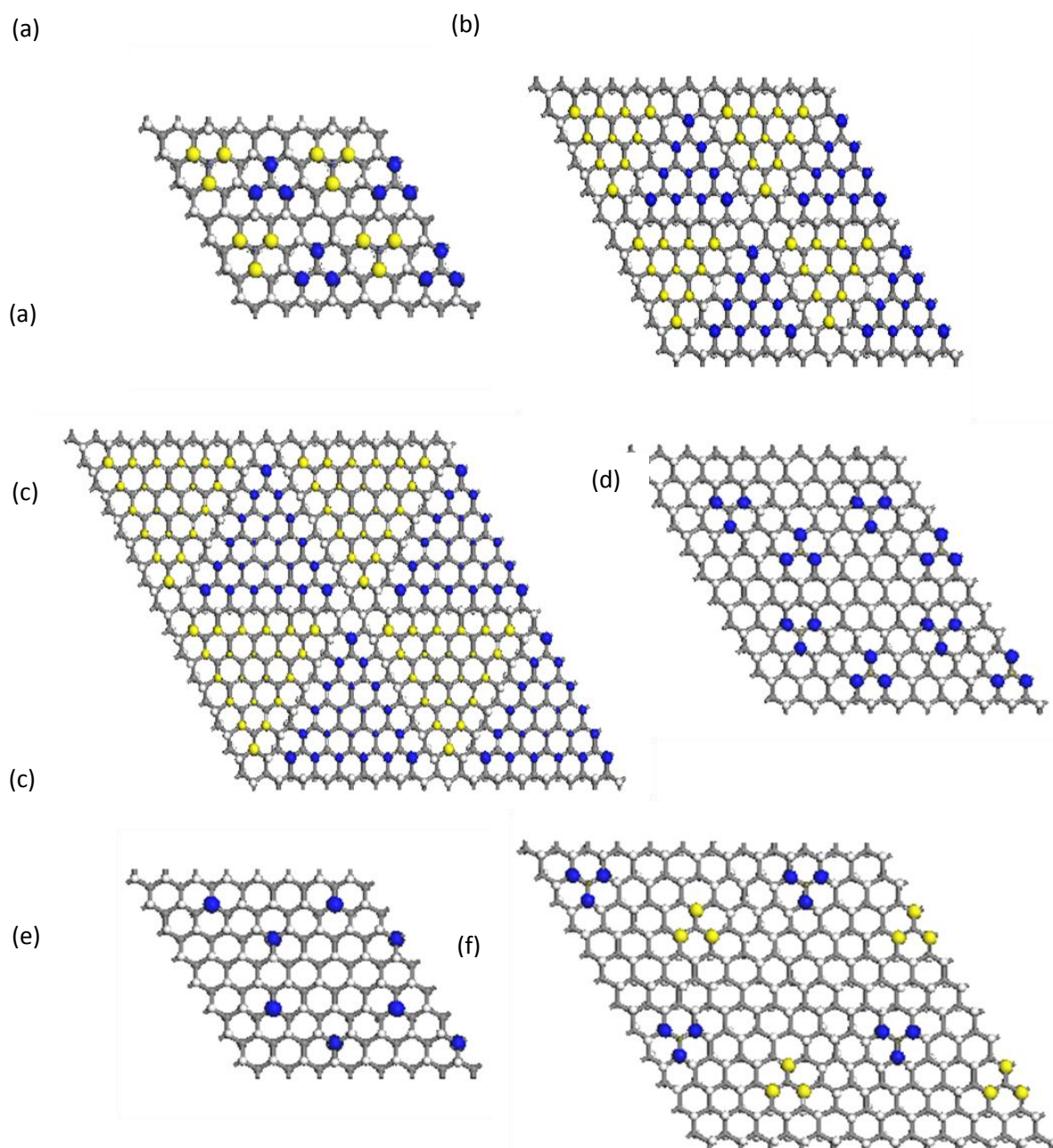


Figure 3. Spin density distribution on selectively hydrogenated graphene for (a) $n = 2$, $m = 1$; (b) $n = 4$, $m = 1$; (c) $n = 6$, $m = 1$; (d) $n = 2$, $m = 2$; (e) $n = 1$, $m = 2$; and (f) $n = 2$, $m = 3$, where m and n measure the width of hydrogenated carbon stripes and the number of uncoated edge carbon atoms, respectively. Grey and white balls represent C and H atom, respectively. Blue and yellow denote spin-up and spin-down density, respectively. Iso-values of spin density range from -0.1 to 0.1.

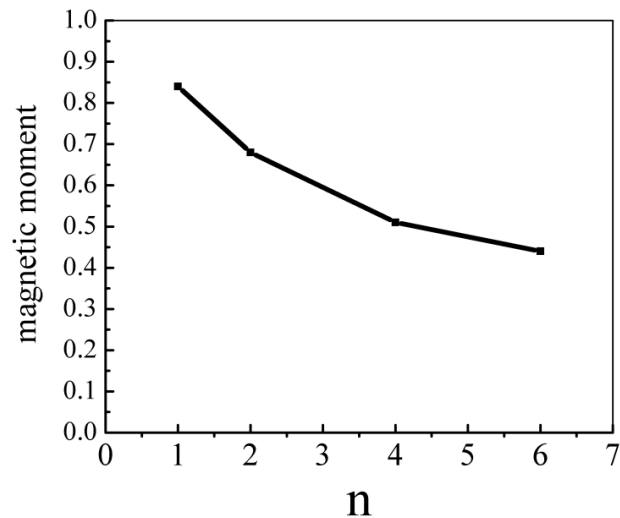


Figure 4. Dependence of average magnetic moment per carbon atom at the edges on the side length of carbon triangles n (for $m = 1$).

Moreover, the dependence of average magnetic moment per edge carbon atom on the side length of carbon triangle n is shown in Fig. 4, where it shows that the average magnetic moment per carbon atom at the edges decreases as n increases.

To investigate electronic properties of the selectively hydrogenated graphenes, we computed their electronic band structures as shown in Fig. 5. For $n = 2$ and $m = 1$, the electronic band structure (Fig. 5(a)) suggests that the chemically modified graphene is semiconducting with an indirect band gap of ~ 1.08 eV. For $n=2$ and $m=2$, the ground state is FM and its band structure is spin polarized, as shown in Fig. 5(b). As n increases to 4, the system is still semiconducting with a band gap of \sim

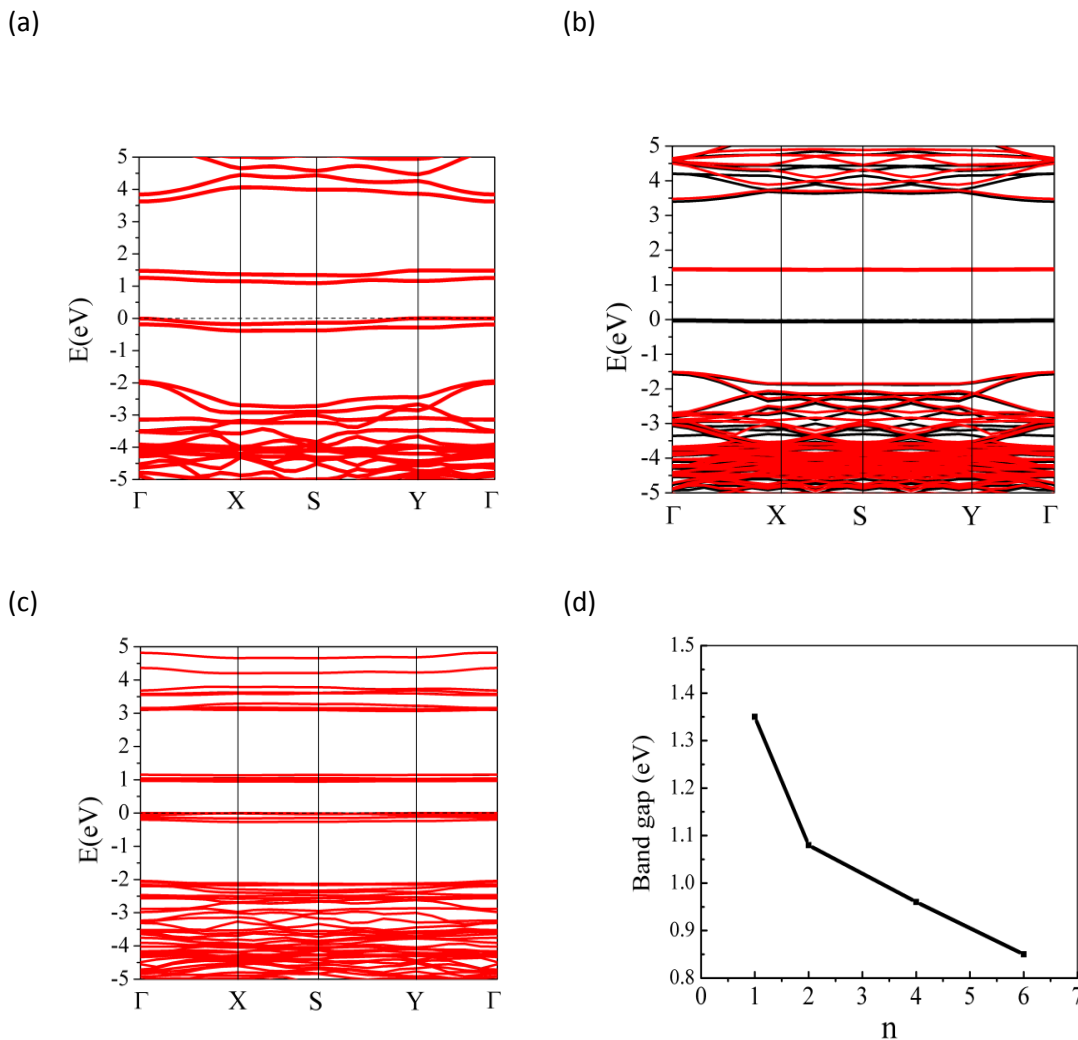


Figure 5. Electronic band structures of selectively hydrogenated graphene for (a) $n = 2, m = 1$; (b) $n = 2, m = 2$; and (c) $n = 4, m = 1$. $\Gamma(0.0, 0.0, 0.0)$, $X(0.0, 0.5, 0.0)$, $S(0.5, 0.5, 0)$ and $Y(0.5, 0.0, 0.0)$ refer to special symmetry points in the first Brouillon Zone. The black dotted line denotes the Fermi level. Black and red lines in (b) refer to spin-up and spin-down channel, respectively. (d) Dependence of the calculated band gap on n ($m = 1$).

0.95 eV (Fig. 5(c)). The bands near the Fermi level are quite flat, bearing resemblance of typical band structures of quantum dots[16]. Figure 5(d) displays the dependence of band gap on the side length of carbon triangle n . It suggests that the band gap decreases as n

increases, again, akin to typical band-gap behavior of quantum dots. In this aspect, the uncoated carbon triangle array may be viewed as a quantum-dot array, where the quantum confinement is enforced by hydrogenated carbon stripes.

It is known that quantum dots can find applications in light-emitting devices[17]. We therefore computed optical absorption spectra of the chemically modified graphenes, using a spin-polarized DFT method within the GGA in the PBE functional form implemented in the CASTEP package in Material Studio[18]. For comparison, the optical spectra of a pristine graphene and a fully hydrogenated graphene (i.e. graphane) are computed and shown in Figs. 6(a) and (b), respectively. Figures 6(c) to (e) display the optical spectra of three chemically modified graphenes. It can be seen that (1) upon selective hydrogenation, the high-energy absorption band of the pristine carbon is either diminished or significantly weakened. On the other hand, a fully hydrogenated graphene (i.e., a graphane) completely diminishes the low-energy absorption band around 4 eV. (2) As n increases from 2 to 6, the highest peak of the low-energy band is shifted from ultraviolet to visible-light regime. Hence, the side length of uncoated carbon triangles can be controlled to adjust optical absorption properties of the quantum-dot array for potential light-emitting application by design.

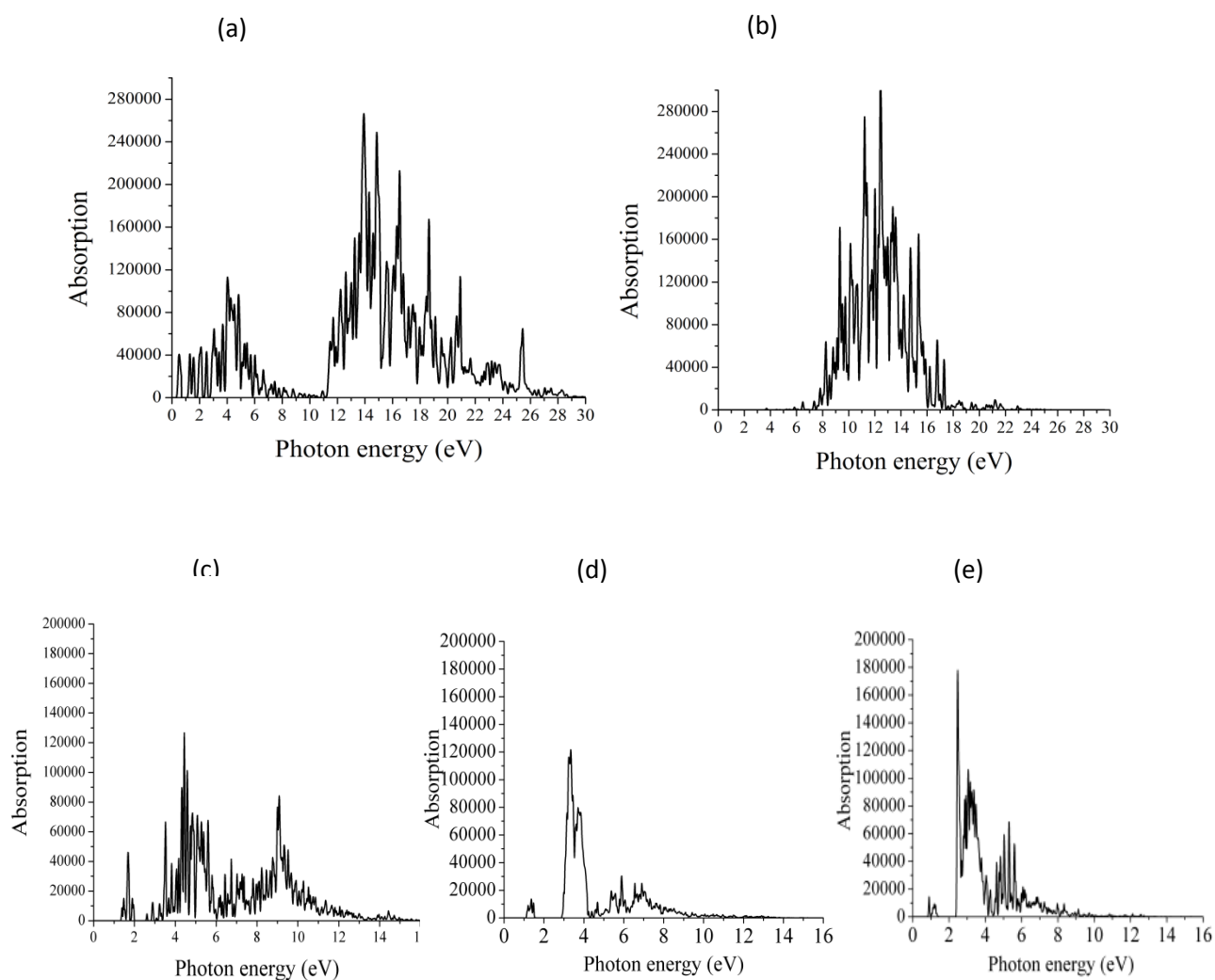


Figure 6. Optical absorption spectra of (a) a pristine graphene, (b) a fully hydrogenated graphene (i.e. graphane), and the selectively hydrogenated graphene for (c) $n = 2$, $m = 1$; (d) $n = 4$, $m = 1$; (e) $n = 6$, $m = 1$, respectively.

In summary, we present a first-principle study of chemically modified graphenes, containing an array of uncoated carbon triangles separated by hydrogenated carbon stripes.

As such, every carbon triangle exhibits a sizable magnetic moment, and the chemically modified graphene through selective hydrogenation can be viewed as a magnetic semiconducting quantum-dot array. Moreover, the magnetic moment, band gap, and optical properties of the magnetic quantum-dot array can be tuned by changing the width of hydrogenated carbon stripes or the side length of carbon triangles. Graphene-based quantum dots are potentially useful for building solid-state quantum computers, as the spin-orbit coupling is relatively weak in carbon and the spin decoherence can be avoided[19]. Previous theoretical work on graphene-based quantum dots suggested that the quantum confinement can be achieved by applying gate voltages locally[19-21]. However, this method is still challenging to implement in the experiment. The quantum confinement achieved by hydrogenated carbon stripes offers an alternative way to attain graphene-based magnetic quantum-dot arrays.

3.5 References

- (1)Ryu, S.; Han, M.Y.; Maultzsch, J.; Heinz, T.F.; Kim, P.; Steigerwald, M.L.; Brus, L.E. *Nano Lett.* **2008**, *8*, 4597.
- (2)Elias, D.C.; Nair, R.R.; Mohiuddin, T.M.G.; Morozov, S.V.; Blake, P.; Halsall, M.P.; Ferrari, A.C.; Boukhvalov, D.W.; Katsnelson, M.I.; Geim, A.K.; Novoselov, K.S. *Science* **2009**, *323*, 610.
- (3)Sofo, J.O., Chaudhari, A. S., Barber, G. B. *Phys. Rev B* **2007**, *75*, 153401.
- (4)Boukhvalov, D.W.; Katsnelson, M.I; Lichtenstein, A.I. *Phys. Rev B* **2008**, *77*, 035427.
- (5)Singh, A. K.; Yakobson, B.I. *Nano Lett.* **2009**, *9*, 1540.
- (6) Wu, M.; Wu, X.; Gao, Y.; Zeng, X.C. *Appl. Phys. Lett.* **2009**, *94*, 223111.

- (7) Lee, H.; Son, Y.W.; Park, N.; Han, S.; Yu, J. *Phys. Rev. B* **2005**, 72, 174431.
- (8) Pisani, L.; Chan, J. A.; Montanari, B.; Harrison, N. M. *Phys. Rev. B* **2007**, 75, 064418.
- (9) Son, Y. W.; Cohen, M. L.; Louie, S. G. *Nature* **2006**, 444, 347.
- (10) Huang, B.; Liu, F., Wu, J.; Gu, B. L.; Duan, W. *Phys. Rev B* **2008**, 77, 153411.
- (11) Fernandez-Rossier, J.; Palacios, J. J. Sofo, J.O., Chaudhari, A. S., Barber, G. B. *Phys. Rev. Lett* **2007**, 99, 177204.
- (12) Wang, W. L.; Meng, S.; Kaxiras, E. *Nano Lett.* **2008**, 8, 241.
- (13) Yu, D.; Lupton, E.M.; Liu, M.; Liu, W.; Liu, F. *Nano Res.* **2008**, 1, 56.
- (14) Yu, D.; Lupton, E.M.; Gao, H. J.; Zhang, C.; Liu, F. *Nano Res.* **2008**, 1, 497.
- (15) Koskinen, P.; Malola, S.; Hkkinen, H. *Phys. Rev. Lett.* **2008**, 101, 115502.
- (16) Reimann, S. M.; Manninen, M. *Rev. Mod. Phys.* **77**, 1283-1342 (2002).
- (17)(a) Park, N. M.; Kim, T. S.; Park, S.J. *Appl. Phys. Lett.* **78**, 2575 (2001). (b) Chaudhary, S.; Ozkan, M.; Chan, W.C.W. *Appl. Phys. Lett.* **84**, 2925 (2004). (c) Li, Y.; Rizzo, A.; Mazzeo, M.; Carbone, L.; Manna, L. Cingolani, R. *J. Appl. Phys.* **97**, 113501 (2005).
- (18) Segall, M. D.; Lindan, P. J. D.; Probert, M. J.; Picakard, C. J.; Hasnip, P. J.; Clark, S. J.; Payne, M. C. *J. Phys.: Condens. Matter* **14**, 2717 (2002).
- (19) Silvestrov, P. G.; Efetov, K.B. *Phys. Rev. Lett.* **2007**, 98, 016802.
- (20) Rycerz, A.; Tworzydło, J.; Beenakker, C.W.J. *Nat. Phys.* **2007**, 3, 172.
- (21) Trauzettel, B.; Bulaev, D. V.; Loss, D.; Burkard, G. *Nat. Phys.* **2007**, 3, 192.

4 Single-layer BN and other hexagonal systems

4.1 Introduction

A graphene-like 2D matter that was isolated recently is the single-layer hexagonal BN (SL-h-BN) [1-6]. In contrast to graphene which is a semi-metal, a SL-h-BN is wide-gap semiconductor [7-9]. Furthermore, a SL-h-BN can be cut into BN nanoribbons (BNNRs), i.e., narrow strips of hexagonal BN. A special class of BNNRs with either zigzag or armchair edges are commonly referred as zigzag-edged (z-BNNRs) or armchair-edged nanoribbons (a-BNNRs) [10-18]. Previous studies have shown that both z-BNNRs and a-BNNRs are nonmagnetic semiconductors although their electronic properties can be tunable by applying an in-plane transverse electric field [17-18]. For z-BNNRs, the unpassivated zigzag edges can also exhibit field-dependent magnetic behavior. In addition, some other Q1D inorganic structures such as AlN, GaN, SiC and ZnO nanotubes and nanoribbons have been investigated by theoretical studies [19-22]. In this chapter we will show first-principles calculation evidence that a class of 2D honeycomb group-III/V (BN, BP, AlN, AlP) systems, including their nanoribbons, can all exhibit novel magnetic properties upon charge injection. Subsequently we will present a study on some of their nanoribbons with unpassivated edges.

4.2 Computation details

The DFT calculations are carried out using Dmol³ package. The GGA in the PBE form together with the DNP basis set with polarized function are chosen for the spin-unrestricted DFT computation. The real-space global cutoff radius is set to be 3.7 Å. To simulate inorganic nanoribbons, a rectangular supercell with dimension $36 \times L \times 16$ Å³ is built, where L is chosen to be twice of the width of the hexagonal ring and hence it depends on the type of the nanoribbon

considered. The nearest distance between the nanoribbon and its nearest image (under periodic boundary conditions) is greater than 16 Å. For 2D systems a rhomboid supercell in the plane and a vacuum layer of 16 Å were constructed. For geometric optimization, the Brillouin zone is sampled with $1 \times 20 \times 1$ (1D) or $6 \times 6 \times 1$ (2D) k points using the Monkhorst-pack scheme. After geometric optimization, the forces on all atoms are less than 0.0002 Ha/ Å. For charged systems, a neutralizing background charge is assumed automatically, identical to the original charged system immersed in a jellium background filling the supercell, according to the methods described in Ref.30. To further confirm predicted half metallicity for certain inorganic, we re-examined their band structures using the screened exchange hybrid Heyd-Scuseria-Ernzerhof (HSE) [23,24] functional and the 6-31G basis set (implemented in the Gaussian 09 package). The reaction pathways were computed using nudged elastic band method [25] implemented in Dmol³.

4.3 Charge-Injection Induced Magnetism and Half Metallicity in Single-Layer Hexagonal Group III/V (BN, BP, AlN, AlP) Systems

Figure 1 displays the spin density distribution of (a) a SL-h-BN, (b) a z-BNNR and (c) an a-BNNR. The 4x4 supercell for all three systems contains 16 B and 16 N atoms, with a charge injection being 2e (hole injection) or -2e (electron injection) per supercell, respectively. Remarkably, injecting holes can substantially induce a magnetic moment on each N atom, whereas injecting electrons can induce a moment on each B atom. The DFT calculations show that the ferromagnetic (FM) state is the ground state while the antiferromagnetic (AFM) state is nonexistence. For the SL-h-BN, the induced magnetic moments distribute uniformly on N or B atoms over the entire 2D sheet, whereas for finite-size BNNRs, the moments mainly distribute near the two edges. The calculated band structures suggest that the BN nanostructures are half metals upon electron injection but spin-polarized metals upon hole injection. Based on the

Hirshfeld charge analysis, we find that the total magnetic moment in all three BN systems is $2\mu_B$ upon charge injection of $-2e/\text{supercell}$. This indicates that the charge is fully spin-polarized. When the three BN systems are charged by $2e/\text{supercell}$, the magnetic moment of system (a)-(c) is 1.51, 1.34, $0.652\mu_B$, respectively.

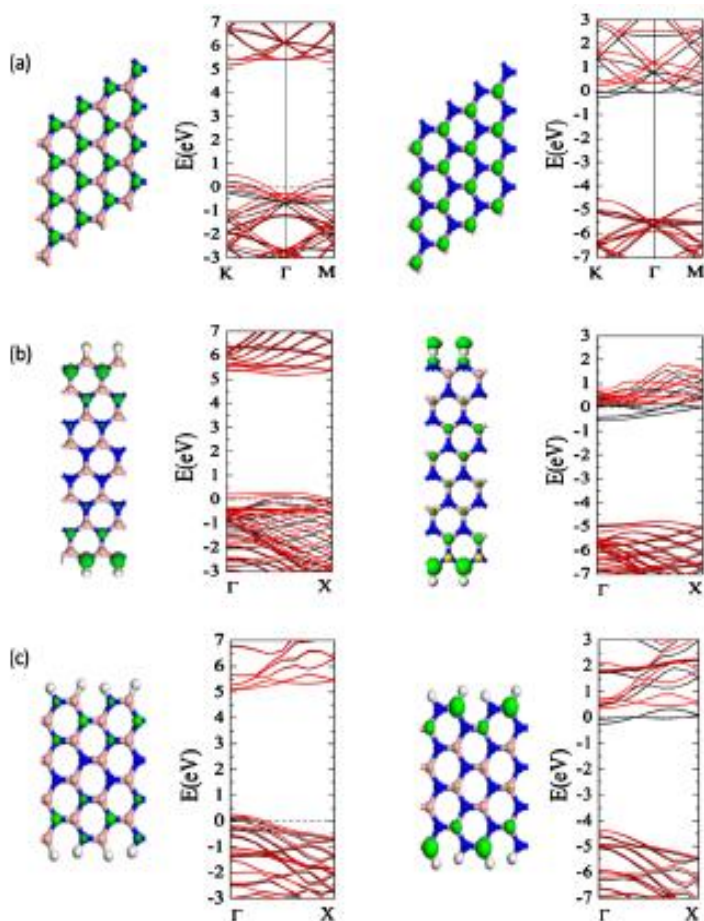


Figure 1 Spin density distribution and band structures of (a) SL-h-BN, (b) z-BNNR and (c) a-BNNR when they are charged by $2e$ (left panel) and $-2e$ (right panel) per supercell. Pink, blue and white spheres denote B, N, and H atoms, respectively. Green and yellow represent isosurface of α and β spin density, respectively. The range of isovalues for spin density is within $[-0.03,$

0.03]. In band structures red and black lines denote α and β spin channels, respectively. The dashed line denotes the Fermi level.

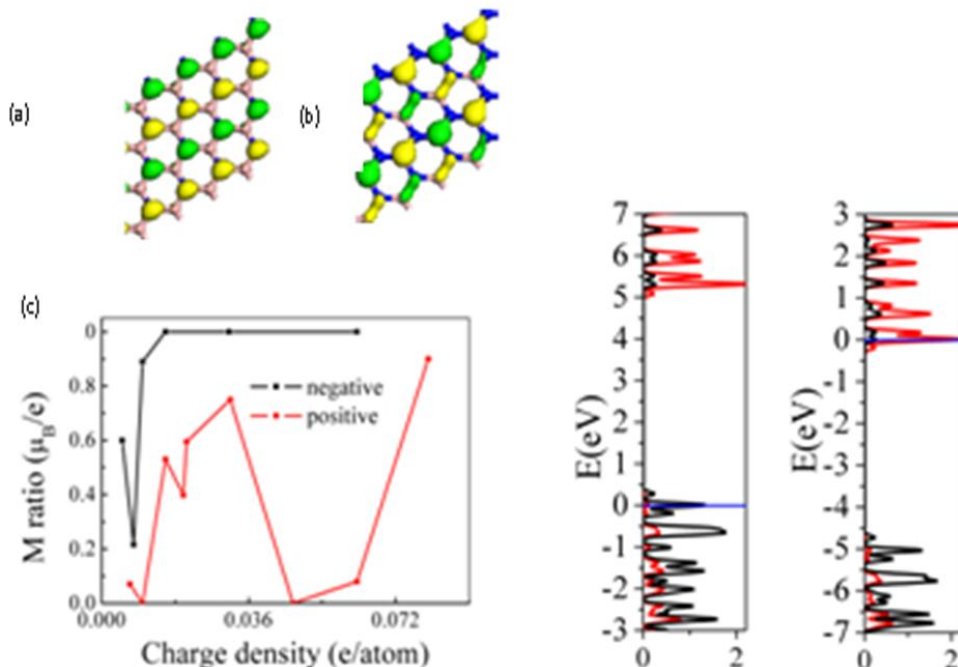


Figure 2 (a) HOCO and LUCO of an uncharged SL-h-BN. (b) Spin-unpolarized PDOS of a B and an N atom in the SL-h-BN in 2e (left panel) and -2e (right panel) charge states. (c) M ratio dependence on the injected charge per atom. In (b) red and black lines denote the PDOS of B and N, respectively, and the blue line denotes the Fermi level.

To understand the origin of strong ferromagnetism in the three BN nanostructures, the highest occupied crystalline orbitals (HOCO) and lowest unoccupied crystalline orbitals (LUCO) of an uncharged SL-h-BN at the gamma (Γ) point are displayed in Fig. 2. The HOCO is mainly contributed by N atoms, while LUCO by B atoms. According to the Stoner criterion [26], the transition from a paramagnetic to ferromagnetic (FM) state occurs if $I\rho(E_F) > 1$, where I is the

Stoner parameter and $\rho(E_F)$ is the density of states (DOS) of the paramagnetic state at the Fermi level. If the Stoner criterion is met, the FM state would be favorable. The spin-unpolarized band structure and projected DOS (PDOS) of a B atom and an N atom of the SL-h-BN, charged by $2e$ and $-2e$ per supercell respectively, are displayed in Fig. 3 and Fig. 2(b). Upon positive charge injection, the Fermi level downshifts and $\rho(E_F)$ of N atoms greatly increases (see left panel in Fig. 2(b)). Hence, when $I\rho(E_F) > 1$, N atoms should exhibit ferromagnetism. Likewise, upon negative charge injection, the Fermi level upshifts and $\rho(E_F)$ of B atoms will increase and B atoms should exhibit ferromagnetism. As shown in Fig. 2(b), $\rho_B(E_F)=1.5/eV$ (in $-2e$ charge state) is larger than $\rho_N(E_F)=0.37/eV$ (in $2e$ charge state), which explains why the charge state of $-2e$ can induce $2.0\mu_B$ but the charge state of $2e$ only induces $1.51\mu_B$ in the SL-h-BN. Moreover, the greater exchange splitting in the $-2e$ charge state induces half metallicity. By defining the ratio of magnetic moment to charge as M , the dependence of M on the extra charge per atom is shown in Fig. 2(c). When the BN system is in a negative charge state, the injected charge will be fully spin-polarized even at high charge density. However, in the positive charge state, no general trend is seen.

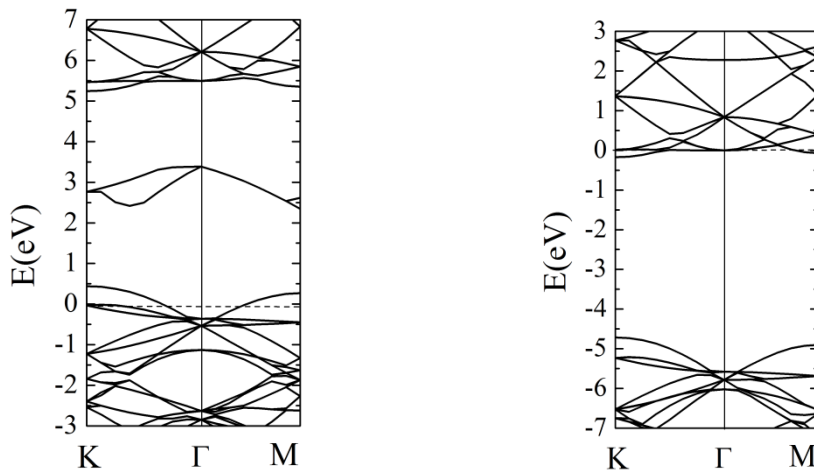


Figure 3 Spin-unpolarized band structure of SL-h-BN with $2e$ (left) and $-2e$ (right) charge injection per supercell, respectively. $\Gamma(0.0, 0.0, 0.0)$, $M(0.0, 0.5, 0.0)$, $K(-0.333, 0.667, 0)$ refer to special symmetry points in the first Brillouin zone.

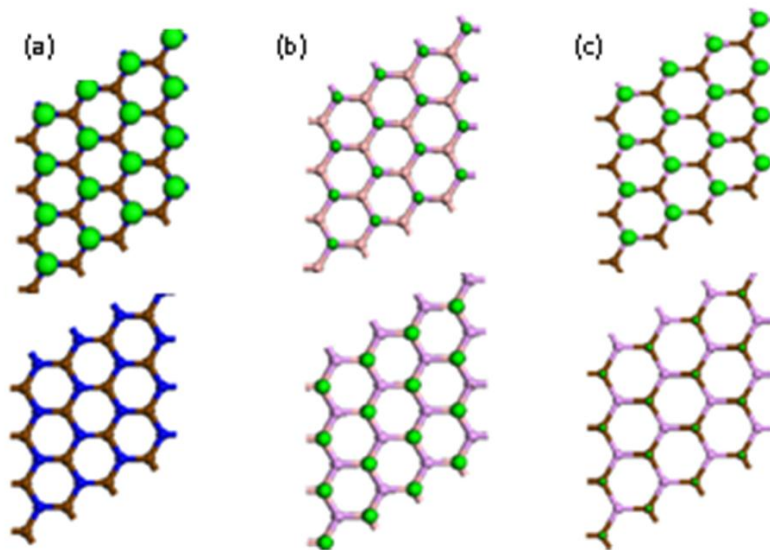


Figure 4 Spin density distributions of a (a) SL-h-AIN, (b) SL-h-BP and (c) SL-h-AIP in $2e$ (upper panels) and $-2e$ (lower panels) charge state, respectively. Pink, blue, brown and purple spheres denote B, N, Al and P atoms, respectively. Green and yellow represent isosurface of α and β spin densities, respectively. The range of isovalues for spin density is within $[-0.01, 0.01]$.

Table 1 Magnetic moment per supercell at the injection of charge of absolute value $|2e|$, M ; PDOS at Fermi level when the system starts to exhibit magnetism, $\rho(E_F)$; and estimated Stoner parameter I , of SL-h-BN, SL-h-AIN, SL-h-BP and SL-h-AIP. +, - represent positive and negative charge: at positive charge $\rho(E_F)$ is the PDOS for a group-IV atom, but at negative charge it is the PDOS for a group-III atom in the systems.

	SL-h-BN		SL-h-AIN		SL-h-BP		SL-h-AIP	
	+	-	+	-	+	-	+	-
$M(\mu_B)$	1.51	2.0	2.0	0	0.73	0.91	1.28	0.93
$\rho(E_F)$ (eV^{-1})	0.29	0.31	0.92	1.1	0.48	0.35	0.93	1.11
$I(eV)$	3.45	3.23	1.09	0.91	2.08	2.85	1.07	0.90

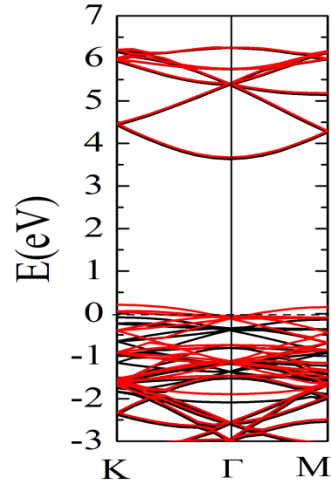


Figure 5 Spin-polarized band structure of SL-h-AIN with 2e charge injection per supercell. $\Gamma(0.0, 0.0, 0.0)$, $M(0.0, 0.5, 0.0)$, $K(-0.333, 0.667, 0)$ refer to special symmetry points in the first Brillouin zone. Red and black lines denote α and β spin channels, respectively.

In addition, we find that such charge-injection induced spin-polarization is quite universal in all 2D honeycomb group-III/V systems, e.g., SL-h-AIN, SL-h-BP and SL-h-AIP. In Fig. 4, we show the spin density distribution for SL-h-AIN, SL-h-BP and SL-h-AIP in 2e charge state, respectively; their supercell exhibits a magnetic moment of 2.0, 0.73, and 1.28 μ_B , which is distributed mainly on N, P and P atoms, respectively; when they are in -2e charge state, the magnetic moment will be 0, 0.91 or 0.92 μ_B , which is distributed on the Al, B and Al atoms, respectively (see Table 1). Compared to the induced local moments shown in Fig. 1, here the local moments on Al and P are much smaller. We estimate the Stoner parameter I for these 2D

systems using the following method: we assumed that as the injected charge density is slowly increased from zero and when the systems begin to exhibit magnetism, $I\rho(E_F) = 1$ is more or less satisfied. Thus, by calculating corresponding $\rho(E_F)$ we can estimate the parameter I . In Table 1 one can see that the Stoner parameter I for SL-h-AIP is around 0.90~1.07, which is smaller than that for SL-h-BN 3.23~3.45. This is in part because $3p$ orbitals are more delocalized than $2p$ orbitals, hence less favorable for the spin polarization. Regarding electronic properties, the SL-h-AlN is also predicted to be half metallic in the $2e$ charge state (see Fig. 5). The calculated values of I here are very large compared with that of transition metals in Ref.31, probably due to different characteristics of covalent-bonding systems.

In summary, we predict, based on first-principles calculations, that a SL-h-BN and BN nanoribbon can become ferromagnetic or even half metallic in certain charge states. Other 2D honeycomb group-III/V systems, such as SL-h-BP, SL-h-AlN and SL-h-AIP, exhibit similar ferromagnetic behavior upon charge injection. Like SL-h-BN, a SL-h-AlN can be converted to half metal at certain charge states as well.

4.4 Inorganic Nanoribbons with Unpassivated Zigzag Edge: Half Metallicity and Edge Reconstructions

In Ref. 21, Zheng et.al showed from the first-principles calculation that the zigzag BN nanoribbon (zBNNR) can be half metallic if its N edge is unpassivated. It would be interesting to see whether the same electronic behavior can be seen in other inorganic nanoribbons with unpassivated edges. Nevertheless, unpassivated edges could be very unstable and if so edge reconstructions may take place, akin to structural reconstructions of the unpassivated edges of GNRs [27]. In this article, we present calculated electronic structures of a number of inorganic

zigzag nanoribbons, including the group-III nitrides, the group-III phosphorides, SiC and ZnO, based on DFT calculations. We find that some of these nanoribbons with either one or two unpassivated edges can be half metallic. Possible edge reconstruction on all unpassivated edges is also investigated in detail. Some of unpassivated edges are quite unstable where edge reconstructions can take place above room temperature.

4.4.1 Half Metallicity

We use the number of parallel zigzag chains n in a zigzag-edged nanoribbon to describe the width of the nanoribbon. Here, $n = 8$ is chosen for all the nanoribbons considered. First, we focus on two group-III nitrides, AlN and GaN. In the zigzag-edged AlN nanoribbon (zAlNNR), all the outmost atoms at the Al edge are Al atoms while all the outmost atoms at the opposing edge (i.e., the N edge) are N atoms. As shown in Fig. 6(a), when the Al edge of a zAlNNR is passivated by hydrogen atoms (designated as the zAlNNR-Hal), the calculated band structure suggests that the zAlNNR-HAl is a spin-polarized semiconductor with a band gap of ~ 0.2 eV. When the H atoms on the Al edge are removed, however, the calculated band structure suggests that the pristine zAlNNR is a *half metal*, which is also confirmed by the DFT calculation using the HSE functional. As can be seen in Fig. 6(b), the N edge is ferromagnetic while the Al edge is antiferromagnetic, similar to the pristine zBNNR [28]. In (c) both HOMO and LUMO are revealed to be distributed mainly on edge N atoms. For zGaNNR-HGa, the N atoms at the N-edge is no longer on a single straight line along the ribbon direction but become slightly modulated in a periodic fashion as shown in Fig. 6(d). The calculated band structure suggests that it is a spin-polarized semiconductor. When the H atoms on the Ga edge are removed, it is still a semiconductor although the band gap is reduced to 0.05 eV as shown in Fig. 6(e).

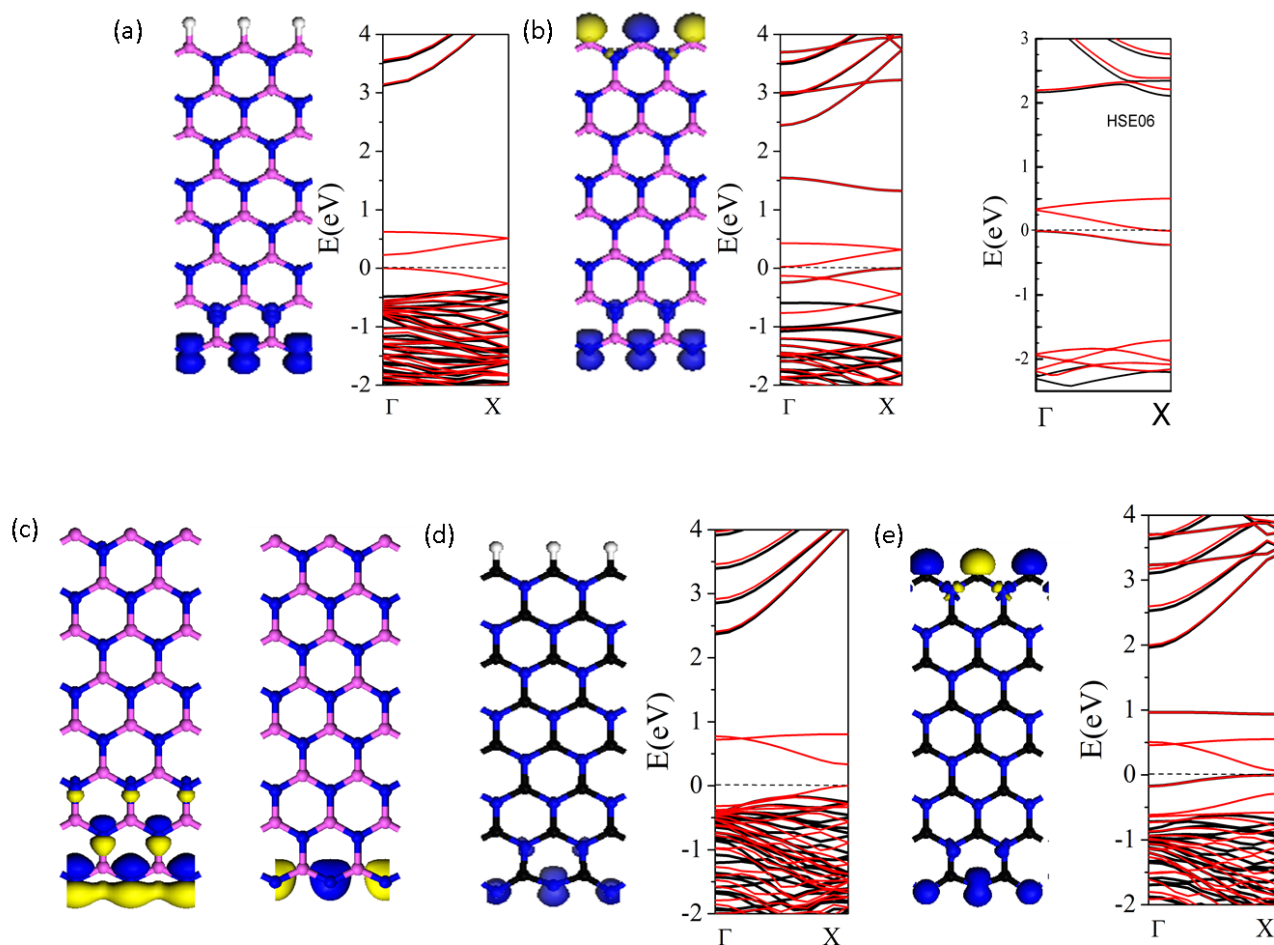


Figure 6 The spin density (left panel) and spin-polarized band structures (right panel) of (a) zAlNNR-HAl, (b) pristine zAlNNR, (d) zGaNNR-HGa, (e) pristine zGaNNR. (c) displays HOMO and LUMO of pristine zAlNNR. Small balls in white, pink, blue, black, and red denote hydrogen, aluminum, nitrogen, gallium, and oxygen atoms, respectively. For spin density, blue and yellow lobes represent spin-up and spin-down regions, respectively; and the range of the iso-values of spin density is $[-0.03, 0.03] e/\text{\AA}^3$. In the band-structure graphs black represents the spin-up channel and red represents the spin-down channel. The Fermi level is denoted by the horizontal dashed line.

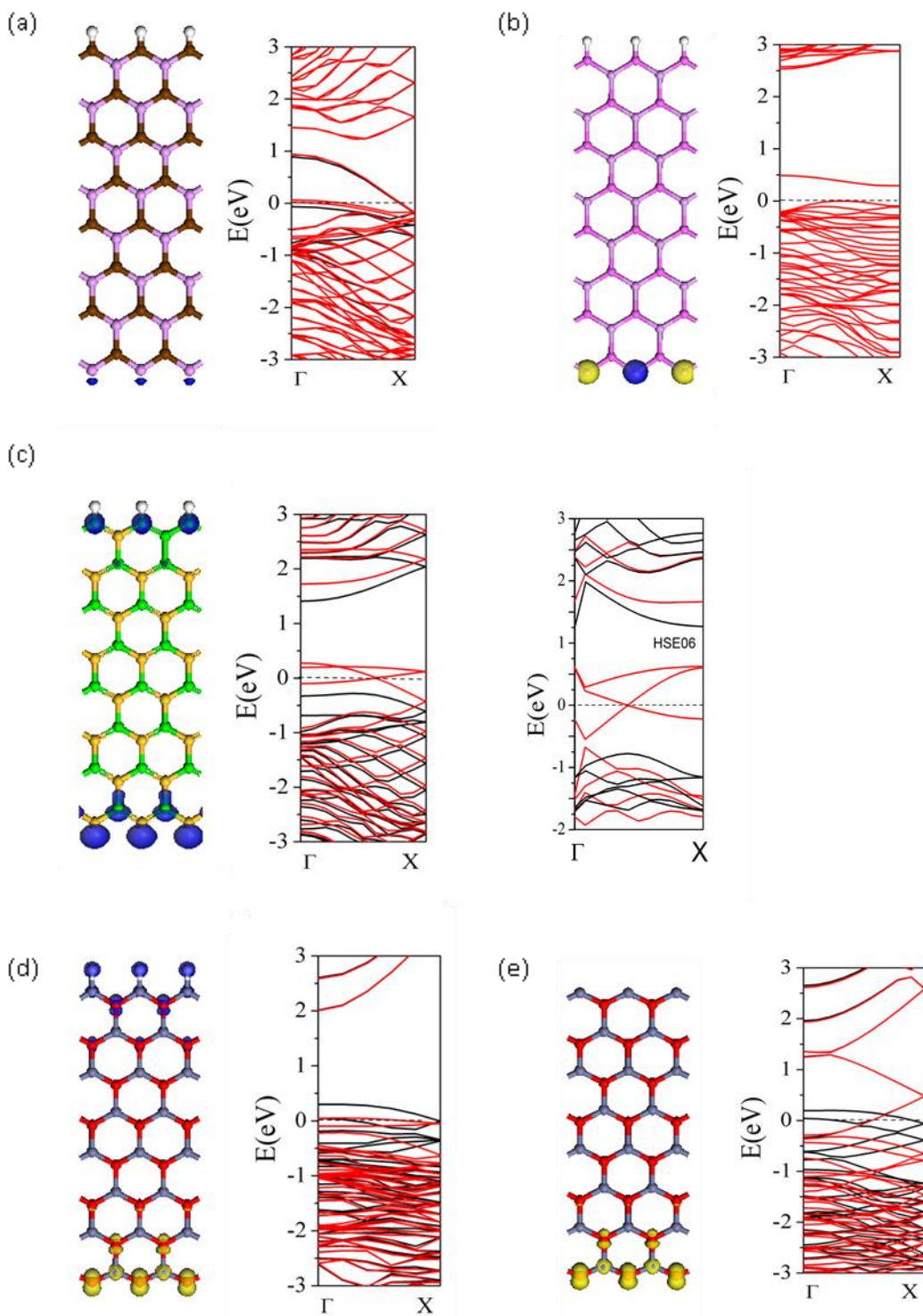


Figure 7 The spin density and spin-polarized band structures of (a) zBPNR-HB, (b) zAlPNR-HAl, (c) zSiCNR-HC, (d) zZnONR-HZn and (e) pristine zZnONR. Small balls in green, white, pink, blue, black, brown, purple, yellow, grey and red denote carbon, hydrogen, aluminum, nitrogen, gallium, boron, phosphorus, silicon, zinc and oxygen atoms, respectively. For spin density, blue and yellow lobes

represent spin-up and spin-down regions, respectively; and the range of the iso-values of spin density is $[-0.03, 0.03] e/\text{\AA}^3$. In the band-structure graphs black represents the spin-up channel and red represents the spin-down channel. The Fermi level is denoted by the horizontal dashed line.

For group-III phosphoride, we consider BP and AlP nanoribbons. As shown in Fig. 7(a), the band-structure calculation suggests zBPNR-HB is metallic if the P edge is unpassivated. For zAlPNR-HAl, the P edge is antiferromagnetic and the system is a spin-unpolarized semiconductor as shown in Fig. 7(b). Besides the group-III/V compounds, we also consider SiC and ZnO nanoribbons. As shown in Fig. 7(c), when the Si edge of zSiCNR-HC is unpassivated, the spin distribution at two edges and in the ground state is ferromagnetically coupled. The nanoribbon is predicted to be a half metal based on the calculated band structure using the PBE and HSE functional, respectively. For zZnONR-HZn shown in Fig. 7(d), the spin distribution at two edges is anti-ferromagnetically coupled, and the nanoribbon is metallic. If all the H atoms at the Zn edge are removed, the nanoribbon is still metallic as shown in Fig. 7(e). It is similar to the ferromagnetism of ZnO nanowires induced by surface partial passivation [29].

4.4.2 Edge Reconstruction

According to Ref. 27, in zGNRs, the reconstruction of an unpassivated zigzag edge can spontaneously take place at room temperature, where two neighboring hexagons can transform into a pentagon and heptagon. Here we investigate similar edge reconstruction that may take place at the unpassivated edges of any inorganic nanoribbons presented here. First, we consider the half metallic zBNNR-HB reported in Ref. 28. As shown in Fig. 8(a-c), the N edge has two ways of reconstructions: (1) it can reconstruct into a symmetric structure shown in Fig. 8(b),

where the pentagon is formed by two N atoms and three boron atoms. This way of edge reconstruction is denoted as the A style. (2) The N edge may reconstruct into an unsymmetrical structure, as shown in Fig. 8(c), where each pentagon is formed by three N atoms and two B atoms. This way of edge reconstruction is denoted as the B style. After the edge reconstruction in the A style, the system is 1.06 eV/supercell higher in energy, while in the B style, the energy is lowered by 0.22 eV/supercell. Hence, the B style is energetically more favorable. Our calculation also shows that the activation barrier for the edge reconstruction in the B style is about 1.0 eV, implying that spontaneous reconstruction of the N edge can be possible above room temperature. The calculated band structure for the reconstructed nanoribbon (in the B style) is shown in Fig. 8(d). Interestingly, upon the edge reconstruction, the nanoribbon is no longer a half metal but becomes a wide-gap semiconductor.

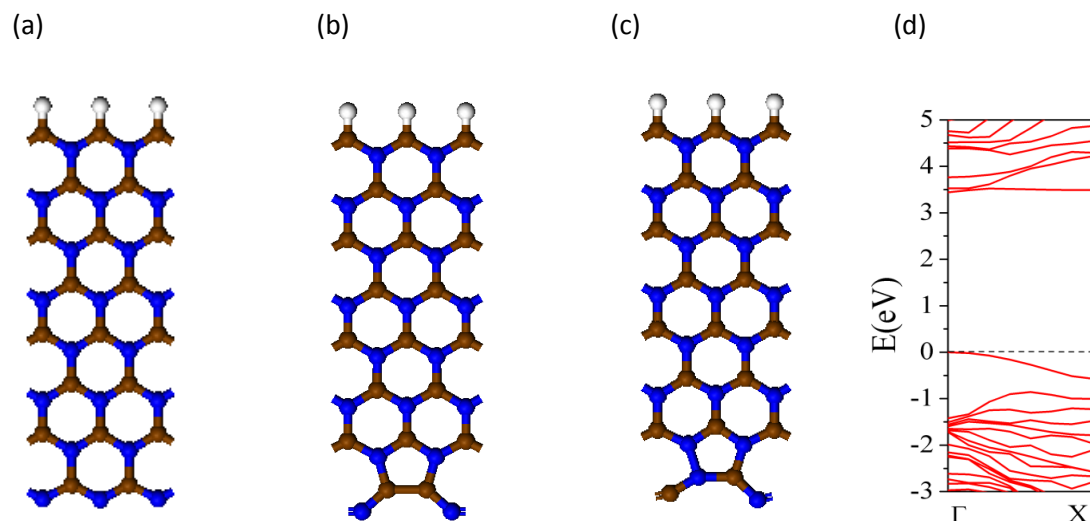


Figure 8 The optimized structures of zBNNR-HB (a) before and after the edge reconstruction in (b) the A style and (c) B style at the N edge. White, blue, and brown balls denote hydrogen, nitrogen, and boron atoms, respectively. The band structure of nanoribbon (c) is shown in (d).

For pristine zAlNNR, we first consider reconstruction of the Al edge. The edge reconstruction in either the A or B style is shown in Fig. 9(a) and (b), respectively. The calculations show that upon the edge reconstruction in the A or B style the energy will be 3.4 eV or 1.4 eV higher, respectively. Hence, the unpassivated Al edge appears to be robust against the edge reconstruction. Figure 9(c) and (d) displays the edge reconstruction at the N edge in the A and B style, respectively. Our calculation shows that upon the edge reconstruction in the A style, the energy will be lowered by 0.26 eV while in the B style it will increase by 0.64 eV. However, even though the edge reconstruction in the A style is energetically favorable, the activation barrier for the edge reconstruction is typically very high (~ 3.5 eV). Hence, it is unlikely for an N atom at the edge to swap position with its nearby Al atom. As a consequence, the unpassivated N edge can still be considered as very stable against edge reconstruction.

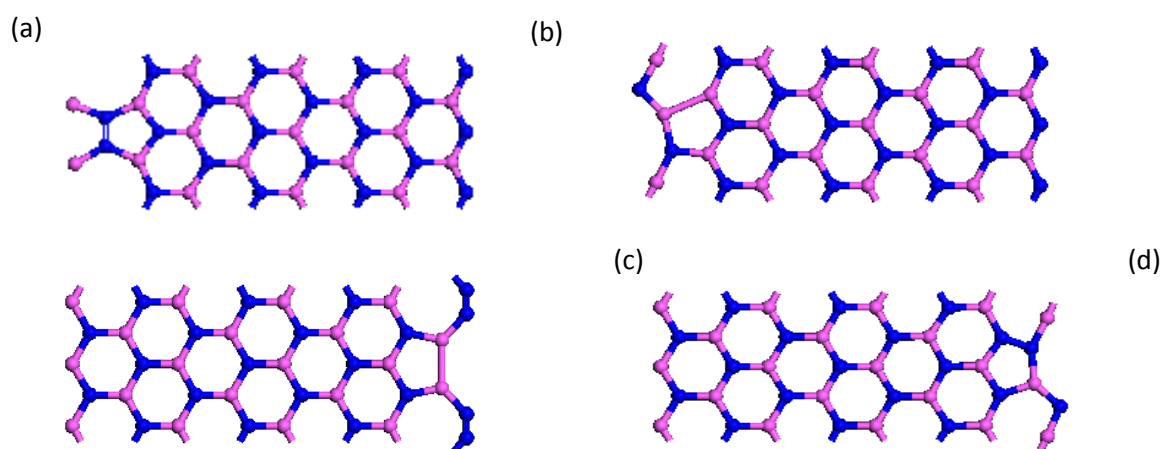


Figure 9 The optimized structures of zAlNNR upon the edge reconstruction in (a) the A style and (b) the B style at the Al edge, and in (c) the A style and (d) the B style at the N edge. Blue and pink balls denote nitrogen and aluminum atoms, respectively.

Table 2 Energy change upon edge reconstruction in the A and B style at the unpassivated edge in zGaNNR-HGa, zBPNR-HB, zAIPNR-HAl, zSiCNR-HC, and zZnONR-HZn.

Reconstruction	zGaNNR-HGa	zBPNR-HB	zAIPNR-HAl	zSiCNR-HC	zZnONR-HZn
A style (eV)	-2.92	1.03	0.18	1.19	2.13
B style (eV)	0.11	1.00	-0.015	1.35	

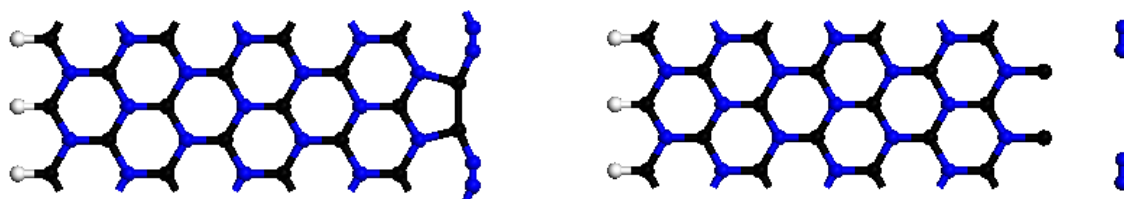


Figure 10 For the edge reconstruction of zGaNNR-HGa in the A style, the edge N atoms will form into free molecules after geometric optimization. White, blue, and black balls denote the hydrogen, nitrogen, and gallium atoms, respectively.

In Table 2, we list energy change upon the edge reconstruction in the A and B style at the unpassivated edge in zGaNNR-HGa, zBPNR-HB, zAIPNR-HAl, zSiCNR-HC, zZnONR-ZnH, respectively. For zGaNNR-HGa, the pentagon and heptagon cannot be stable upon the edge reconstruction in the style A at the N edge because the N atoms will turn into free molecules, as shown in Fig. 10. Also, the energy change for the edge reconstruction of zZnONR-HZn in the B style is not given in Table 1 since the unpassivated O edge recovers its original zigzag structure after the geometric optimization even with the edge reconstruction imposing on it initially.

As shown in Table 2, only the energy of zAIPNR-HAl is lowered upon edge reconstruction in the B style. Moreover, our calculation shows that the activation barrier for the edge reconstruction in this case is about 0.65 eV, implying that the spontaneous edge reconstruction is

conceivable at room temperature. The normal bond lengths of Al-Al, Al-P and P-P are 2.22 Å, 2.21 Å and 2.20 Å, respectively, which are nearly the same. This observation is similar to the case of zBNNR-HB where the normal bond lengths of B-B, B-N and N-N are nearly the same (which are 1.42 Å, 1.45 Å and 1.48 Å, respectively). Considering the edge reconstruction of GNR reported in Ref. 27, it seems that the edge reconstruction in the B style tends to occur at the unpassivated edge where two types of constituent atoms give rise to nearly the same bond length among them.

In conclusion, we show that the unpassivated zigzag edges of inorganic nanoribbons = (BN, AlN, GaN, SiC, and ZnO) can lead to spin-splitting energy bands in general. More interestingly, the inorganic nanoribbons AlN and SiC with either one or two edges unpassivated are predicted to be half metals. Possible structural reconstruction at the unpassivated edges and their effect on the electronic properties are investigated. The unpassivated N edge in the BN nanoribbon and P edge in AlP nanoribbon are unstable and as such the edge reconstruction is likely to occur at these edges above room temperature. Other unpassivated edges in the inorganic nanoribbons considered here are robust against edge reconstruction.

4.5 References

1. Novoselov, K. S.; Jiang, D.; Schedin, F.; Booth, T.; Khotkevich, V. V.; Morozov, S. V.; Geim, A. K. *Proc. Natl. Acad. Sci. U.S. A.* **102**, 10451-10453 (2005).
2. Meyer, J.C.; Chuvilin, A.; Algara-Siller, G.; Biskupek, J.; Kiser, U. *Nano Lett.* **9**, 2683 (2009)
3. Jin, C. H.; Lin, F.; Suenaga, K.; Iijima, S. *Phys. Rev. Lett* **102**, 195505 (2009)

4. Lin, Y.; Williams, T.V. and Connel, J.W. *J. Phys. Chem. Lett.* **1(1)**, 277 (2010)
5. Yu, J.; Qin, L.; Hao, Y.; Kuang, S.; Bai, X.; Chong, Y.; Zhang, W. and Wang, E. *ACS Nano* **4**, 414 (2010).
6. Han, W.-Q.; Wu, L.; Zhu, Y.; Watanabe, K. and Taniguchi, T. *Appl. Phys. Lett* **93**, 223103 (2008)
7. Arnaud, B.; Lebegue, S.; Rabiller, P. and Alouani, M. *Phys. Rev. Lett.* **96**, 206402 (2006)
8. Blasé, X.; Rubio, Al; Louie, S.G. and Cohen, M. L. *Phys. Rev. B* **51**, 6868 (1995).
9. Watanabe, K.; Tniguchi, T.; Kanada, H. *Nat. Mater.* **3**, 404-409 (2004).
10. Chen, R. B.; Chang, C. P.; Chyu, F. L.; Lin, M. F. *Solid State Commun.* **123**, 365-369 (2002).
11. Nakamura, J.; Nitta, T.; Natori, A. *Phys. Rev. B* **72**, 205429 (2005).
12. Nakhmanson, S.M.; Calzolari, A.; Meunier, V.; Bernholc, and Nardelli, M. B.. *Phys. Rev. B* **67**, 235406 (2003).
13. Du, A.; Smith, S. C.; Lu, G. *Chem. Phys. Lett.* **447**, 181 (2007).
14. Chen, W.; Li, Y.; Yu, G.; Li, C.; Zhang, S.-B.; Zhou, Z. and Chen, Z. *J. Am. Chem. Soc.* **132**, 1699 (2010)
15. Topsakal, M.; Akturk, E.; Ciraci, S. *Phys. Rev. B* **79**, 115442 (2009).
16. Chen, W.; Li, Y.; Yu, G.; Zhou, Z. and Chen, Z. *J. Chem. Theory. Comput.* **5(11)**, 3088 (2009)
17. Park, C.-H; Louie, S.G. *Nano Lett.* **8**, 2200 (2008)
18. Zhang, Z.; Guo, W. *Phys. Rev. B* **77**, 075403 (2008).
19. Botello-Mendez, A. R.; Lopez-Urias, F.; Terrones, M.; Terrones, H. *Nano. Lett.* 2008, 8, 1562-1565.

20. Lee., S.M.; Lee, Y. H.; Hwang, Y. G.; Elsner, J.; Porezag, D.; Frauenheim, T. *Phys. Rev. B* 1999, 60, 7788.
21. Du, A. J.; Zhu, Z. H.; Chen, Y.; Lu, G.Q.; Smith, S.C. *Chem. Phys. Lett.* 2009, 469, 183-185.
22. Sun, L.; Li, Y.; Li, Z.; Li, Q.; Zhou, Z.; Chen, Z., Yang, J. L. and Hou, J. G. *J. Chem. Phys.* 2008, 129, 174114.
23. Heyed, J. and Scuseria, G.E. *J. Chem. Phys.* 2004, 121, 1187.
24. Heyed, J.; Peralta, J.E.; Scuseria, G.E. *J. Chem. Phys.* 2005, 123, 174101.
25. (a) Henkelman, G.; Uberuaga, B. P.; Jonsson, H. *J. Chem. Phys.* 2000. 113, 9901. (b) Henkelman, G.; Jonsson, H. *J. Chem. Phys.* 2000. 113, 9978.
26. Stoner, E.C. *Proc. R. Soc. London, Ser. A* **165**, 372 (1938)
27. Koskinen, P.; Malola, S.; Hakkinen, H. *Phys. Rev. Lett.* 2008, 101, 115502.
28. Zheng, F.; Zhou, G.; Liu, Z.; Wu, J.; Duan, W.; Gu, B.-L.; Zhang, S.B. *Phys. Rev. B* 2008, 78, 205415.
29. Huang, S.-P. ; Xu, H.; Bello, I.; Zhang, R. Q. *Chem. Eur. J.* 2010, 16(44), 13072.
30. Makov, G. and Payne, M. C., *Phys. Rev. B.* 1995, 51, 4014.
31. Gunnarsson, O. *J.Phys.F: Metal Phys.*1976, 6, 587.

5 Three-dimensional carbon and BN foam

5.1 Introduction

Recently, a new class of graphene-based nanostructures has been proposed, namely, the graphene tri-wing nanoribbons in which three GNRs are interconnected by sp^3 carbon atoms [1]. It turns out that the TWG nanoribbons entail much greater flexural rigidity (defined as the force couple required to bend a beam-like structure to a unit curvature) than a flat GNR due to the robust “Y”-shaped beam structure (motivated from building construction) [1]. Moreover, the TWG nanoribbons can be viewed as a building block for a class of open-network (low-density) carbon foams which contain mixed sp^2 - sp^3 carbon bonds. Since the design of carbon foams by Karfunkel et al. in 1992 [2] and Balaban et al. in 1994 [3], this class of porous carbon foams has received increasing attention due to their high structural stability at low mass density [4-7]. For example, the large surface area of carbon foams can be exploited as hydrogen storage [8]. In this chapter, we present a material design of another tri-wing graphene (TWG) nanoribbon and a tri-wing BN (TWBN) nanoribbon, which can serve as a structural motif for constructing a new class of open-network carbon and BN foams, respectively. Unlike previously reported carbon foam which contains a large fraction of sp^3 carbon-carbon bonds, the newly designed honeycomb carbon foam contains little sp^3 carbon-carbon bonds. We also present a material design of medium-density open-network of carbon foam, which contain only sp^2 carbon-carbon bonds. Electronic properties of the TWG and TWBN nanoribbons are computed and the cohesive energies of the new carbon and BN foams are compared with those of bulk carbon and BN solids, respectively. In addition, their thermal stability and elastic properties are investigated.

5.2 Computational details

DFT calculations are carried out using Dmol3 package. The GGA in the PBE form and DNP basis set are chosen for the spin-unrestricted DFT computation. The real-space global cutoff radius is set to be 4.1 Å. A rectangular supercell with dimension $35 \times b \times 35$ Å³ is selected for TWGs, and the Brillouin zone is sampled by using $1 \times 10 \times 1$ k points in the Monkhorst-Pack scheme. After geometric optimization, $b = 4.90$ and 5.04 Å are obtained for the TWG and TWBN nanoribbons, respectively. For structural relaxation of the carbon and BN foams, a rhomboid supercell is set up and the Brillouin zone is sampled by using $3 \times 3 \times 5$ k points in the Monkhorst-Pack scheme. After geometric optimization, the forces on all atoms are less than 0.0002 Ha/Å.

5.3 Results and discussions

The newly designed TWG nanoribbon is composed of three ZGNRs. In the initial configuration, a linear carbon chain joins the three ZGNRs together via the sp^2 carbon-carbon bonds at their zigzag edges (Fig. 1(a)). The dangling bonds on the outer edges of the three wings are passivated by hydrogen atoms. Here, we denote this carbon nanostructure as the carbon-centered TWG (cc-TWG) nanoribbon in which all carbon-carbon bonds are sp^2 , in contrast to the TWG nanoribbon designed in Ref. 30. The number of zigzag chains in each ZGNR wing is denoted by n , m , l , respectively. In Fig. 1(a), a TWG nanoribbon with $n = m = l = 4$ is displayed and thus it has C_{3v} symmetry. However, we find that this TWG nanoribbon structure is energetically less favorable than the structure shown in Fig. 1(b), in which every other two nearest-neighbor carbon atoms along the center line are bonded with each other to form a dimer

so that only the center carbon atoms have the sp^3 hybridization. The structure shown in Fig. 1(b) is lower in energy by 1.51 eV per supercell than that shown in Fig. 1(a). Nevertheless, the C_{3v} symmetry is still preserved after the formation of dimers for all center carbon atoms. In the relaxed structure, the outer edges of the three wings exhibit magnetic edge states which are ferromagnetically coupled as demonstrated by the spin density distribution (Fig.1(c)). Figure 1(d) displayed the computed electronic band structure which suggests that the TWG nanoribbon is a metal with spin polarization. If the center carbon atoms are replaced by boron or nitrogen atoms, we found that the boron or nitrogen atoms form a uniform linear chain (see Fig.1(e) and (f)) without showing the formation of dimers as in the case of carbon atoms.

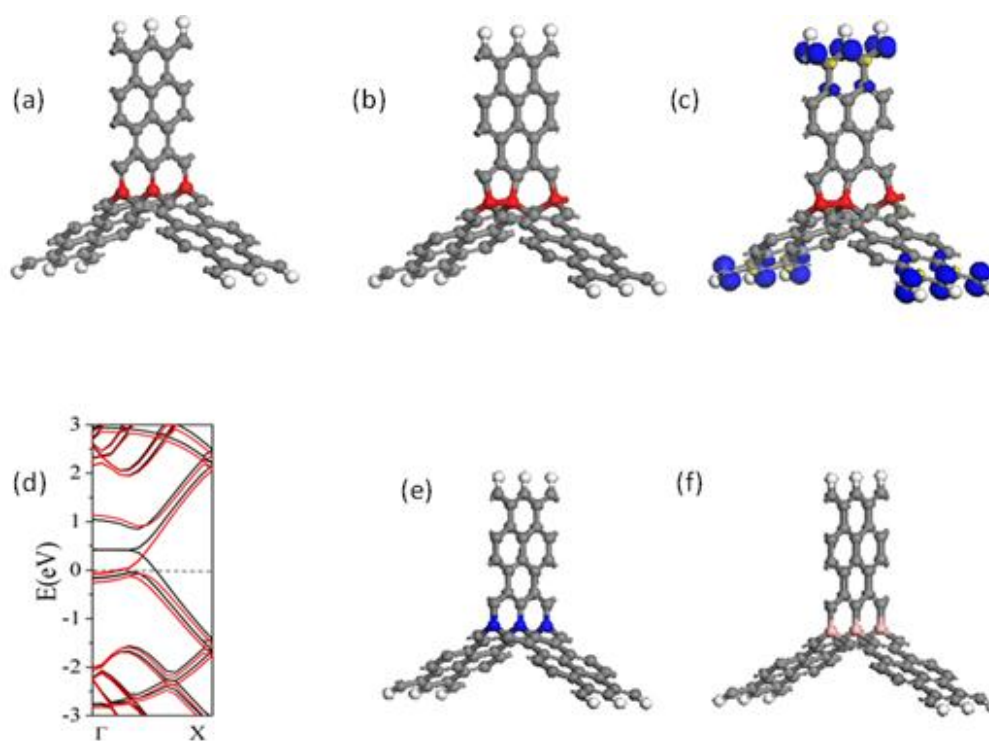


Figure 1 Geometric structures of cc-TWG nanoribbon (a) before and (b) after the formation of carbon-carbon dimers along the center carbon chain; (c) the spin-density distribution and (d) band structure of the cc-TWG nanoribbon. (e) and (f) display structures of nitrogen-centered and boron-centered structures, respectively.

boron-centered TWG nanoribbon, respectively. Grey, white, blue, pink balls denote carbon, hydrogen, nitrogen and boron atoms. In (c), blue and yellow represent spin-up and spin-down spin state, respectively, and the range of iso-value spin density is $[-0.03, 0.03]$. In (d), black lines represent the spin-up channel and red lines represent the spin-down channel; the black dashed line denotes the Fermi level.

For the TWBN nanoribbons, two types can be constructed, namely, B-center (bc-TWBN) and N-center (nc-TWBN) nanoribbons, as shown in Fig. 2(a) and (b). Unlike the TWG nanoribbon, the center N atoms or B atoms do not form periodic dimers in the TWBN nanoribbons. The calculated band structures suggest that both bc-TWBN and nc-TWBN nanoribbons are semiconducting with a band gap of 0.75 and 0.7eV respectively, and that both TWBN nanoribbons exhibit no spin polarization. The highest occupied state (HOS) and lowest unoccupied state (LUS) at the gamma (Γ) point for both TWBN nanoribbons are also displayed in Fig. 2. For the bc-TWBN nanoribbon, the LUS is mainly contributed by the boron chain in the center, while HOS is mainly contributed by those nitrogen atoms bonded with center boron atoms. For nc-TWBN nanoribbons, however, the HOS is contributed mainly by the center nitrogen atoms while LUS is mainly contributed by adjacent boron atoms.

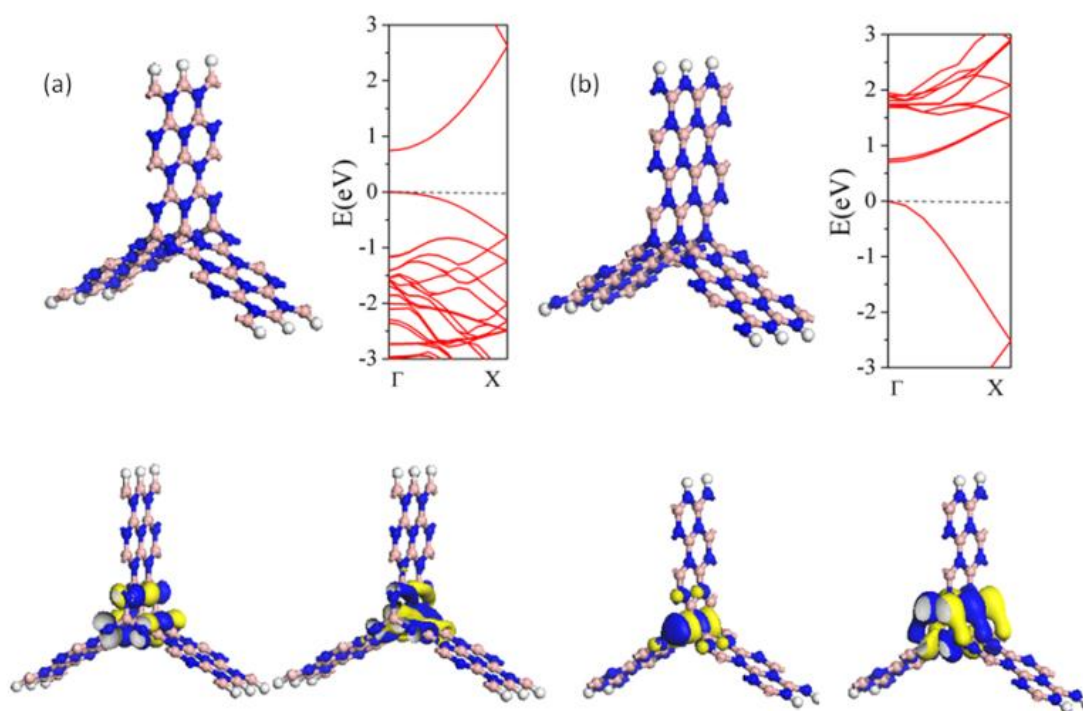


Figure 2 Geometric structures, band structures, HOS and LUS of (a) bc-TWBN and (b) nc-TWBN nanoribbons.

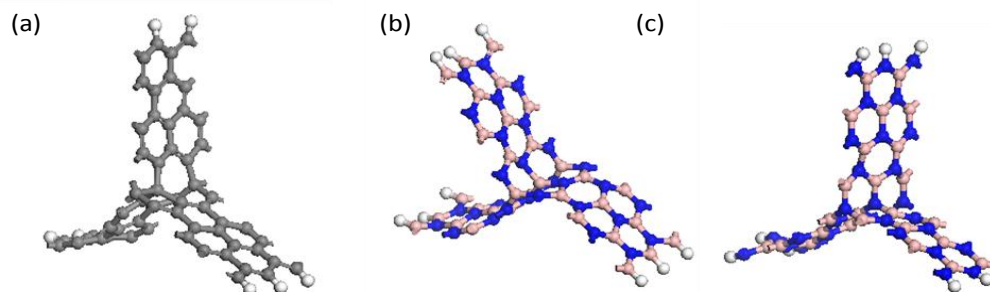


Figure 3 A snapshot of the equilibrium structure of (a) cc-TWG, (b) bc-TWBN, and (c) nc-TWBN nanoribbons at 1000 K and at the end of 5 ps quantum MD simulation.

To confirm that both TWG and TWBN nanoribbons are thermally stable, we perform independent Born-Oppenheimer molecular dynamics (BOMD) simulations of cc-TWG, bc-TWBN and nc-TWBN nanoribbons, respectively. Specifically, the constant-temperature and constant-volume (NVT) ensemble is chosen and the Nosé-Hoover chain method [9] is used for temperature control (temperature is fixed at 1000 K). The Nosé Q ratio is set 2.0 and the Nosé chain length is 2. A snapshot of the equilibrium structure at the end of 5 ps BOMD simulation for each nanostructure is shown in Fig. 3(a-c), respectively. It can be seen that the TWG and nc-TWBN nanoribbons can preserve their overall structure even at 1000 K. For the bc-TWBN nanoribbon, however, one wing is slightly bended towards another wing. In general, the TWG nanoribbon entails much greater flexural rigidity than a flat GNR [1].

As pointed out above, the TWG nanoribbon can be viewed as a building unit for the construction of low-density porous carbon foams. This first type of carbon foam constructed is a honeycomb network similar to hinged polyacetylene carbon proposed in Ref. 32, as shown in Fig. 4(a), and hereafter we call it the type-I carbon foam. At each junction, three GNRs form a 120° inter-plane angle with respect to one another, and the joint is a linear chain of carbon dimers where each carbon atom in the dimer is in sp^3 hybridization. We calculated the frequency and no imaginary frequency is found. We use the number of zigzag chains n in each wing to characterize the carbon foam ($n = 4$ in Fig. 4). The calculated mass density of the honeycomb carbon foam is 0.80 g/cm^3 , which is less than a quarter of the measured mass density (3.54 g/cm^3) of diamond. The band structure for the $n = 4$ carbon foam is shown in Fig. 4(a), which indicates that the type-I carbon foam is metallic. The honeycomb BN foam ($n = 4$, Fig. 4(b)) has identical structure as the type-I carbon foam. Calculated band structure suggests that the honeycomb BN foam is a half metal—the band gap is zero for one spin channel and 0.37 eV for the other.

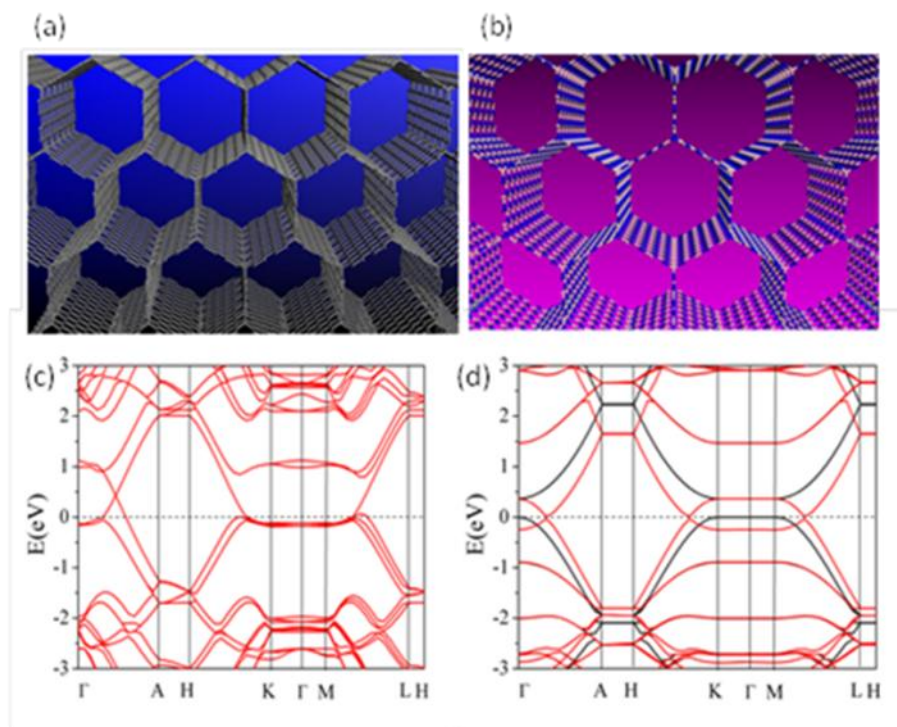


Figure 4 Geometric structures and calculated band structures of (a) the honeycomb carbon foam and (b) the honeycomb BN foam. $\Gamma(0.0, 0.0, 0.0)$, $A(0.0, 0.0, 0.5)$, $H(-0.333, 0.667, 0.5)$, $K(-0.333, 0.667, 0.0)$, $M(0.0, 0.5, 0.0)$, and $L(0, 0.5, 0.5)$ refer to special symmetry points in the first Brillouin zone.

Based on DFT calculations, we find the cohesive energy of the ($n = 4$) honeycomb carbon foam (with 52 atoms per unit cell) is 7.19 eV/atom, slightly less than that of graphite by 0.12 eV/atom but nearly the same as that of diamond. Hence, we expect that this low-density carbon foam can be a stable polymorph of carbon and may be fabricated through fusion of graphene nanoribbons. For the honeycomb BN foam ($n = 4$), the calculated cohesive energy is 6.93 eV, which is only 0.13 eV/atom less than that of 3D h-BN, 0.11 eV/atom less than c-BN, and almost equal to that of a (9,0) single-walled BN nanotube. Hence, the low-density honeycomb BN foam can be a stable polymorph of boron nitride as well. The calculated mass density of the

honeycomb BN foam is 0.78 g/cm^3 , about a third of h-BN mass density (2.22 g/cm^3) and less than a quarter of c-BN mass density (3.45 g/cm^3). Both type-I carbon and BN foams have a fairly large surface area per mass, 2859 and $2889 \text{ m}^2/\text{g}$, respectively. They also have a huge surface area per volume, 2.29×10^9 and $2.28 \times 10^9 \text{ m}^2/\text{m}^3$, much larger than internal surface area of common carbon foam, $5,000 \sim 50,000 \text{ m}^2/\text{m}^3$. [10]

In addition, we present a material design of a medium-density carbon foam, namely, the triangular (or type-II) carbon foam. As shown in Fig. 5(a), the type-II foam exhibits a triangular network where at each junction six graphene nanoribbons are joined by a stack of hexagon rings. As such, the mass density of type-II carbon foam is 1.67 g/cm^3 , about twice higher than that of type-I carbon foam. Also, no structural reconstruction is found at each joint upon structural relaxation. Hence, all carbon-carbon bonds in the type-II carbon foam are in sp^2 hybridization. As shown in Fig. 5(a), the calculated band structure suggests that the type-II foam carbon foam is still metallic. The type-II BN foam as shown in Fig. 5(b) has identical geometric structure as the type-II carbon foam, and the mass density of type-II BN foam is 1.63 g/cm^3 , about twice of that of type-I BN foam. Unlike the type-I BN foam, the band-structure calculation suggests that the type-II BN foam is a semiconductor with a band gap of 1.35 eV .

According to DFT calculations, the cohesive energy of the type-II carbon foam is 7.08 eV/atom , about 0.11 eV/atom less than that of type-I carbon foam. Thus, this medium-density polymorph of carbon is energetically less stable than the low-density honeycomb carbon foam, but still can be a stable structure in the medium-density range. For the type-II BN foam, the calculated cohesive energy is 6.93 eV/atom , nearly the same as that of type-I BN foam. Hence, the medium-density type-II BN foam can be a stable polymorph of BN as well. The calculated surface area per mass of type-II carbon and BN foam are 2513 and $2530 \text{ m}^2/\text{g}$, respectively,

slightly less than that of type-I carbon and BN foam. However, they have even larger surface area per volume, 5.35×10^9 and 5.30×10^9 m^2/m^3 , which are more than twice as that of type-II foams.

Because both low-density and medium-density carbon and BN foams have appreciably large surface area, we calculate the adsorption curves of N_2 at 298 K using the Sorption Package [11]. As shown in Fig. 6, the number of adsorbed N_2 per supercell increases with increasing the pressure of N_2 . It seems that the type-II foams have higher adsorption rates than the type-I foams. If the surface coverage is estimated based on the number of adsorbed N_2 molecules over the number of atoms of the foam, we find that the surface coverage of type-I carbon and BN foam, type-II carbon and BN foam are about 0.013, 0.018, 0.028, 0.031, respectively, at 100 kPa (ambient condition).

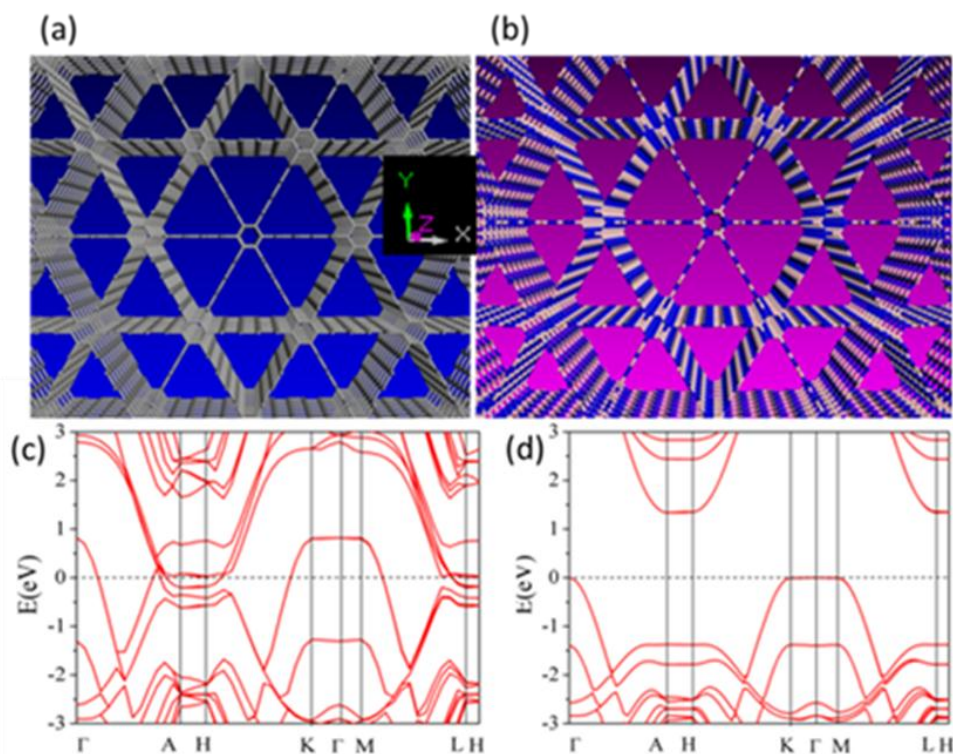


Figure 5. Geometric structures and electronic band structures of (a) the type-II carbon foam and (b) type-II BN foam. $\Gamma(0.0, 0.0, 0.0)$, $A(0.0, 0.0, 0.5)$, $H(-0.333, 0.667, 0.5)$, $K(-0.333, 0.667, 0.0)$, $M(0.0, 0.5, 0.0)$, and $L(0, 0.5, 0.5)$ refer to special symmetry points in the first Brillouin zone.

Lastly, we calculate the Young's modulus E_x , E_z in the X and Z direction of the carbon and BN foams (see Fig. 4, 5) and their bulk modulus by using CASTEP package [42]. As shown in Table I, we found type-II foams have much larger Young's modulus and bulk modulus than type-I foams: the Young's modulus E_x of every type-II foam is higher than that of steel (~ 200 GPa) but significantly less than that of diamond (~ 1220 GPa), and their bulk modulus are also larger than that of steel (160GPa) but smaller than that of diamond (460GPa).

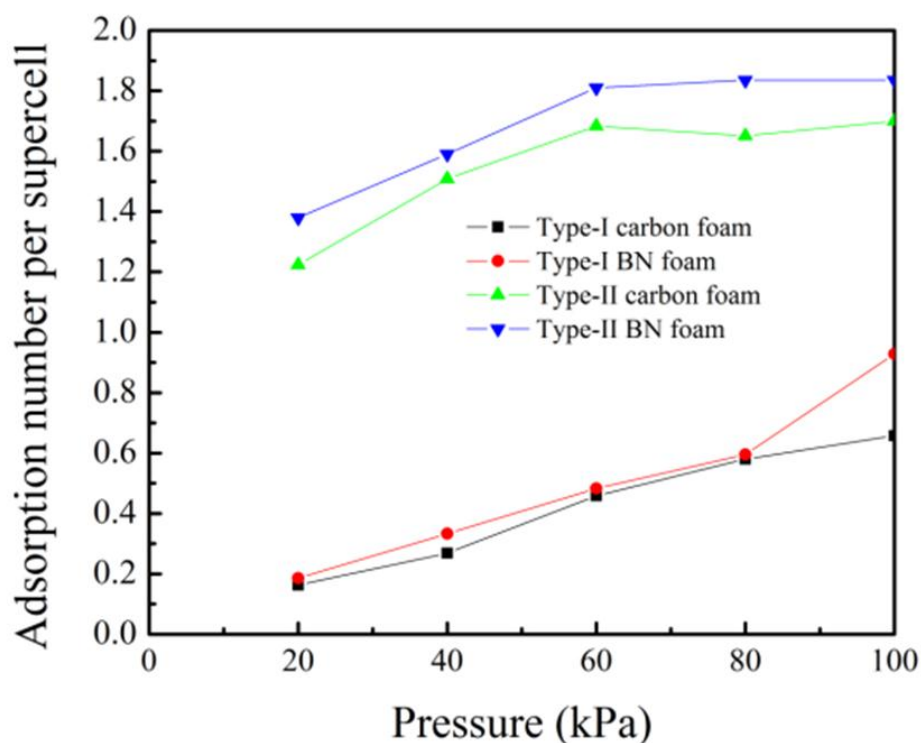


Figure 6. Calculated adsorption curves of N₂ for the carbon and BN foams at 298 K.

Foam	Type-I carbon	Type-I BN	Type-II carbon	Type-II BN
E _x (GPa)	30	35	288	232
E _z (GPa)	339	255	641	502
B(GPa)	72	64	202	145

Table I. Calculated Young's modulus and bulk modulus of the carbon and BN foams.

5.4 Conclusions

In summary, based on density-functional calculations and quantum MD simulations, we demonstrate high stability of a new carbon or BN nanostructure, i.e., the TWG nanoribbon in which three ZGNR wings are connected by a carbon-dimer chain and the TWBN nanoribbon with either boron or nitrogen as center. The TWG nanoribbon is predicted to be metallic while the TWBN nanoribbons are semiconducting. Their structures remain robust even at high temperature 1000 K. More importantly, the TWG nanoribbon and TWBN can serve as a building unit to construct low-density polymorph of carbon and BN, namely, the honeycomb (or type-I) carbon and BN foam, respectively. Both carbon and BN foams have cohesive energy very close to their high-density polymorphs, e.g. diamond and c-BN, respectively. Hence, from the energetic point of view, these low-density polymorphs of carbon and BN can be quite stable. In addition, we present a design of medium-density (type-II) carbon and BN foams which exhibit triangular network structures. Their cohesive energy and surface area is slightly less than that of

type-I foams while their Young's modulus is much higher than that of type-II foams. For carbon, both type-I and II foams are predicted to be metallic while type-I BN foam is predicted to be half metallic and type-II BN foam is semiconducting. Note that the honeycomb and triangular foams presented here are ideal structures with uniform density. In real-world fabrication, the foams can be a mixture of various open networks with different lengths of walls. Nevertheless, the inherent large surface area, low mass-density, and structural integrity are hallmark of carbon and BN foams that can be exploited for various applications such as gas storages and light-weight/hard materials. Moreover, if confirmed by experiments, these low-density and medium-density foams would enrich polymorphic family of carbon and BN.

5.5 References

- 1.L.Zhu et al. *Nano. Lett.* **10(2)**, 494 (2009)
- 2.H. R.Karfunkel and T. Dressler, *J. Am. Chem. Soc.* **114**, 2285 (1992).
- 3.A. T.Balaban, D. J.Klein, C.A.Folden, *Chem. Phys. Lett.* **217**, 266 (1994).
- 4.N.Park, J. Ihm, *Phys. Rev. B* **62**, 7614 (2000).
- 5.R. H. Baughman and D. S. Galvao, *Nature* **365**, 735-737(1993).
- 6F. J.Ribeiro, P.Tangney, S. G.Louie, M.L. Cohen *Phys. Rev. B.* **722**, 214109 (2005).
- 7.Kuc A., G.Seifert, *Phys. Rev. B* **74**, 214104 (2006).
- 8.N.Park, S.Hong, G.Kim, S.-H. Jhi, *J.Am.Chem.Soc.* **129**, 8999 (2007).
- 9G. J.Martyna, M. L. Klein, M. E.Tuckerman, *J. Chem. Phys.* **97**, 2635 (1992).
- 10.Q.Yu, A. G.Straatman, B. E.Thompson, *Applied Thermal Engineering* **26**, 131–143 (2006).
- 11.Sorption is a software module in Materials Studio, available from Accelrys Software Inc.

6 Transition-Metal-Molecular Sandwich Nanowires as Magnetic On/Off Switch

6.1 Introduction

Ferrocene is a sandwich-like molecule with the formula $\text{Fe}(\text{C}_5\text{H}_5)_2$ which is composed of two parallel cyclopentadienyl (Cp) rings and a central Fe atom between the two Cp rings. Since the discovery of ferrocene compound (FeCp_2)[1], ferrocene-like molecular complexes[2-4] (where the central Fe atom is replaced by another metal atom) and one-dimensional (1D) transition-metal-molecular sandwich nanowires (SWNs) have attracted considerable attention due to their intriguing magnetic properties and potential applications in electron transport and spin filtering[5-24]. Besides successful synthesis of various ferrocene-like dicyclopentadienyl complexes such as VCp_2 , CrCp_2 , MnCp_2 , CoCp_2 , NiCp_2 , and ZnCp_2 , longer transition-metal molecular complexes, *e.g.*, the seven-decker $\text{V}_n(\text{Bz})_m$ sandwich cluster and eighteen-decker $\text{Eu}_n(\text{C}_8\text{H}_8)_m$ nanorod, have been produced in the laboratory[2-4]. Among multidecker transition-metal-benzene (Bz) sandwich complexes, the Sc-, Ti-, and V- C_6H_6 (Bz) complexes have been reported to be the most stable[3-4]. Previous first-principles calculation studies have also predicted that the transition-metal-ferrocene SWN $[\text{Fe}(\text{Cp})]_\infty$ and transition-metal-benzene SWN $[\text{Mn}(\text{Bz})]_\infty$ may possess half metallicity (*i.e.*, being conducting in one spin channel while insulating in the other spin channel), whereas the SWN $[\text{V}(\text{Bz})]_\infty$ is a quasi-half-metallic ferromagnet[7]. Koleini *et al.* proposed a design of nanoscale spin filter composed of a transition-metal-benzene cluster V_nBz_m and two single-walled carbon nanotubes (or graphene nanoribbons) as electrodes. A high transmission spin polarization ranging from 73% to 99% is observed, independent of specific structure or orientation of the cluster V_nBz_m [9]. Atodiresei *et al.* revealed that a change of the direction of magnetization, from in-plane to axial, can be achieved by either charging or discharging a transition-metal-molecular complex $\text{Eu}_2(\text{C}_8\text{H}_8)_3$ [10].

Yang and coworkers studied ferromagnetic properties of the first-row transition metal-ferrocene SWNs and found that one valence electron can transfer from the transition metal to the ferrocene so that the sandwich structure entails alternatively charge on the ferrocene and transition metal[12]. Previous first-principles calculations have also shown that both $[\text{Cr}(\text{Bz})]_{\infty}$ and $[\text{Mn}(\text{Cp})]_{\infty}$ SWNs are nonmagnetic[7-12]. In this letter, we show first-principles calculation evidence of charge-induced non-magnetic to ferromagnetic (FM) transition in both the $[\text{Cr}(\text{Bz})]_{\infty}$ and $[\text{Mn}(\text{Cp})]_{\infty}$ SWNs. More specifically, upon positive charge injection, both non-magnetic SWNs $[\text{Cr}(\text{Bz})]_{\infty}$ and $[\text{Mn}(\text{Cp})]_{\infty}$ become FM half metals, whereas upon negative charge injection both SWNs become FM metals. This charge-controlled magnetic transformation for both SWNs may be exploited as magnetic on/off switches.

6.2 Computational details

The first-principles calculations are carried out using the Vienn Ab initio Simulation Package (VASP)[25-27]. The projector augmented wave (PAW) potentials for the core and GGA in the PBE form[28] for the exchange-correlation functional are used. For charged systems, a neutralizing background charge is assumed automatically. For geometric optimization, a tetrahedral supercell with spatial dimension $16 \times 16 \times 2c \text{ \AA}^3$ is adopted, where c is the length of the unit cell along the axial direction. The nearest distance between a SWN and its periodic image is $> 10 \text{ \AA}$. The kinetic energy cutoff is set to be 500 eV. For electronic band-structure calculation, the Brillouin zone is sampled by using $1 \times 1 \times 15$ k points in the Monkhorst-pack scheme[29].

6.3 Results and discussions

In Table 1 we present the calculated magnetic moment per supercell for $[\text{Mt}(\text{Cp})]_{\infty}$ and $[\text{Mt}(\text{Bz})]_{\infty}$ SWNs (Mt = early transition metals from Sc to Fe in the first row of periodic table) in

the charge-neutral state, and subjected to either $1e$ hole or $-1e$ electron injection per supercell, respectively. The computed spin-charge density distribution and electronic band structures are shown in Fig. 1 and in Fig. 2. Note that for the charge-neutral state, our calculation results are in excellent agreement with those from previous studies[7,12]. Note also that we have computed magnetic moments for other $[\text{Mt}(\text{Cp})]_{\infty}$ and $[\text{Mt}(\text{Bz})]_{\infty}$ SWNs (Mt = late transition metals from Co to Zn in the first row, or the second-row early transition metal Nb, Mo, Tc, Ru). We find, however, that these SWNs are either unstable (i.e., the binding energy per metal atom is less than 1.0 eV), or exhibit zero magnetic moments (independent of their charge state; see Fig. 2).

Table I Computed magnetic moments (μ_{B}) per supercell (containing 2 unit cells) for $[\text{Mt}(\text{Cp})]_{\infty}$ (Mt = first-row transition metals) and $[\text{Mt}(\text{Bz})]_{\infty}$ (Mt=Sc, Ti, V, Cr, Mn, Fe) SWNs in the charge neutral state, or subjected to either $1e$ hole injection or $-1e$ electron injection per supercell.

M(μ_{B})	Mt	Sc	Ti	V	Cr	Mn	Fe
Bz	0e	0.0	0(AF)	1.9	0.0	2.2	4.0
	1e	0.0	0(AF)	2.9	1.0	1.2	3.2
	-1e	0.0	0(AF)	1.8	0.0	2.5	4.0
Cp	0e	0.0	1.5	3.4	2.0	0.0	2.0
	1e	0.0	0.8	3.4	3.0	1.0	1.7
	-1e	0.0	1.7	3.4	1.7	0.2	2.3

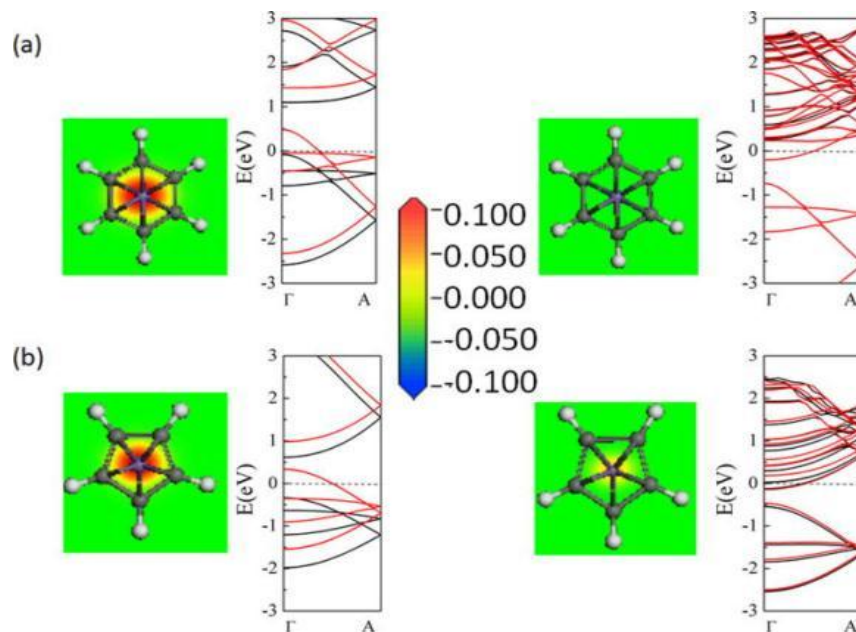
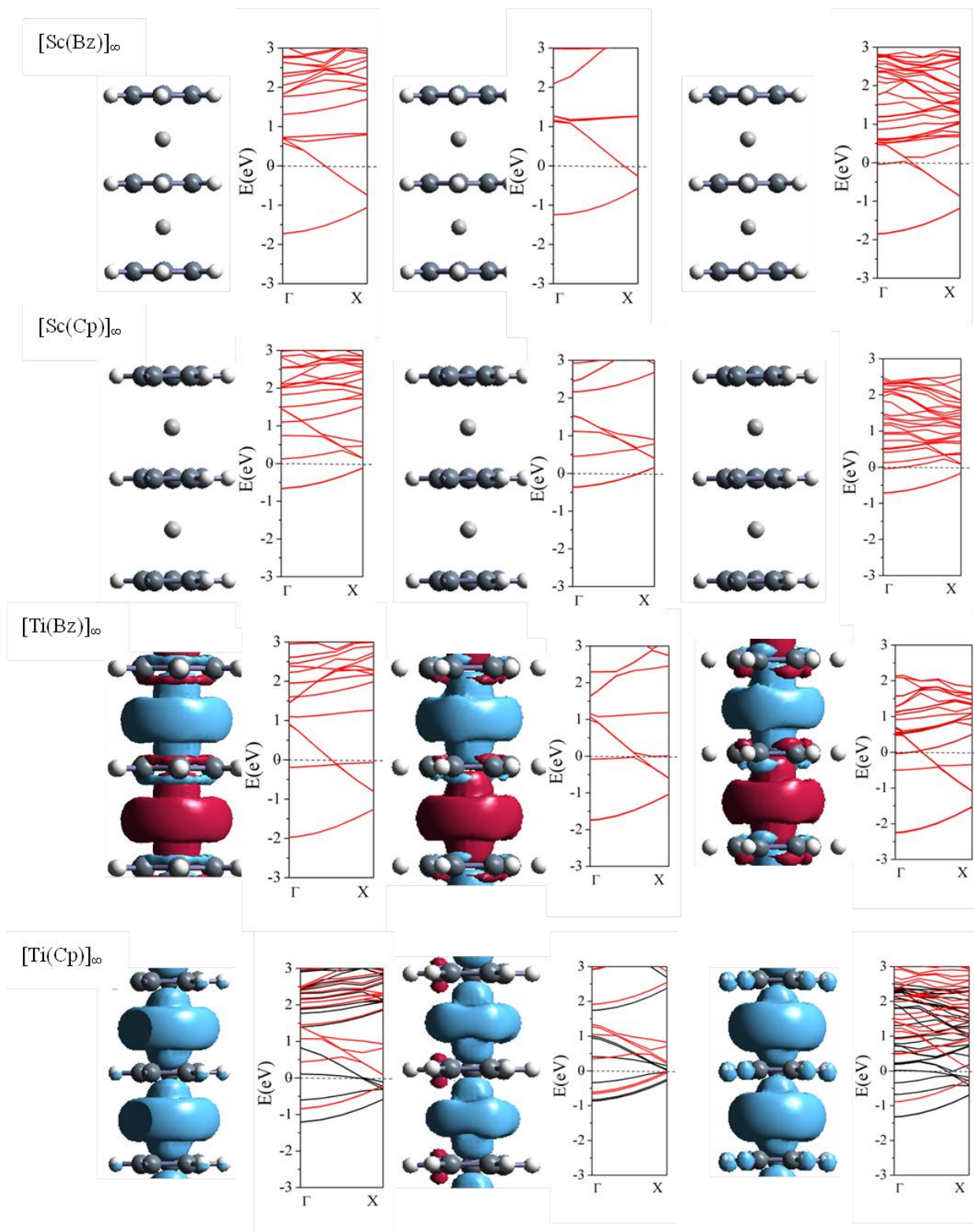


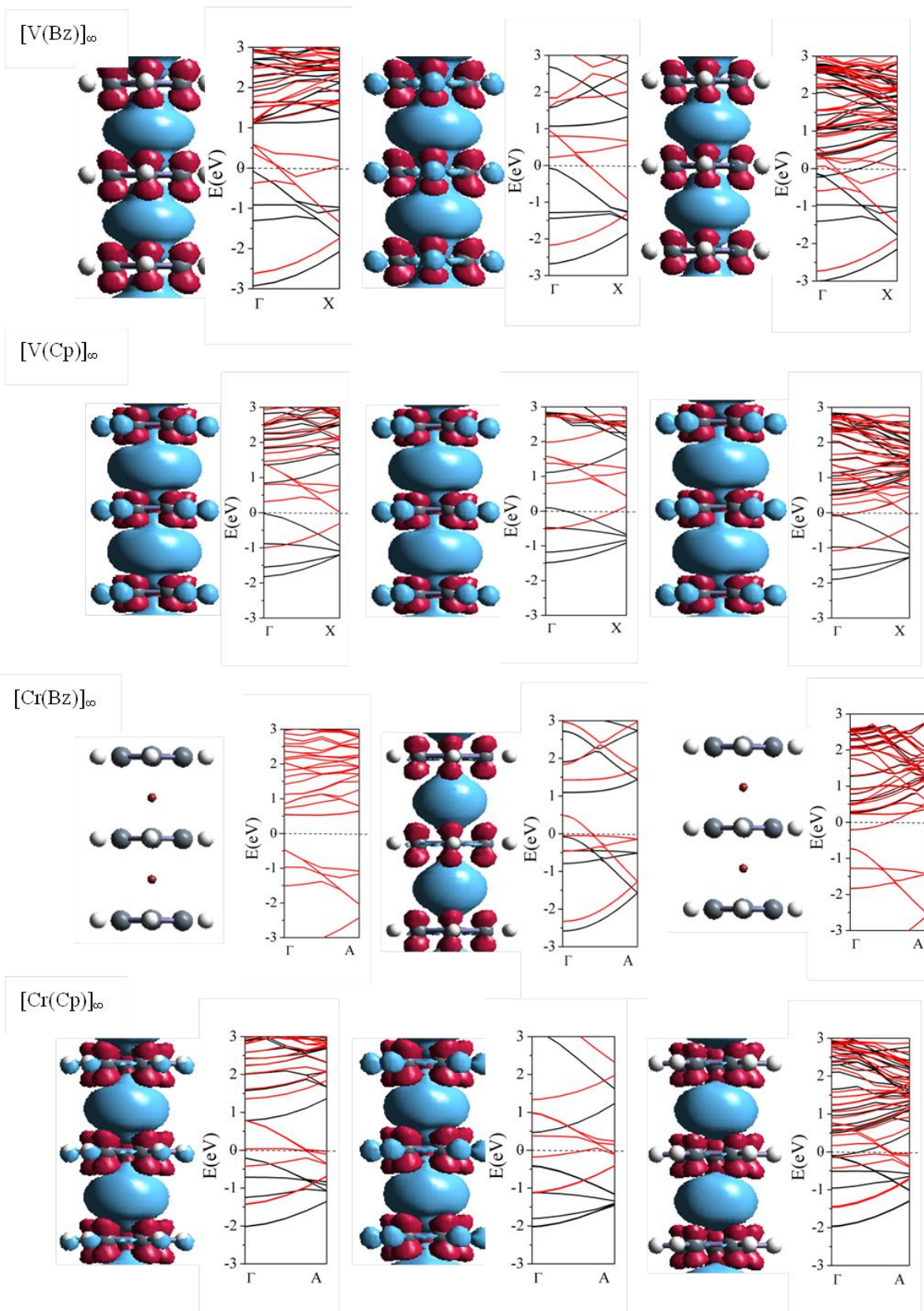
Figure 1 Computed spin-charge density distribution and electronic band structures of (a) $[\text{Cr}(\text{Bz})]_{\infty}$ and (b) $[\text{Mn}(\text{Cp})]_{\infty}$ SWNs subjected to charge injection of $1e$ per supercell (left panel) and $-1e$ per supercell (right panel). For band structures, red and black lines denote α and β spin channels, respectively. The Fermi level is marked by the dashed line. Grey and white spheres represent carbon and hydrogen atoms.

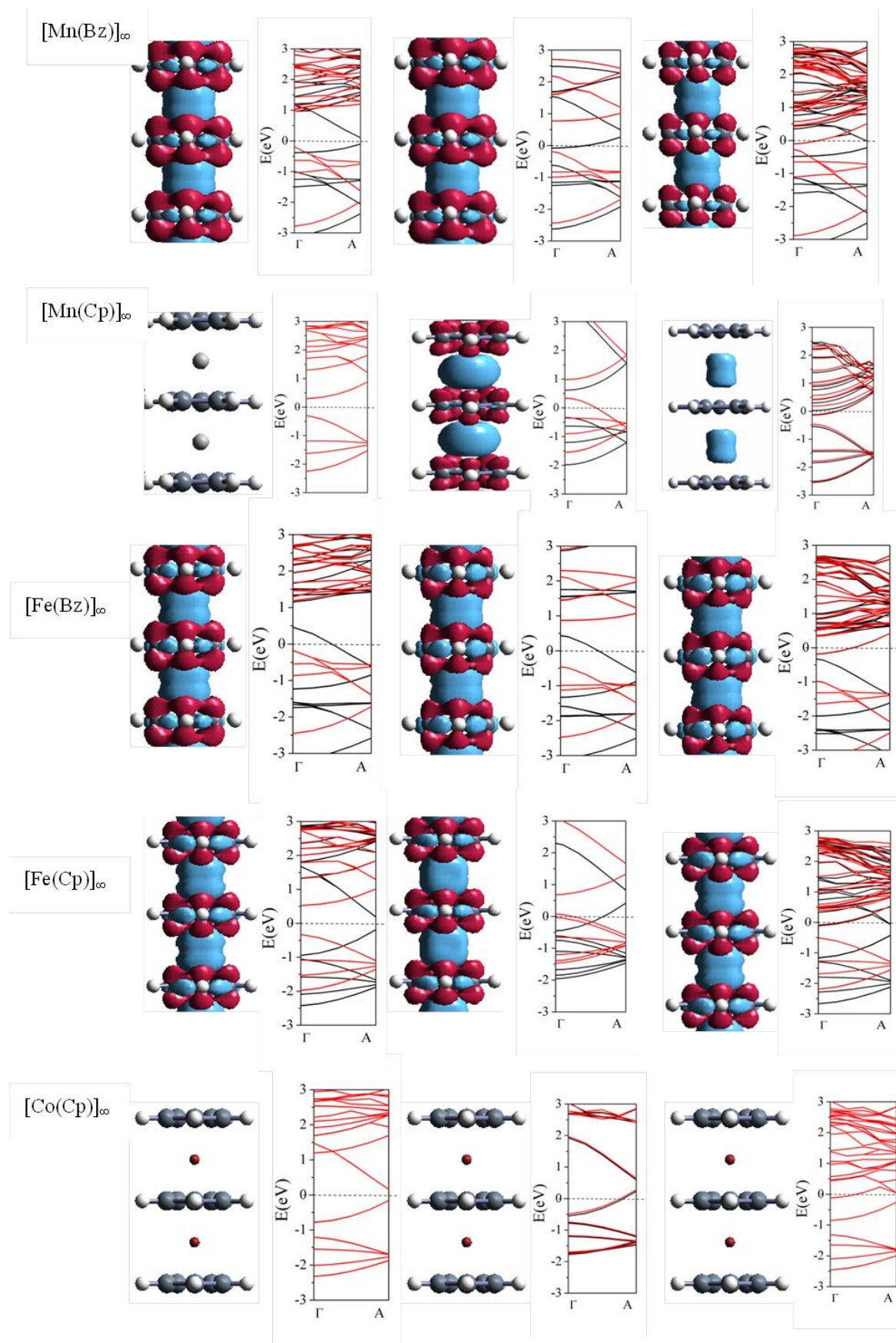
As shown in Table 1, in the charge neutral state, only four SWNs are non-magnetic, namely, $[\text{Sc}(\text{Bz})]_{\infty}$, $[\text{Sc}(\text{Cp})]_{\infty}$, $[\text{Cr}(\text{Bz})]_{\infty}$ and $[\text{Mn}(\text{Cp})]_{\infty}$. Upon charge injection, however, only $[\text{Cr}(\text{Bz})]_{\infty}$ and $[\text{Mn}(\text{Cp})]_{\infty}$ SWNs undergo the non-magnetic to FM transition, similar to the behavior found in the boron nitride sheet [30]. Figure 1 displays the computed spin-density distribution for the $[\text{Cr}(\text{Bz})]_{\infty}$ and $[\text{Mn}(\text{Cp})]_{\infty}$ SWNs in the charge-neutral state, or subjected to either $1e$ hole injection or $-1e$ electron injection per supercell. Notably, the hole injection can induce substantially stronger magnetization on the transition-metal atoms in both $[\text{Cr}(\text{Bz})]_{\infty}$ and $[\text{Mn}(\text{Cp})]_{\infty}$ SWNs, bringing out a relatively large magnetic moment of $1\mu_{\text{B}}$ per supercell (see Table I). In addition, a partial magnetic moment in the opposite spin direction is also induced on

either Bz or Cp rings. On the other hand, upon the electron injection, the $[\text{Cr}(\text{Bz})]_\infty$ and $[\text{Mn}(\text{Cp})]_\infty$ SWNs exhibit different magnetic behavior as shown in Fig. 1. The $[\text{Mn}(\text{Cp})]_\infty$ SWN attains a relatively smaller magnetic moment of $\sim 0.2\mu_B$ per supercell (under a charge injection of $-1e$ per supercell), while the $[\text{Cr}(\text{Bz})]_\infty$ SWN remains to be non-magnetic. Moreover, the computed band structures suggest that upon the hole injection ($1e$ per supercell), both $[\text{Cr}(\text{Bz})]_\infty$ and $[\text{Mn}(\text{Cp})]_\infty$ SWNs become half metallic, whereas upon electron injection ($-1e$ per supercell) both SWNs become metallic.

According to the Stoner criterion[31], a transition from the paramagnetic to FM state would occur if the condition $I\rho(E_F) > 1$ is met, where I is the Stoner parameter and $\rho(E_F)$ is the density of states at the Fermi level for the system at the paramagnetic state. To apply the Stoner criterion to the present SWN systems, we have computed the projected density of states (PDOS) on Cr in $[\text{Cr}(\text{Bz})]_\infty$ and on Mn in $[\text{Mn}(\text{Cp})]_\infty$, at the charge-neutral and two charge-injection states, respectively, as shown in Fig. 3(a) and (b). At the charge-neutral state, we find $\rho(E_F) = 0$ on both Cr and Mn atoms, consistent with the conclusion that both SWNs are non-magnetic.^{7,12} Upon the positive charge (hole) injection, the Fermi level is shifted upward in general. However, for the $[\text{Cr}(\text{Bz})]_\infty$ SWN, $\rho(E_F)$ on Cr remains nearly zero so that the SWN is still non-magnetic. In contrast, $\rho(E_F)$ on Mn increases from 0 to $0.9/\text{eV}$ (see right panel in Fig. 3(b)). Hence, when the value of $I\rho(E_F)$ becomes greater than 1, $[\text{Mn}(\text{Cp})]_\infty$ would become FM. On the other hand, upon the negative charge (electron) injection, the Fermi level is shifted downward; $\rho(E_F)$ on Cr and Mn increase to $1.7/\text{eV}$ and $2.9/\text{eV}$, respectively. Hence, both SWNs become spin-polarized. Note that $\rho_{\text{Mn}}(E_F) = 2.9/\text{eV}$ (in $-1e$ charge state) is much higher than $\rho_{\text{Mn}}(E_F) = 0.9/\text{eV}$ (in $1e$ charge state), which explains why the former charge state induces a relatively larger magnetic moment ($1.0\mu_B$ per supercell) than the latter ($0.2\mu_B$ per supercell).







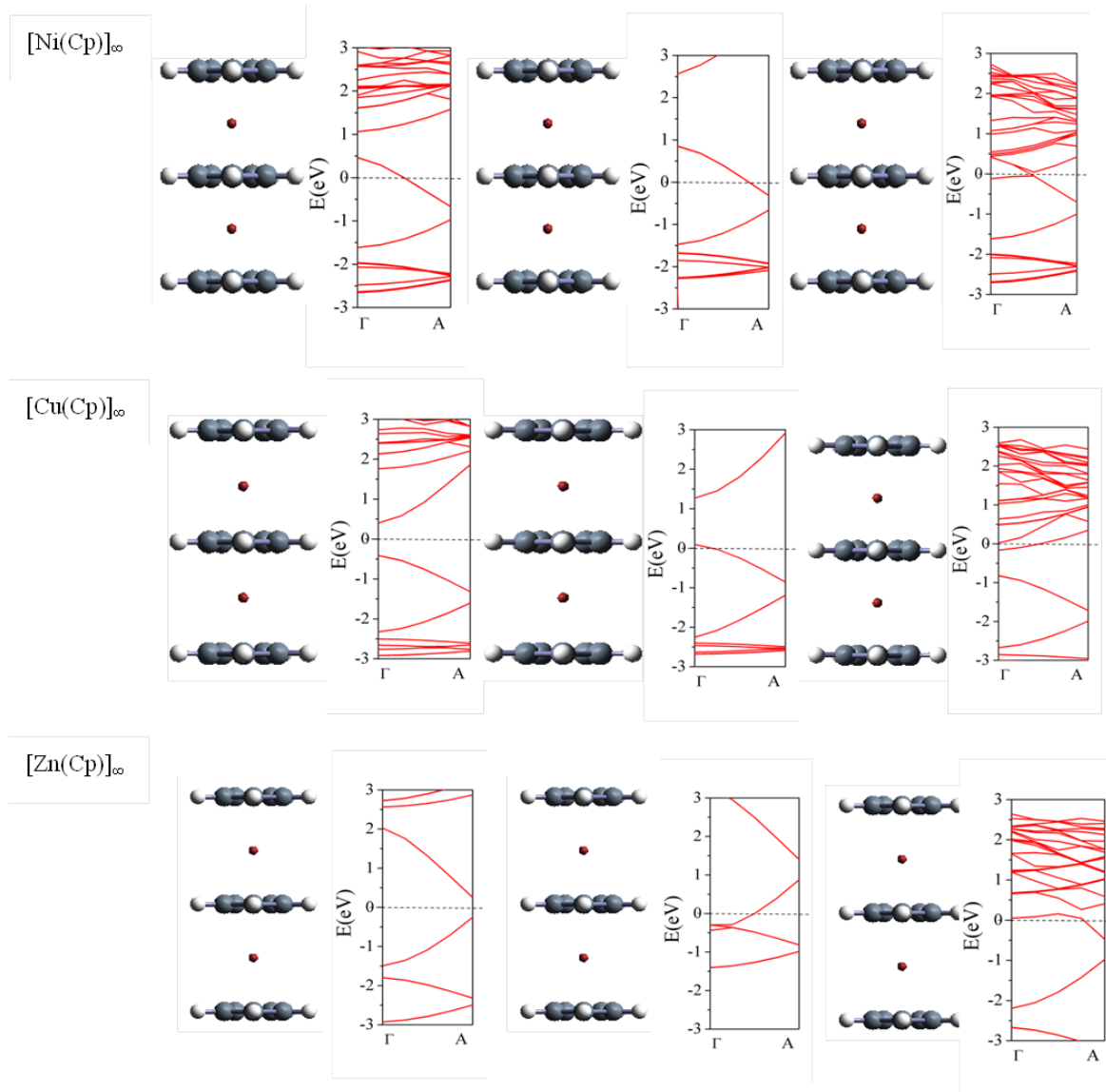


Figure 2 Computed spin density distribution and electronic band structures of SWNs (listed in Table 1) at neutral state (left panel), and at charge injection of $1e$ per supercell (middle panel) and $-1e$ per supercell (right panel), respectively. For spin density distribution, blue and red represent α and β spin, respectively; the range of the isovalues of spin density is $0.08e/\text{\AA}^3$. For band structures, red and black lines denote α and β spin channels, respectively. Grey and white spheres represent carbon and hydrogen atoms. The Fermi level is marked by the dashed line.

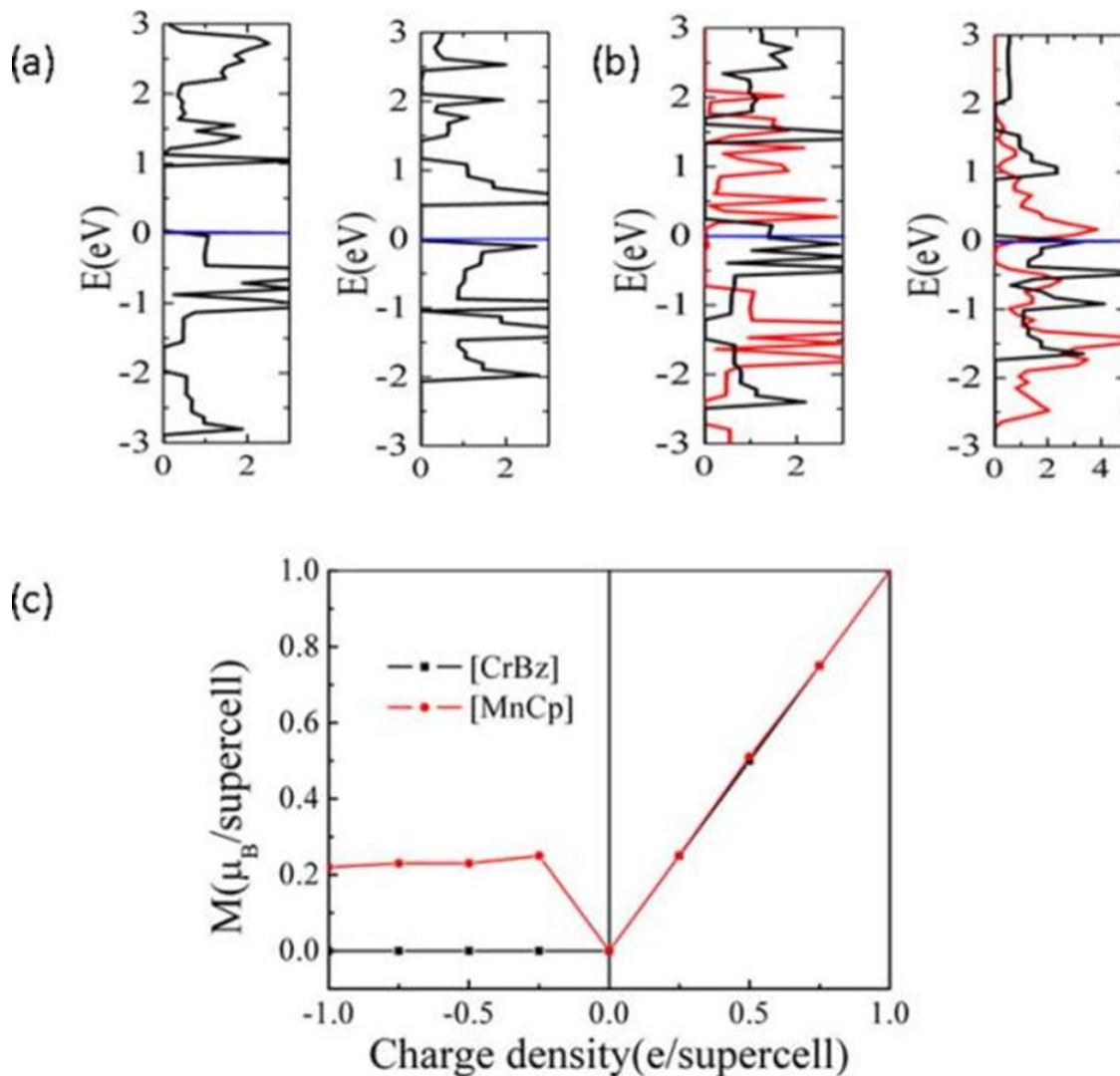


Figure 3 PDOS on Cr in [Cr(Bz)]_∞ SWN (left panel) and on Mn in [Mn(Cp)]_∞ SWN (right panel), in (a) charge-neutral state, and (b) two charge-injection states with the charge injection of $1e$ (red line) and $-1e$ (black line) per supercell, respectively. Blue lines denote the Fermi level. (c) Dependence of induced magnetic moment on the net injected charge per supercell.

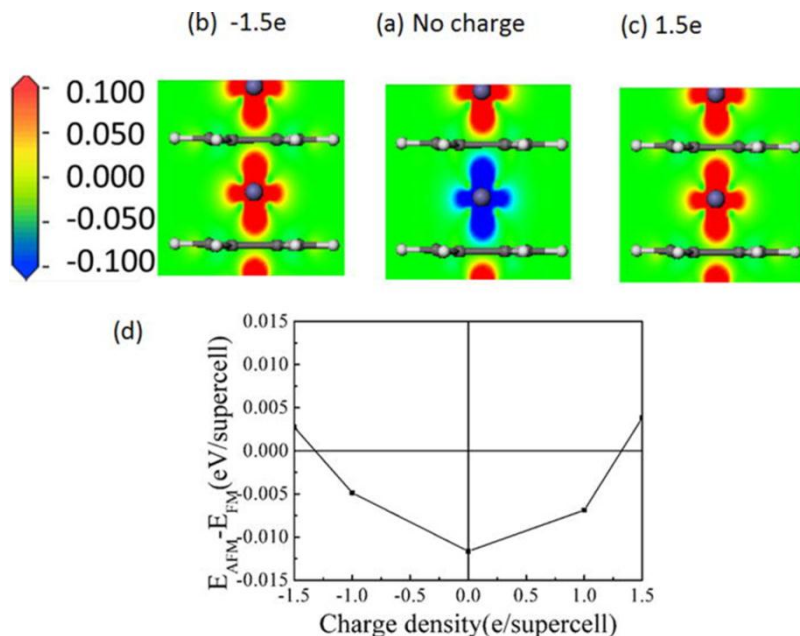


Figure 4 The spin-charge density distribution of [Ti(Bz)]_∞ (a) with no charge injection, and with the charge injection of (b) -1.5e per supercell, and (c) 1.5e per supercell. (d) Dependence of energy difference $E_{AFM} - E_{FM}$ on the injected charge per supercell.

Figure 3(c) displays the induced magnetic moment *versus* the injected charge per supercell. Upon the positive charge injection, the induced magnetic moment is proportional to the net charge per supercell, indicating that the DOS is fully spin-polarized for both SWNs. Upon the electron injection, however, no magnetic moment is induced for [Cr(Bz)]_∞, irrespective of the amount of net charge per supercell, whereas for [Mn(Cp)]_∞ the induced magnetic moment is nearly a constant when the net charge is greater than 0.25e per supercell.

In addition to the $[\text{Cr}(\text{Bz})]_{\infty}$ and $[\text{Mn}(\text{Cp})]_{\infty}$ SWNs, we have investigated electronic and magnetic properties of the $[\text{Ti}(\text{Bz})]_{\infty}$ SWN. As shown in Table 1 and Fig. 4(a), $[\text{Ti}(\text{Bz})]_{\infty}$ SWN possesses unique antiferromagnetic (AFM) properties in the charge-neutral state.⁶ Although under a charge injection of 1 e per supercell does not induce any magnetic transition in the SWN (Table 1), we find that when the $[\text{Ti}(\text{Bz})]_{\infty}$ is subjected to a charge injection of 1.5 e or -1.5 e per supercell, the ground state of the SWN becomes FM (see Fig. 4). The magnetic moment on each Ti atom is slightly decreased from $0.87\mu_{\text{B}}$ to $0.53\mu_{\text{B}}$ (under 1.5 e charge injection) and to $0.82\mu_{\text{B}}$ (under -1.5 e charge injection). In Fig. 4(a) – (c), the spin-density distributions are displayed, wherein the AFM-to-FM transition can be clearly seen. The calculated energy difference between the AFM and FM state, $E_{\text{AFM}}-E_{\text{FM}}$, is shown in Fig. 4(d). With low injected charge per supercell, the AFM state is energetically more favorable, but the FM state becomes more stable when the injected charge is greater than $|1.3e|$ per supercell.

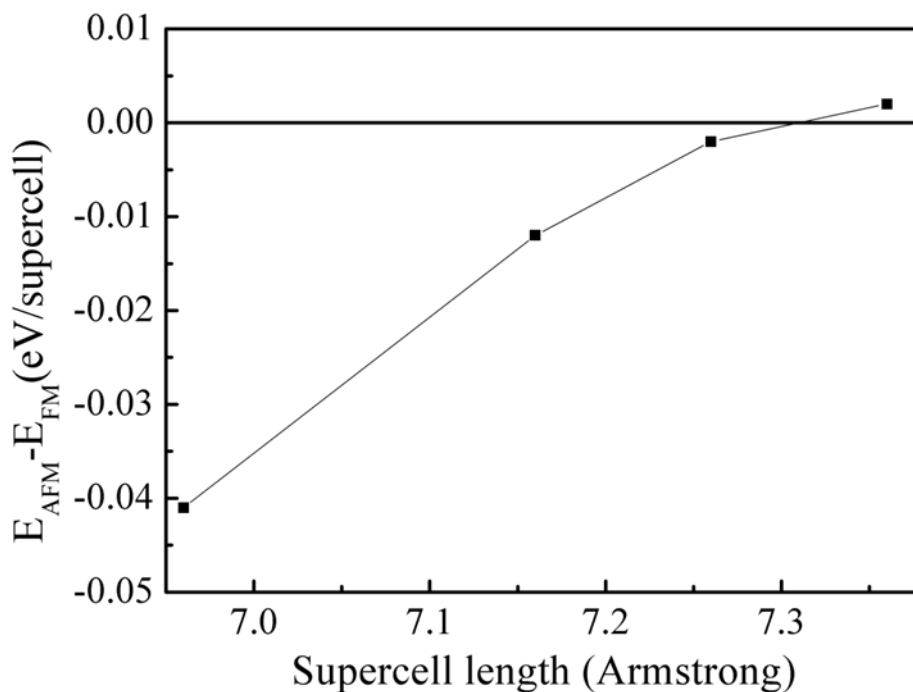


Figure 5. Computed energy difference per supercell $E_{\text{AFM}}-E_{\text{FM}}$ for $[\text{Ti}(\text{Bz})]_{\infty}$ versus the supercell length, which shows that the ground state will change from AFM to FM when the supercell length is prolonged to $\sim 7.30 \text{ \AA}$.

We also find that the AFM-to-FM transition can be induced by mechanically prolonging the length of the SWN along the axis direction. If the $[\text{Ti}(\text{Bz})]_{\infty}$ SWN is elongated by 2.7% in length, the FM state will become more stable than the AFM state (see Fig. 5). Hence, not only the charge injection but also the mechanical elongation can alter the magnetic coupling within the $[\text{Ti}(\text{Bz})]_{\infty}$ SWN. Contrary to the $[\text{Ti}(\text{Bz})]_{\infty}$ SWN, a previous first-principles study has shown that the $[\text{Mn}(\text{Bz})]_{\infty}$ SWN can be switched from FM to AFM if it is elongated by 10% in length, due to the weakening of double exchange interaction by elongation. Here, the change of magnetic state in the $[\text{Ti}(\text{Bz})]_{\infty}$ SWN requires considerably less elongation in length ($< 3\%$), thereby will be easier to realize.

6.4 Conclusions

In summary, using first-principles calculation, we have systematically investigated magnetic and electronic properties of first-row transition-metal-molecular SWNs in positively and negatively charged states. Among all these SWNs, only two, namely, $[\text{Cr}(\text{Bz})]_{\infty}$ and $[\text{Mn}(\text{Cp})]_{\infty}$ SWNs, can be transformed from non-magnetic semiconductors to FM half metals or to FM metals upon charge injection. Moreover, under either charge injection or mechanical elongation, the $[\text{Ti}(\text{Bz})]_{\infty}$ SWN may be switched from AFM to FM. Hence, these quasi-1D SWNs may be exploited as magnetic on/off switches, controlled by their charging state.

6.5 References

1. T. J. Kealy, P. L. Pauson *Nature*, **168**, 1039 (1951).
2. L. Hedberg, K.J. Hedberg, *Chem. Phys.* **53**, 1228 (1970).
3. E. Gard, A. Haaland, D.P. Novak, R.J. Seip, *Organomet. Chem.* **88**, 181 (1975).
4. A. Almenningen, E. Gard, A. Haaland, *J. Organomet. Chem.* **107**, 273 (1976).
5. T. Kurikawa, H. Takeda, M. Hirano; K. Judai, T. Arita, S. Nagao, A. Nakajima, K. Kaya, *Organometallics* **18**, 1430 (1999).
6. N. Hosoya, R. Takegami, J. Suzumura, K. Yada, K. Koyasu, K. Miyajima, M. Mitsul, M.B. Knickelbein, S. Yabushita, A. Nakajima, A. Lanthanide, *J. Phys. Chem. A* **109**, 9 (2005).
7. H.J. Xiang, J.L. Yang, J.G. Hou, Q.S. Zhu, *J. Am. Chem. Soc.* **128**, 2310 (2006).
8. V.V. Maslyuk, A. Bagrets, V. Meded, A. Arnold, F. Evers, M. Brandbyge, T. Bredow, I. Mertig, *Phys. Rev. Lett.* **97**, 097201 (2006).
9. M. Koleini, M. Paulsson, M. Brandbyge, *Phys. Rev. Lett.* **98**, 197202 (2006).
10. N. Atodiresei, P.H. Dederichs, Y. Mokrousov, L. Bergqvist, G. Bihlmayer, S. Blügel, *Phys. Rev. Lett.* **100**, 117207 (2008).
11. L. Zhou, S.W. Yang, M. Ng, M.B. Sullivan, V.B.C. Tan, L. Shen, *J. Am. Chem. Soc.*, **130**, 4023 (2008).
12. L. Shen, S.W. Yang, M.-F. Ng, V. Ligatchev, L. Zhou, Y.J. Feng, *J. Am. Chem. Soc.* **130**, 13956 (2008).
13. K. Hoshino, T. Kurikawa, H. Takeda, A. Nakajima, K. Kaya, *J. Phys. Chem.* **99**, 3053 (1995).

14. K. Miyajima, A. Nakajima, S. Yabushita, M.B. Knickelbein, K. Kaya, *J. Am. Chem. Soc.* **126**, 13202 (2004).
15. K. Miyajima, S. Yabushita, M.B. Knickelbein, A. Nakajima, *J. Am. Chem. Soc.* **129**, 8473 (2007).
16. R. Pandey, B.K. Rao, P. Jena, J.M. Newsam, *Chem. Phys. Lett.* **321**, 142 (2000).
17. R. Pandey, B.K. Rao, P. Jena, M.A. Blanco, *J. Am. Chem. Soc.* **123**, 3799 (2001).
18. A.K. Kandalam, B.K. Rao, P. Jena, R.J. Pandey, *Chem. Phys.* **120**, 10414 (2004).
19. J. Wang, P.H. Acioli, J. Jellinek, *J. Am. Chem. Soc.* **127**, 2812 (2005).
20. J. Wang, J. Jellinek, *J. Phys. Chem. A* **109**, 10180 (2005).
21. W.J. Zheng, J.M. Nilles, O.C. Thomas, K.H. Bowen, *Chem. Phys. Lett.* **401**, 266 (2005).
22. J. Kua, K.M. Tomlin, *J. Phys. Chem. A* **110**, 11988 (2006).
23. M.M. Rahman, H. Kasai, E.S. Dy, *Jpn. J. Appl. Phys.* **44**, 7954 (2005).
24. Z. Zhang, X. Wu, W. Guo, X.C. Zeng, *J. Am. Chem. Soc.* **132**, 10215 (2010).
25. G. Kresse, J. Hafner, *Phys. Rev. B* **47**, 558 (1993).
26. G. Kresse, J. Furthmuller, *Phys. Rev. B* **54**, 11169 (1996).
27. G. Kresse, D. Joubert, *Phys. Rev. B* **59**, 1758 (1999).
28. J.P. Perdew, K. Burke, M. Ernzerhof, *Phys. Rev. Lett.* **77**, 3865 (1996).
29. H.J. Monkhorst, J.D. Pack, *Phys. Rev. B* **13**, 5188 (1976).
30. M. Wu, Z. Zhang, X.C. Zeng, *Appl. Phys. Lett.* **97**, 093109 (2010).
31. E.C. Stoner, *Proc. R. Soc. London, Ser. A* **165**, 372 (1938).